Polymer Characterization Beaucage

J Yang, Y Li, N Hao, A Umair, A Liu, L Li, X Ye *Preparation and Controlled Degradation of Model Amphiphilic Long-Subchain Hyperbranched Copolymers: Hyperblock versus Hypergraft* Macromolecules **52** 1173-1187 (2019). present a careful study of the degradation of amphiphilic (surfactant-like) hyperbranched copolymers (see insets to Figure (a)).
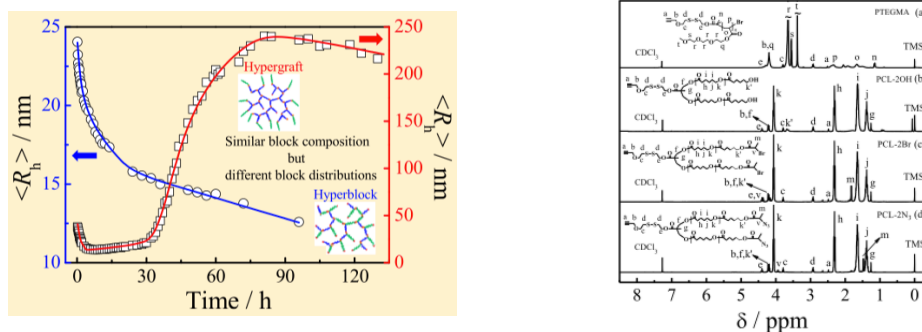

(a)

Figure 3. ^{1}H NMR spectra of (a) PTEGMA$_{13}$, (b) PCL$_{23}$-2OH, (c) PCL$_{23}$-2Br, and (d) macromonomer PCL$_{23}$-2N$_3$.
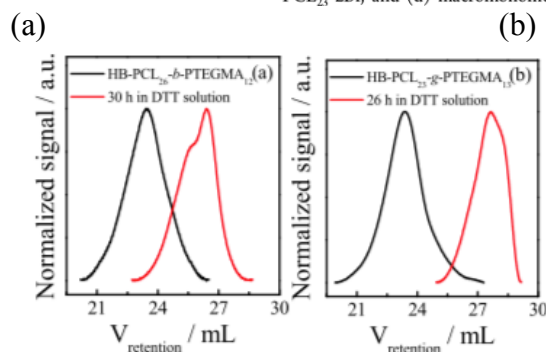
(b)

Figure 6. GPC curves for the two AHPs before and after degradation in THF at [DTT] = 10 mM: (a) fractionated HB-PCL$_{26}$-*b*-PTEGMA$_{12}$ and (b) fractionated HB-PCL$_{23}$-*g*-PTEGMA$_{13}$.

(c)

a) Yang et al. use anionic and RAFT polymerization to produce their hyperbranched self-assembled amphophiles (SAs). Give a brief, "hand waving" description of these two polymerization techniques, including their similarities and differences, as best you can. (*These are the two most important synthesis techniques in current polymer research*.)

b) Yang et al. use proton NMR to characterize their structures. What is δ on the x-axis of graph (b) above, and how do you obtain the units ppm from the measurement?

c) Graph (a) is the TOC graphic from this paper. You are expected to be able to understand this graphic at a glance with no supporting information but it requires a basic understanding of Polymer Science. What is $<R_h>$ and how is it typically determined so that you could get a time dependent structural degradation curve of this type?

d) Yang et al. use the Stokes-Einstein (SE) relationship to obtain $<R_h>$ from the diffusion coefficient. Explain the physical basis of the SE relationship. To what type of structure does the SE relationship refer, and does the structure in (a) seem appropriate for this equation?

e) Figure (c) shows GPC curves before and after degradation. Explain these curves. Particularly, why do the curves move to the right and change after degradation?

Beaucage Polymer Physics Question 1

Jorge Ramirez, T. J. Dursch, and B. D. Olsen (A *Molecular Explanation for Anomalous Diffusion in Supramolecular Polymer Networks* Macromolecules **51** 2517-2525 (2018).) discuss computer simulations of four-arm star polymers with "sticky feet" that form supramolecular networks in solution. These polymers can form a dynamic hierarchy characterized by hindered Fickian diffusion at short distances followed at intermediate size by "super-diffusive", "caging" behavior and finally a secondary Fickian regime at large distances as shown in Figure 3 below, involving hopping and walking. *d* is the distance over which motion is being observed and τ is the characteristic time associated with a particular size scale.
(see also https://www.youtube.com/watch?time_continue=171&v=dzRhTxhZWPo)
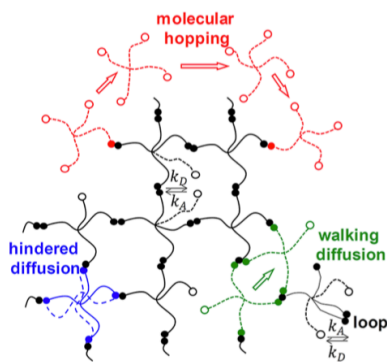

Figure 1. Schematic view of the association reactions (filled/open symbols represent associated/free stickers), the formation of loops, and the three main diffusion mechanisms in associating star-shaped polymers.
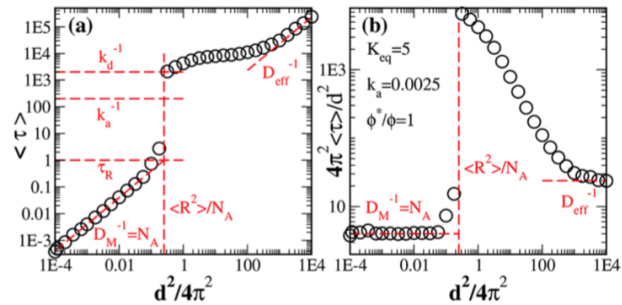

Figure 3. (a) Characteristic time $\langle\tau\rangle$ as a function of the domain length from BD simulations of FRS experiments of molecules with 4 arms, $k_A = 0.0025$ and $K_{eq} = 5$, at the overlap concentration. (b) Normalized $\langle\tau\rangle$ as a function of the domain length, revealing differences in the early- and large-distance diffusion coefficients as well as the apparent superdiffusive scaling.

a) What is the relationship between $\langle\tau\rangle$ and *d* in the Fickian "*hindered diffusion*" regime? How can the diffusion coefficient be determined from the simulations? (Remember that a particle subject to thermal motion follows a random walk by Brownian motion.)

b) For *d* less that a radius of gyration of the polymer, the chains are in the Fickian regime. Super-diffusive motion involves "*walking diffusion*" shown in Figure 1. From Figure 3, what would you say is the value for the radius of gyration using units of the x-axis in Figure 3?

c) Is the diffusion coefficient for the "*molecular hopping*" regime larger or smaller than that for the hindered diffusion regime? Does it have a larger or smaller characteristic time? Explain this apparent discrepancy. You may want to rewrite the equation for Fickian diffusion from part "a".

d) Ramirez indicates that in his simulations the chains are in "*semi-dilute condition below the entanglement concentration*". The chains are considered "*Rouse chains of correlation blobs*". The blob size and terminal relaxation time are given by,

$$\langle R^2 \rangle = R_g^2 \left(\frac{\phi^*}{\phi}\right)^{(2\nu-1)/(3\nu-1)} \qquad \tau_R = \tau_F \left(\frac{\phi^*}{\phi}\right)^{(3\nu-1)/(3\nu-1)}$$

, where ν is $1/d_f$ and R_g and τ_R are for the arms. For good solvent scaling explain the origin of the blob, size equation.

e) Ramirez states that the stickers at the end of the polymer arms in a given time step can 1) remain unreacted; 2) form a loop (intramolecular); 3) for a bridge (intermolecular); or 4 detach from a loop or a bridge. *Sticker association is considered in a mean-field sense: the probability of association takes into account the state of all stickers in the system.*" Explain what Ramirez means by a mean field. How does this differ from considering specific interactions?

Beaucage Polymer Physics Question 2

Julia Higgins recently published an article on polymer blends using PαMS-AN and d-PMMA ((a) below) with the intent of producing controlled, quenched, spinodal structures for various applications such as separation membranes (Y Aoki, H Wang, W Sharratt, RM Dalgliesh, JS Higgins, JT Cabral, *Small Angle Neutron Scattering Study of the Thermodynamics of Highly Interacting PαMSAN/dPMMA Blends* Macromolecules **52** 1112-1124 (2019).). Neutron scattering can be used to quantify χ_{12} in the miscible regime since from the RPA equation,

$$\frac{1}{S(q)} = \frac{1}{S_1(q)} + \frac{1}{S_2(q)} - 2\frac{\tilde{\chi}_{12}}{v_0}, \text{ where } \tilde{\chi}_{12} = -\frac{1}{2}\frac{\partial^2[\phi(1-\phi)\chi_{12}]}{\partial\phi^2}.$$
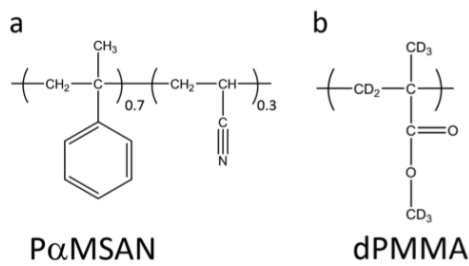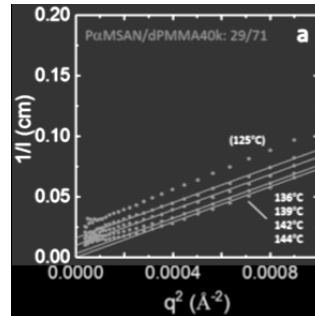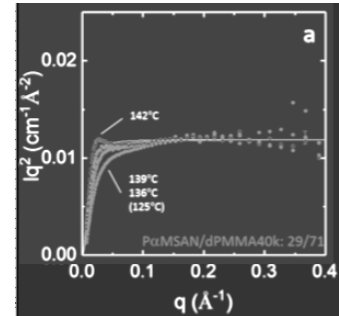

Figure 1. Monomer repeat units of poly(α-methylstyrene-co-acrylonitrile) and (deuterated) poly(methyl methacrylate).

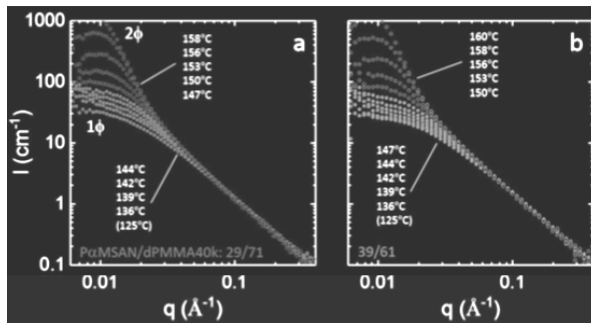(a)   (b)   (c)

(d)   (e)

a) Show that $\tilde{\chi}_{12} = \chi_{12}$ when there is no concentration dependence to χ_{12}.

b) Plot (b) above follows the Ornstein-Zernike function, $S(q) = \frac{S(0)}{1+\xi^2 q^2}$, where ξ is the correlation length. Physically what is ξ and how is ξ determined from plot (b)? Note: Guinier's law can be written $1/S(q) = (1/S(0)) \exp(q^2 R_g^2/3) = (1/S(0)) (1 + q^2 R_g^2/3 + …)$ at low q. Compare this with the OZ approach. Is Guinier's law appropriate here?

c) Figure (c) is called a Kratky Plot. For a polymer chain in the melt why would the Kratky plot be appropriate? Higgins discusses the appearance of a peak in this plot. Does the peak have any meaning?

d) & e) Explain the two regimes of behavior seen in Figures (d) and (e). (*The lighter curves are a different regime than the darker curves.*) How would the second, higher intensity, regime appear in plots (b) and (c) above?

Preparation and Controlled Degradation of Model Amphiphilic Long-Subchain Hyperbranched Copolymers: Hyperblock versus Hypergraft

Jinxian Yang,[†,§] Yixia Li,[†] Nairong Hao,[†] Ahmad Umair,[†] Anhong Liu,[†] Lianwei Li,*[†] and Xiaodong Ye*[†,‡]

[†]Hefei National Laboratory for Physical Sciences at the Microscale, Department of Chemical Physics, and [‡]CAS Key Laboratory of Soft Matter Chemistry, University of Science and Technology of China, Hefei, Anhui 230026, China

[§]Shenzhen Key Laboratory for Functional Polymer, School of Chemistry and Chemical Engineering, Shenzhen University, Shenzhen, Guangdong 518060, China

S Supporting Information

ABSTRACT: The controlled degradation of amphiphilic hyperbranched polymers (AHPs) is the first consideration for their bio-related applications. In this contribution, we aim to get some insight into the effect of block distribution and composition on the degradation behavior of AHPs model systems. Degradable amphiphilic hyperbranched block (Hyperblock) and graft (Hypergraft) copolymers with hydrophobic poly(ε-caprolactone) (PCL) and hydrophilic poly[tri(ethylene glycol) methyl ether acrylate] (PTEGMA) as building blocks were prepared in this study, i.e., HB-PCL-*b*-PTEGMA and HB-PCL-*g*-PTEGMA. The two kinds of AHPs own cleavable disulfide linkages embedded at all branching sites. Their degradation behavior was comparatively investigated in aqueous solutions. The results reveal that the block distribution and composition play different roles in the regulation of degradation behavior of long-subchain hyperbranched self-assembly amphiphiles (SAs). Namely, the degradation process is mainly affected by chain architecture of resultant SAs, while for a given architecture, the degradation rate can be regulated by systematically varying the block composition.
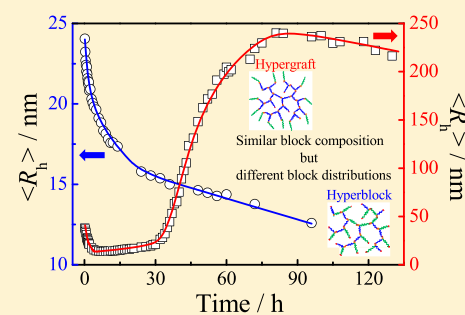
◼ INTRODUCTION

As one main subclass of dendritic polymers, hyperbranched polymers (HPs) have received increasing attention in the past two decades because of their unique properties, such as facile synthesis,[1−4] good solubility,[5] low viscosity,[6] and high number of terminal functional groups.[3,7] These advantages have led to wide use of HPs as functional materials in various applications, such as biomedical materials,[4,8−15] polymer coating materials,[16] optoelectronic materials,[17,18] and so forth. Accordingly, numerous efforts have been devoted to the understanding of the structure−property relationship for HPs in different applications.

Among the various applications mentioned above, the development of amphiphilic hyperbranched polymer (AHP)-based encapsulating/framework materials for nanomedicine application is one of the hottest topics and has been extensively studied in the past decade. Namely, Yan et al.[19] studied the self-assembly and redox-responsive property of polyphosphate-based AHPs. Kim et al.[20] designed a double hydrophilic hyperbranched copolymer made of poly(ethylene oxide) and polyglycerol and found that the assembled micelles can exhibit a pH-responsive release of doxorubicin (DOX). Liu et al.[21] prepared hyperbranched unimolecular poly-prodrug micelles for synergistic reductive milieu-triggered drug release and enhanced magnetic resonance signals. Clearly, all these examples demonstrate the great potential of using HPs as eco-friendly functional materials in bio-related applications. Nevertheless, a careful literature search shows that only a limited understanding of the structure−property relation for AHPs has been achieved. It is yet to be found that how the molecular parameters of AHPs, such as the molar mass, molar mass distribution, degree of branching, and the hydrophilicity/hydrophobicity balance, affect the framework degradation, small-molecule loading efficiency, and release behavior of AHP-based self-assembly amphiphiles (SAs) in aqueous solutions.[22,23] This is mainly attributed to the uncontrollability of structural parameters of prepared HPs in previous reports.[20,24]

So far, two major synthetic approaches have been developed for the preparation of HPs including the chain-growth polymerization and step-growth polymerization strategies. Because of the synthetic facilitation, the chain-growth polymerization methods, including self-condensing vinyl polymerization (SCVP)[25−27] and self-condensing ring-opening polymerization (SCROP),[28,29] have been widely used for the preparation of HPs. Even the synthetic methods could offer

Scheme 1. Schematic Illustration of Topological Structures of Prepared (a) Hyperblock and (b) Hypergraft Amphiphilic Copolymers
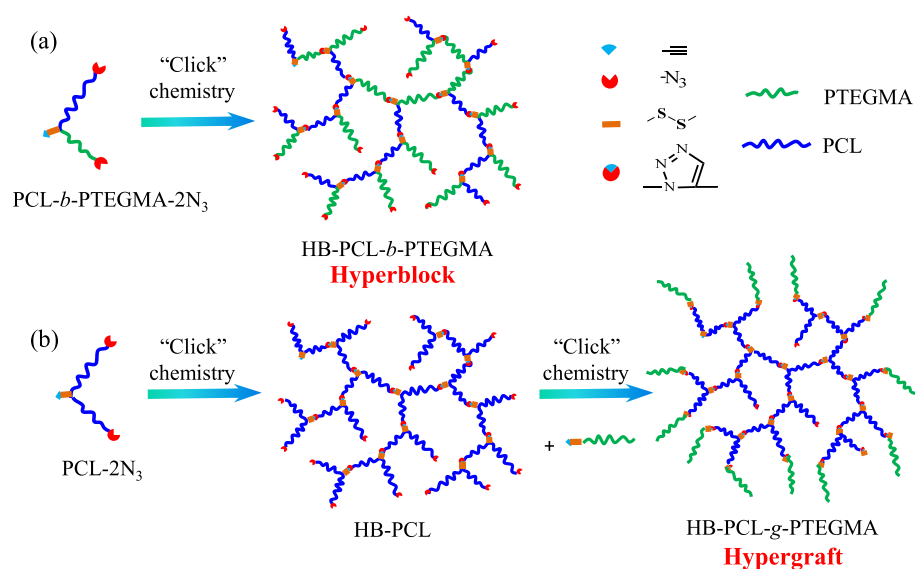
moderate control over the chain parameters such as the molar mass and the average branching subchain length, while the subchain length distribution is still less controlled, which partially explains why the previously established structure−property relationships generally lack the universality and could hardly be applied to different systems. In contrast, the step-growth polymerization approach has shown a much better control over these chain parameters.[30] Recently, we proposed a novel seesaw-type AB$_2$ macromonomer strategy for the preparation of HPs with uniform and controlled subchains,[31,32] where the subchain length is exactly half of initial macromonomer length. Our systematic investigations have revealed that various solution properties of resultant HPs are strongly dependent on the internal subchain length.[33−35] Moreover, using model hyperbranched polystyrene chains with both uniform subchains and controlled locations of cleavable disulfide linkage,[36] we quantitatively investigated their degradation behavior in THF, and the results highlighted the importance of controlled locations of cleavable disulfide linkages for model degradation.

For a real AHP nanocarrier system, loading efficiency, degradation rate of polymer framework, drug release rate, and biocompatibility are the critical factors to be considered while designing the structure of AHP nanocarriers. On the other hand, all the properties are mainly correlated to the molecular parameters, such as the overall molar mass, polydispersity, number and distribution of branching subchains and degradation sites, and block sequence. It is no exaggeration to say that the preparation of model AHP systems with controlled branching subchains and degradation sites, as well as well-defined distribution pattern and composition of hydrophobic/hydrophilic blocks, is the prerequisite for further regulating the related property of AHPs-based nanocarrier system.

For the proof of concept, we prepared two hyperbranched polymer model systems (Hyperblock and Hypergraft) for the comparative study of the influence of block distribution and composition on the degradation behavior of AHP SAs in aqueous solutions, where the biocompatible poly(ε-caprolactone) (PCL) and poly[tri(ethylene glycol) methyl ether

acrylate] (PTEGMA) were used as hydrophobic and hydrophilic blocks, respectively (Scheme 1). For Hyperblock, it was made from PCL-b-PTEGMA diblock macromonomer, and the inserted hydrophobic and hydrophilic blocks were randomly distributed in the resultant Hyperblock structure, while Hypergraft was made of a hydrophobic hyperbranched PCL core with hydrophilic PTEGMA chains grafted on the periphery. Based on our previously proposed synthetic approach, both model systems own controlled branching subchains and cleavable redox-sensitive disulfide bonds. Moreover, we first intentionally controlled the composition of hydrophobic/hydrophilic blocks of Hyperblock and Hypergraft copolymers to be similar to each other to study the effect of block distribution. In addition, for a given architecture, hyperbranched copolymers with varied block length were also prepared to study the effect of block composition. Thus, the two model systems afford us the opportunity, *for the first time*, to elucidate how the block distribution and composition influence the degradation of amphiphilic long-subchain HPs in aqueous solutions. Experimentally, a significantly different degradation behavior was observed for the two AHPs systems, highlighting the importance of the rational design of block distribution and composition for AHPs in different applications. The results simultaneously demonstrate that both of the model systems are potential candidates as nanocarriers for practical nanomedicine application.

■ MATERIALS

ε-Caprolactone (CL, Aladdin, 99%) was dried over calcium hydride and distilled under reduced pressure. Copper(I) bromide (CuBr, Alfa Aesar, 98%) was washed with glacial acetic acid to remove soluble oxidized species, filtrated, washed with ethanol, and dried under vacuum. Acetonitrile (ACN, Sinopharm, 99%) and triethylamine (TEA, Sinopharm, 97%) were refluxed over p-toluenesulfonyl chloride and then distilled over calcium hydride prior to use. Dichloromethane (DCM, Sinopharm, 97%) was distilled over calcium hydride. Dimethylformamide (DMF, Sinopharm, 97%) was first dried with anhydrous magnesium sulfate and then distilled under reduced pressure. Tetrahydrofuran (THF, Sinopharm, 99%) and toluene (Sinopharm, 97%) were refluxed over sodium for 24 h and then distilled. 2-Bromopropionyl bromide (Aladdin, 97%), 2-bromoisobu-

Scheme 2. Schematic Illustration of (a) Hyperblock Copolymer HB-PCL-*b*-PTEGMA and (b) Hypergraft Copolymer HB-PCL-*g*-PTEGMA
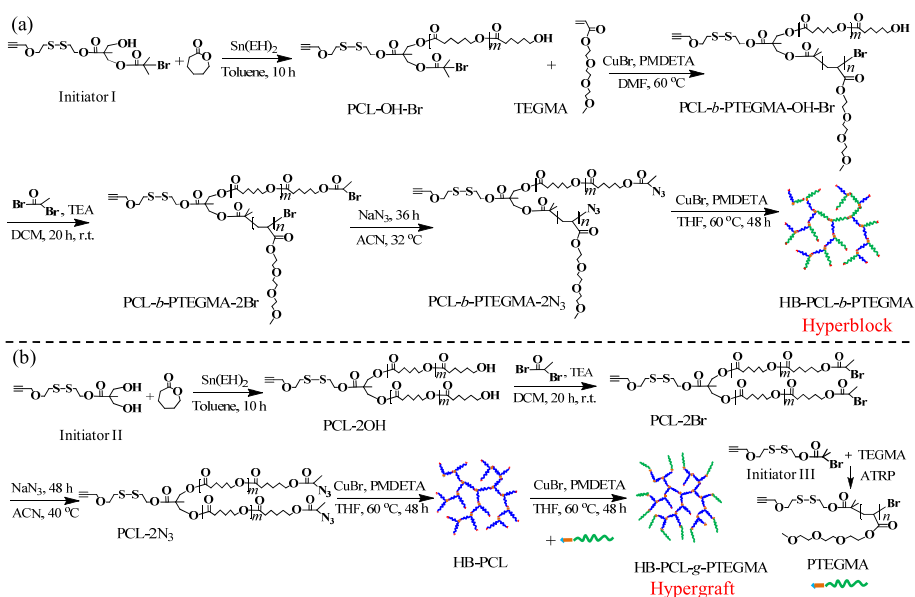
tyryl bromide (Aladdin, 98%), acryloyl chloride (Aladdin, 96%), triethylene glycol monomethyl ether (Sigma-Aldrich, 95%), sodium azide (NaN$_3$, Sigma-Aldrich, 99%), *N,N,N′,N′,N″*-pentamethyl-diethylenetriamine (PMDETA, Sigma-Aldrich, 99%), tin(II) 2-ethylhexanoate (Sn(EH)$_2$, Sigma-Aldrich, 95%), and other analytical grade reagents from Sinopharm were used as received. The water used in this work is Milli-Q water (Millipore, resistivity = 18.2 MΩ·cm at 25 °C).

The synthesis of Hyperblock (HB-PCL$_{26}$-*b*-PTEGMA$_{12}$) and Hypergraft copolymer (HB-PCL$_{23}$-*g*-PTEGMA$_{13}$) is detailed as follows, as shown in Scheme 2, and the syntheses of other hyperbranched copolymers with different compositions are similar. The subscript number represents the degree of polymerization of the repeating unit calculated from ^{1}H NMR, which will be discussed later.

Synthesis of PCL-OH-Br by Ring-Opening Polymerization (ROP). In a typical reaction, 0.67 g of initiator I (1.46 mmol), 4.01 g of *ε*-caprolactone (35.2 mmol), and 0.09 g of Sn(EH)$_2$ (0.22 mmol) were added into a 100 mL three-neck bottle, and then anhydrous toluene (50 mL) was added. The mixture was stirred for 10 h at 115 °C under an argon atmosphere. The solvent was removed by rotary evaporation after the reaction was stopped. The product was redissolved in THF and precipitated into an excess of cold methanol/water mixture (3/1, v/v). The precipitation process was repeated for three times. The white solid PCL$_{26}$-OH-Br was obtained after drying under vacuum at 40 °C for 24 h (yield: 4.0 g, 85%). ^{1}H NMR chemical shift for PCL$_{26}$-OH-Br (δ, ppm, CDCl$_3$): 4.38−4.45 (−COO−CH_2−CH_2−SS−), 4.20−4.37 (−COO−CH_2−C−COO−), 4.18−4.20 (CH≡C−CH_2−), 4.00−4.12 (−OOC−CH$_2$−CH$_2$−CH$_2$−CH$_2$−CH_2−O−), 3.75−3.83 (−CH_2−O−CH_2−CH$_2$−SS−), 3.60−3.70 (−CH_2−CH$_2$−OH), 2.85−3.00 (−CH$_2$−CH_2−SS−CH_2−CH$_2$−), 2.43−2.52 (CH≡C−), 2.24−2.42 (−OOC−CH_2−CH$_2$−CH$_2$−CH$_2$−CH$_2$−O−), 1.65−1.87 (−OOC−C(CH_3)$_2$−Br), 1.53−1.77 (−OOC−CH$_2$−CH_2−CH$_2$−CH_2−CH$_2$−O−), 1.27−1.48 (−OOC−CH$_2$−CH$_2$−CH_2−CH$_2$−CH$_2$−O−), 1.26−1.32 (−OOC−C−CH_3).

Synthesis of PCL-*b*-PTEGMA-OH-Br by Atom Transfer Radical Polymerization (ATRP). Tri(ethylene glycol) methyl ether acrylate (TEGMA) was synthesized according to the reported procedure.[37] 1.6 g of PCL$_{26}$-OH-Br (0.47 mmol), 5.10 g of TEGMA (23.4 mmol), 100 μL of PMDETA (0.48 mmol), and anhydrous DMF (5 mL) were added into a 20 mL glass tube with a magnetic stirrer. After degassing by three freeze−vacuum−thaw cycles, 68 mg of CuBr (0.47 mmol) was added into the tube, and then the tube was

sealed under vacuum. The mixture was stirred at 60 °C for 3 h. Then the mixture was diluted with THF and passed through a short neutral alumina column to remove the metal salt. The solvent was removed by rotary evaporation. The product was redissolved in THF and precipitated into an excess amount of cold *n*-hexane. The precipitation process was repeated for three times. The white solid PCL$_{26}$-*b*-PTEGMA$_{12}$-OH-Br was obtained after drying under vacuum at 40 °C for 24 h (yield: 2.2 g, 74%).

Synthesis of PCL-*b*-PTEGMA-2Br by Functional Modification. 2.05 g of PCL$_{26}$-*b*-PTEGMA$_{12}$-OH-Br (0.34 mmol), 0.34 g of TEA (3.4 mmol), and anhydrous DCM (30 mL) were added into a 50 mL three-neck bottle. 0.73 g of 2-bromopropionyl bromide (3.4 mmol) dissolved in anhydrous DCM (5 mL) was added dropwise within 1 h at 0 °C. The mixture was stirred for 20 h at room temperature under an argon atmosphere. The solvent was removed by rotary evaporation after the reaction was stopped. The residue was redissolved in THF. After the removal of insoluble salts by filtration, the filtrate was concentrated by a rotary evaporator. The polymer solution was precipitated into an excess amount of cold *n*-hexane. The precipitation process was repeated three times. The light yellow solid PCL$_{26}$-*b*-PTEGMA$_{12}$-2Br was obtained after drying under vacuum at 40 °C for 24 h (yield: 1.89 g, 92%).

Synthesis of PCL-*b*-PTEGMA-2N$_3$ by Azidation. 1.84 g of PCL$_{26}$-*b*-PTEGMA$_{12}$-2Br (0.30 mmol) was dissolved in ACN (20 mL), and then 0.59 g of NaN$_3$ (9.1 mmol) was added into the solution. The mixture was stirred at 32 °C for 36 h under an argon atmosphere. The solvent was removed by rotary evaporation after the reaction was stopped, and the product was redissolved in THF. After being centrifuged for 30 min × 3, the supernatant was precipitated into an excess amount of cold *n*-hexane. The light yellow solid PCL$_{26}$-*b*-PTEGMA$_{12}$-2N$_3$ was obtained after drying under vacuum at 40 °C for 24 h (yield: 1.6 g, 87%).

Synthesis of Hyperblock Copolymer HB-PCL-*b*-PTEGMA by "Click" Reaction. 1.55 g of PCL$_{26}$-*b*-PTEGMA$_{12}$-2N$_3$ (0.26 mmol), 96 μL of PMDETA (0.46 mmol), and THF (10 mL) were added into a 20 mL glass tube with a magnetic stirrer. After degassing by three freeze−vacuum−thaw cycles, 68 mg of CuBr (0.46 mmol) was added into the tube, and then the tube was sealed under vacuum. The mixture was stirred at 60 °C for 48 h. Then the mixture was diluted with THF and passed through a short neutral alumina column to remove the metal salt. After being concentrated, the polymer solution was precipitated into an excess amount of cold *n*-hexane. The solid HB-PCL$_{26}$-*b*-PTEGMA$_{12}$ was obtained after drying under vacuum at

40 °C for 24 h (yield: 1.1 g, 71%), and then the product was fractionated with n-hexane/THF mixture (1−1.5/1, v/v) (yield: 0.12 g, 11%).

Synthesis of PCL-2OH by ROP. In a typical reaction, 0.74 g of initiator II (2.4 mmol), 6.02 g of ε-caprolactone (52.8 mmol), and 0.20 g of Sn(EH)$_2$ (0.49 mmol) were added into a 100 mL three-neck bottle, and then anhydrous toluene (60 mL) was added. The mixture was stirred for 10 h at 115 °C under an argon atmosphere. The solvent was removed by rotary evaporation after the reaction was stopped. The product was redissolved in THF and precipitated into an excess of cold methanol/water mixture (3/1, v/v). The precipitation process was repeated for three times. The white solid PCL$_{23}$-2OH was obtained after drying under vacuum at 40 °C for 24 h (yield: 6.1 g, 90%).

Synthesis of PCL-2Br by Functional Modification. 5.8 g of PCL$_{23}$-2OH (2.0 mmol), 2.51 g of TEA (24.9 mmol), and 60 mL of anhydrous DCM were added into a 100 mL three-neck bottle. A solution of 5.34 g of 2-bromopropionyl bromide (24.7 mmol) in anhydrous DCM (10 mL) was added dropwise within 1 h at 0 °C. The mixture was stirred for 20 h at room temperature under an argon atmosphere. The solvent was removed by rotary evaporation after the reaction was stopped. The residue was redissolved in THF. After the removal of insoluble salts by filtration, the filtrate was concentrated by a rotary evaporator. The polymer solution was precipitated into an excess amount of cold n-hexane. The precipitation process was repeated for three times. The light yellow solid PCL$_{23}$-2Br was obtained after drying under vacuum at 40 °C for 24 h (yield: 4.5 g, 78%).

Synthesis of PCL-2N$_3$ by Azidation. 2.3 g of PCL$_{23}$-2Br (0.78 mmol) was dissolved in ACN (20 mL), and then 1.4 g of NaN$_3$ (21.5 mmol) was added into the solution. The mixture was stirred at 40 °C for 48 h under an argon atmosphere. The solvent was removed by rotary evaporation after the reaction was stopped, and the product was redissolved in THF. After being centrifuged for 30 min × 3, the supernatant was precipitated into an excess of cold methanol/water mixture (3/1, v/v). The light yellow solid PCL$_{23}$-2N$_3$ was obtained after drying under vacuum at 40 °C for 24 h (yield: 1.3 g, 57%).

Synthesis of PTEGMA by ATRP. 0.78 g of initiator III (2.3 mmol), 7.02 g of TEGMA (32.2 mmol), 480 μL of PMDETA (2.30 mmol), and anhydrous DMF (5 mL) were added into a 20 mL glass tube with a magnetic stirrer. After degassing by three freeze−vacuum−thaw cycles, 230 mg of CuBr (1.6 mmol) was added into the tube, and then the tube was sealed under vacuum. The mixture was stirred at 60 °C for 3 h. Then the mixture was diluted with THF and passed through a short neutral alumina column to remove the metal salt. The solvent was removed by rotary evaporation. The product was redissolved in THF and precipitated into an excess amount of cold n-hexane. The precipitation process was repeated for three times. The transparent liquid PTEGMA$_{13}$ was obtained after drying under vacuum at 40 °C for 24 h (yield: 3.1 g, 47%). ^{1}H NMR chemical shift for PTEGMA$_{13}$ (δ, ppm, CDCl$_3$): 4.25−4.45 (CH≡C−CH$_2$−, −COO−CH$_2$−CH$_2$−SS−, −COO−CH$_2$−CH$_2$−O−), 3.75−3.84 (−O−CH$_2$−CH$_2$−SS−), 3.60−3.74 (−COO−CH$_2$−CH$_2$−O−CH$_2$−CH$_2$−O−CH$_2$−CH$_2$−O−), 3.50−3.60 (−O−CH$_2$−CH$_2$−O−CH$_3$), 3.29−3.43 (−O−CH$_3$), 2.85−3.00 (−CH$_2$−CH$_2$−SS−CH$_2$−CH$_2$−), 2.47−2.56 (CH≡C−), 2.20−2.47 (−CH$_2$−CH−COO−), 1.38−2.15 (−CH$_2$−CH−COO−), 1.05−1.21 (−C(CH$_3$)$_2$−COO−).

Synthesis of Hypergraft Copolymer HB-PCL-g-PTEGMA. 1.2 g of PCL$_{23}$-2N$_3$ (0.41 mmol), 180 μL of PMDETA (0.86 mmol), and THF (6 mL) were added into a 20 mL Schlenk bottle. After degassing by three freeze−vacuum−thaw cycles, 120 mg of CuBr (0.83 mmol) was added immediately. 1.2 mL of hyperbranched PCL (HB-PCL$_{23}$) solution was taken out after the mixture was stirred at 60 °C for 48 h. Then a degassed polymer solution containing 3.0 g of PTEGMA$_{13}$ (9.4 mmol) was added into the Schlenk bottle, and the reaction was continued at 60 °C for another 48 h to get HB-PCL$_{23}$-g-PTEGMA$_{13}$. The remaining HB-PCL$_{23}$ and HB-PCL$_{23}$-g-PTEGMA$_{13}$ polymer solutions were treated with a similar procedure; i.e., the solutions were first diluted with THF and passed through a short neutral alumina column to remove the metal salt. After being concentrated, the HB-

PCL solution was precipitated into an excess of cold methanol/water mixture (3/1, v/v) while the HB-PCL$_{23}$-g-PTEGMA$_{13}$ solution was precipitated into an excess amount of cold n-hexane. The HB-PCL$_{23}$-g-PTEGMA$_{13}$ was further fractionated with n-hexane/THF mixture (1−1.5/1, v/v). The light green solid HB-PCL$_{23}$ (yield: 50 mg, 25%) and HB-PCL$_{23}$-g-PTEGMA$_{13}$ (yield: 0.2 g, 8.3%) were obtained after drying under vacuum at 40 °C for 24 h.

Preparation of Bare Polymeric Self-Assembly Amphiphiles (SAs). All the SAs were prepared with the same procedure, and all the copolymers used are fractionated samples. In a typical process, 5 mg of HB-PCL$_{26}$-b-PTEGMA$_{12}$ was dissolved in DMF (1 mL). The water (5 mL) was added immediately into this polymer solution under vigorous stirring. The solution was dialyzed against water for 24 h (molecular weight cutoff ~14000 g/mol) after being stirred at room temperature for 1 h.

Preparation of Doxorubicin (DOX) Loaded SAs. The typical preparation procedure of DOX loaded SAs was described as follows. First, DOX solution with a concentration of 10 mg/mL was prepared by mixing 10 mg of DOX·HCl and 5 mol equiv of TEA in DMSO (1 mL). 5 mg of HB-PCL$_{26}$-b-PTEGMA$_{12}$ was dissolved in DMF, and 100 μL of DOX solution (10 mg/mL) was added. Then water (1 mL) was added immediately into the mixture under vigorous stirring. The solution was dialyzed against water for 24 h (molecular weight cutoff ~14000 g/mol) after being stirred at room temperature for 1 h. The DOX loaded SAs solution was centrifuged for 10 min × 3 at 4000 rpm to remove unloaded DOX. The UV absorbance of the mixture (100 μL DOX loaded SAs solution mixed with 900 μL DMSO) at 485 nm was measured to determine the total loading of DOX.[38,39] A standard curve of DOX in DMSO was obtained by the UV−vis spectrophotometer at 485 nm (Figure S1). The drug loading content (DLC) and drug loading efficiency (DLE) were calculated according to the following formulas:[40]

$$\text{DLC (\%)} = \frac{m_{\text{DOX in micelles}}}{m_{\text{polymer}} + m_{\text{DOX in micelles}}} \times 100\% \tag{1}$$

$$\text{DLE (\%)} = \frac{m_{\text{DOX in micelles}}}{m_{\text{DOX}}} \times 100\% \tag{2}$$

Degradation of Hyperblock and Hypergraft Copolymers in THF. 25 mg of Hyperblock or Hypergraft copolymer was dissolved into 50 mL of THF. The oxygen in the solution was removed by bubbling nitrogen for 1 h, and then ~80 mg of DTT was added into the solution. The degradation processes were monitored at 25 °C by GPC.

Drug Release Kinetics in Vitro. The drug release was conducted at 37 °C in 20 mM PB buffer (pH 7.4, 10 mM DTT). Typically, drug loaded SAs solutions were added into a dialysis bag (molecular weight cutoff ~14000 g/mol) and dialyzed against 20 mL of PB buffer. At predetermined time points, the old buffer solution containing DOX was taken out, and 20 mL of fresh buffer was added. The buffer solution was freeze-dried and dissolved in DMSO. The DOX content was measured by a UV−vis spectrophotometer at 485 nm. The cumulative release of DOX was calculated.

Characterization. ^{1}H NMR measurements were conducted on a Bruker AV400NMR spectrometer. Deuterated chloroform (CDCl$_3$) was used as the solvent while tetramethylsilane (TMS) was used as an internal standard. The concentration of polymers was ~20 g/L. FTIR spectra were performed on a Bruker VECTOR-22 IR spectrometer. The samples were prepared by the KBr disk method, and the spectra were collected at 64 scans with a spectral resolution of 4 cm^{-1}. The molar mass and polydispersity index (PDI = M_w/M_n) were determined by gel permeation chromatography (GPC, Waters 1515) equipped with three Waters Styragel columns (HR2, HR4, and HR6) and a refractive index detector (RI, Wyatt WREX-02). The column oven temperature was kept at 35 °C. THF was used as eluent, and the flow rate was set at 1.0 mL/min. Molar masses were calibrated with narrowly distributed linear polystyrene samples.

Differential Scanning Calorimetry (DSC). DSC was performed on a Q2000 differential scanning calorimeter from TA Instruments under a nitrogen flow rate of 100 mL/min. First, the sample was

heated from −90 to 150 °C to remove the thermal history, and then the sample was reheated after cooling from 150 to −90 °C. The scanning rate was set at 10 °C/min. The endothermic maximum temperature during reheating was taken as the melting temperature (T_m). The degree of crystallinity (χ_c) was calculated according to the equation as follows:[41,42]

$$\chi_c = \Delta H_m/(W_{PCL} \times \Delta H_{m,0}) \tag{3}$$

where ΔH_m is the heat of fusion per gram of copolymers determined based on the endothermic peak. 136.4 J/g ($\Delta H_{m,0}$) was used as a reference for the melting enthalpy of 100% crystalline PCL.[42] W_{PCL} is the weight fraction of PCL in the copolymer which was calculated by ^{1}H NMR integral areas.

Thermal Gravimetric Analysis (TGA). TGA was performed on a Discovery TGA from TA Instruments under a nitrogen flow rate of 100 mL/min. The sample was heated to 800 °C, and the heating rate was set at 10 °C/min.

Dynamic Light Scattering (DLS). A commercial LLS spectrometer (ALV/DLS/SLS-5022F) equipped with a multi-τ digital time correlator (ALV5000) was used. The Laplace inversion of each measured intensity−intensity time correlation function $G^{(2)}(q,t)$ in the self-beating mode using both the cumulants and CONTIN analysis can result in a line-width distribution $G(\Gamma)$. Then $G(\Gamma)$ can be converted to translational diffusion coefficient distribution $G(D)$ according to the equation $\Gamma = Dq^2$. The hydrodynamic radius distribution $f(R_h)$ can be obtained via the Stokes−Einstein equation, $R_h = k_B T/6\pi\eta_0 D$, where k_B, T, and η_0 are the Boltzmann constant, the absolute temperature, and the viscosity of solvent, respectively. The scattering angle was fixed at 30°, and the temperature was controlled at 25 °C. The concentration for all the samples was fixed at 0.6 mg/mL. In a typical degradation process, the oxygen in SAs solution (2 mL) was removed by bubbling nitrogen for 10 min, and then 3.2 mg of DTT was added into the solution. All the solutions were filtered through hydrophilic filters (Millipore, aperture 0.45 μm) before DLS measurements.

Cell Viability Assay. HeLa cells were seeded in 96-well plates (4 × 10^3 cells per well) with 100 μL complete Dulbecco's Modified Eagle Medium (DMEM) per well and cultured for 24 h. The cells were incubated with predetermined amounts of bare polymeric SAs or DOX-loaded SAs at 37 °C and 5% CO_2 for 48 h. Then, 20 μL of 5 mg/mL MTT solution in phosphate buffered saline (PBS) was added to each well and incubated for another 4 h. The medium was removed carefully, and generated MTT−formazan was dissolved in 200 μL of DMSO per well. The absorbance was measured on a Bio-Rad iMark at a wavelength of 595 nm. The relative cell viability (%) was determined by comparing the absorbance at 595 nm with control wells incubated with complete DMEM. Data are presented as mean ± standard deviation (SD) ($n = 4$).

CMC Measurement. The critical micelle concentration (cmc) was determined using pyrene as a fluorescence probe.[43] The fluorescence excitation spectra of pyrene were recorded by a Hitachi F-4600 fluorescence spectrophotometer (Hitachi High-Technologies Corporation, Tokyo, Japan). The emission wavelength was set at 390 nm. The concentration of polymers varied from 1.0 × 10^{-5} to 0.6 mg/mL, and the concentration of pyrene was fixed at 8.0 × 10^{-7} mol/L. The cmc was estimated as the cross-point when extrapolating the intensity ratio I_{338}/I_{335} at low and high concentration regions (Figure S2).

■ RESULTS AND DISCUSSION

Synthesis and Characterization of Hyperblock and Hypergraft Copolymers. In this study, to investigate the effect of chain architecture, two amphiphilic hyperbranched polymers (AHPs) with a similar weight fraction of hydrophobic/hydrophilic composition but different block distributions were prepared; to study the effect of block composition, the block length was systematically varied for a given hyperbranched structure. The biocompatible poly(ε-caprolac-

tone) (PCL) was used as hydrophobic building block. We chose poly[tri(ethylene glycol) methyl ether acrylate] (PTEGMA) as hydrophilic building block because the polymerization process is well controlled and the end group can be easily modified. Scheme 2 shows our strategy of synthesizing AB$_2$-type macromonomers and the target Hyperblock and Hypergraft copolymers. The Hyperblock (HB-PCL-b-PTEGMA) is made from PCL-b-PTEGMA diblock AB$_2$-type macromonomer, and the inserted PCL and PTEGMA blocks are randomly distributed along the backbones, while the Hypergraft (HB-PCL-g-PTEGMA) is composed of a hyperbranched PCL core and grafted PTEGMA chains on periphery.

The synthesis started from two functional initiators, as shown in Scheme 2. The initiators I (Figure S3) and II were prepared according to our previous protocols.[35] For the synthesis of Hyperblock HB-PCL-b-PTEGMA and Hypergraft HB-PCL-g-PTEGMA, two kinds of functional AB$_2$-type macromonomers were prepared, namely, PCL-b-PTEGMA-2N$_3$ (Scheme 2a) and PCL-2N$_3$ (Scheme 2b). For the synthesis of PCL-b-PTEGMA-2N$_3$, the diblock precursor PCL-b-PTEGMA-OH-Br was first prepared by a combination of ring-opening polymerization (ROP) of CL and subsequent atom transfer radical polymerization (ATRP) of TEGMA. Further functional modification of the end hydroxyl group of PCL block and azidation substitution furnished the diblock macromonomer PCL-b-PTEGMA-2N$_3$ with one alkyne group in middle of two blocks and two azide groups located at the end of each block. The synthesis of PCL-2N$_3$ is much simpler; namely, a combination of ROP of CL, functional modification, and azidation substitution results in the final PCL-2N$_3$ macromonomer with one alkyne group in the chain center and two azide groups located at the two chain ends.

In the syntheses, the ROP and ATRP polymerization processes were all conducted in a living manner. The successful preparation of macromonomers PCL-b-PTEGMA-2N$_3$ and PCL-2N$_3$ with different chain lengths and block compositions was confirmed by various characterization methods. Namely, Figure 1 demonstrates that the resultant macromonomers
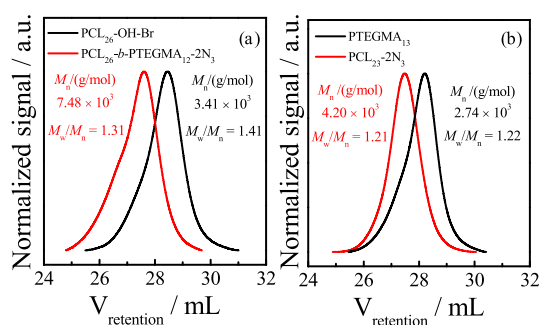

Figure 1. GPC curves of (a) PCL$_{26}$-OH-Br and PCL$_{26}$-b-PTEGMA$_{12}$-2N$_3$ and (b) PTEGMA$_{13}$ and PCL$_{23}$-2N$_3$.

PCL$_{26}$-b-PTEGMA$_{12}$-2N$_3$ and PCL$_{23}$-2N$_3$ own relatively narrow molar mass distributions with polydispersity indexes (M_w/M_n) of ∼1.3 and ∼1.2, respectively. It is worth noting that the monomer conversion during polymerization was maintained below 60% to ensure high end-group functionality. The number-average molar masses (M_n) were determined to be ∼7.5 × 10^3 and ∼4.2 × 10^3 g/mol for these two macromonomers.

In addition to the visual GPC measurements, the two macromonomers and other intermediate polymers were also characterized by ¹H NMR in detail. Figures 2 and 3 summarize
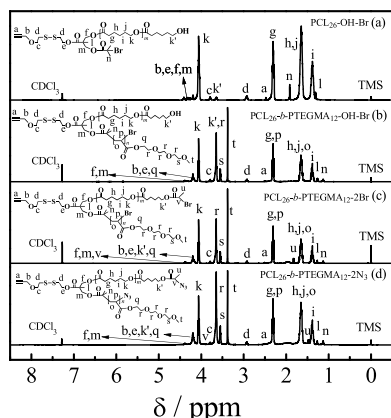

Figure 2. ¹H NMR spectra of (a) PCL$_{26}$-OH-Br, (b) PCL$_{26}$-b-PTEGMA$_{12}$-OH-Br, (c) PCL$_{26}$-b-PTEGMA$_{12}$-2Br, and (d) macromonomer PCL$_{26}$-b-PTEGMA$_{12}$-2N$_3$.
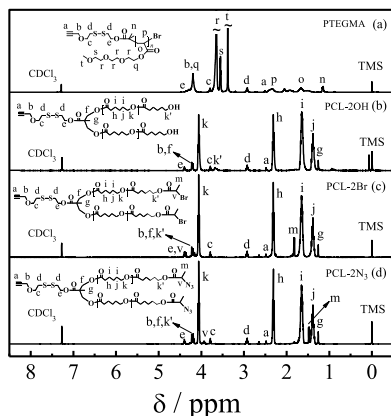
Figure 3. ¹H NMR spectra of (a) PTEGMA$_{13}$, (b) PCL$_{23}$-2OH, (c) PCL$_{23}$-2Br, and (d) macromonomer PCL$_{23}$-2N$_3$.

the corresponding ¹H NMR results for PCL$_{26}$-b-PTEGMA$_{12}$-2N$_3$ and PCL$_{23}$-2N$_3$, respectively. The successful polymerization and postpolymerization modification can be clearly reflected in the presence of new peaks and obvious signal shift of existing peaks, respectively. Detailed notation is made to assign the peaks to the corresponding protons of each intermediate polymer. Figure 2a shows that the characteristic peaks located at ∼4.00 ppm ("k") and ∼3.65 ppm ("k′") are attributed to the protons of −CH$_2$OOC− and −CH$_2$−OH on the chain backbone and the chain end of each PCL block, respectively. PCL$_{26}$-b-PTEGMA$_{12}$-OH-Br was obtained by subsequent ATRP of the monomer TEGMA. The new peaks located at ∼3.55 ppm ("s") and ∼3.38 ppm ("t") in Figure 2b are attributed to the protons of TEGMA repeating unit. After functional modifications by bromination reaction, the new peaks in Figure 2c located at 1.82 ppm ("u") and 4.35 ppm ("v") indicate the success of this reaction. After the azidation reaction of PCL$_{26}$-b-PTEGMA$_{12}$-2Br with NaN$_3$, we got the final amphiphilic macromonomer PCL$_{26}$-b-PTEGMA$_{12}$-2N$_3$. The ¹H NMR spectrum is shown in Figure 2d. The peaks "u" and "v" both shift to lower position compared with PCL$_{26}$-b-PTEGMA$_{12}$-2Br. Moreover, the similar chemical shift changes

after the synthesis process of PCL$_{23}$-2N$_3$ are shown in Figure 3. Note that GPC result can only provide apparent values for molar mass related information if we consider the difference of hydrodynamic sizes between PCL/PTEGMA and polystyrene calibration standards. Therefore, ¹H NMR spectra were further used to extract the information about real molar mass and relative mass fraction of each block for macromonomers PCL$_{26}$-b-PTEGMA$_{12}$-2N$_3$ and PCL$_{23}$-2N$_3$. Principally, the relative intensity of integral area of the signals from initiating site, end-group, and monomer units can be used to calculate the real degree of polymerization (DP) for PCL and PTEGMA blocks. The value of DP of PCL segment was calculated as

$$DP_{PCL} = (A_k + A_{k'})/A_{k'} \tag{4}$$

where A_k and $A_{k'}$ represent the integration area of peaks k and k', respectively. Similarly, the values of DP of PTEGMA block and macromonomer PCL-2N$_3$ can be calculated as

$$DP_{PTEGMA} = 2A_s/A_d \tag{5}$$

$$DP_{PCL} = 2(A_k + A_{k,})/A_{k'} \tag{6}$$

Following this principle, for PCL$_{26}$-b-PTEGMA$_{12}$-2N$_3$, the real DP value of PCL and PTEGMA blocks was found to be ∼26 and ∼12, respectively, while the DP value of PCL was found to be ∼23 for PCL$_{23}$-2N$_3$. In addition, the alkyne-functional PTEGMA with different lengths prepared by ATRP was further used as grafting chains for the preparation of Hypergraft HB-PCL-g-PTEGMA. By taking PTEGMA$_{13}$ as an example, the ¹H NMR result demonstrates that the DP value for PTEGMA$_{13}$ is ∼13, which is similar to the PTEGMA block in the diblock copolymer PCL$_{26}$-b-PTEGMA$_{12}$. The corresponding GPC and ¹H NMR curves of PTEGMA$_{13}$ are shown in Figures 1b and 3a.

The interchain coupling of macromonomer PCL$_{26}$-b-PTEGMA$_{12}$-2N$_3$ was conducted with the CuBr/PMDETA catalyst system to produce Hyperblock HB-PCL$_{26}$-b-PTEG-MA$_{12}$. Similarly, the hydrophobic hyperbranched core of Hypergraft HB-PCL$_{23}$-g-PTEGMA$_{13}$ was prepared from macromonomer PCL$_{23}$-2N$_3$. Figure 4 shows clear shifts of
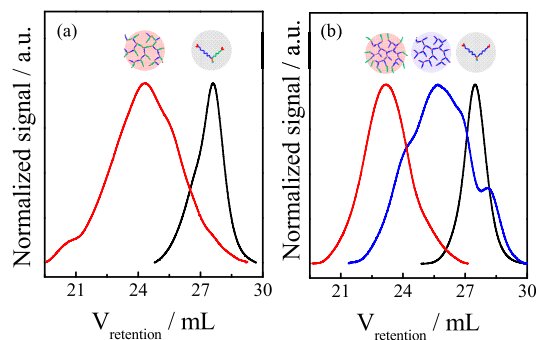
Figure 4. GPC curves of (a) unfractionated Hyperblock HB-PCL$_{26}$-b-PTEGMA$_{12}$ and macromonomer PCL$_{26}$-b-PTEGMA$_{12}$-2N$_3$ and (b) fractionated Hypergraft HB-PCL$_{23}$-g-PTEGMA$_{13}$, HB-PCL$_{23}$, and PCL$_{23}$-2N$_3$.

elution peaks in GPC curves for macromonomers PCL$_{26}$-b-PTEGMA$_{12}$-2N$_3$ and PCL$_{23}$-2N$_3$ after click reaction (red curves), signifying the formation of hyperbranched chains. For the preparation of Hypergraft HB-PCL$_{23}$-g-PTEGMA$_{13}$, an additional click reaction between the alkyne group of PTEGMA$_{13}$ and residual azide groups of PCL hyperbranched

core was carried out to couple the hydrophilic PTEGMA onto the periphery of PCL hyperbranched core. The GPC curve further shifts to a lower retention time, indicating the successful grafting process. All the apparent molar mass information about related samples is summarized in Table S1.

Figure 5 shows the ^1H NMR spectra of two hyperbranched model systems. As shown, the observed new peak located at
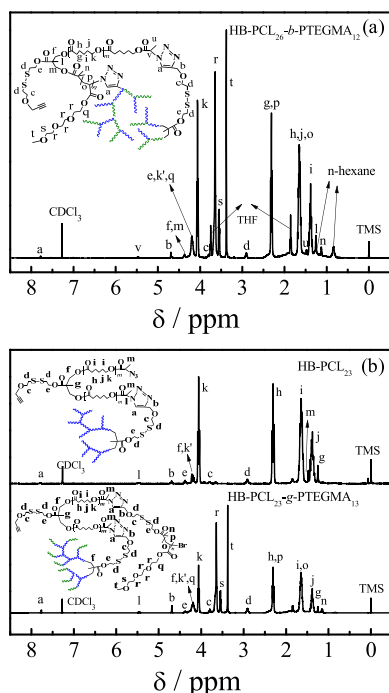

Figure 5. ^1H NMR spectra of (a) Hyperblock HB-PCL$_{26}$-b-PTEGMA$_{12}$ and (b) hyperbranched core HB-PCL$_{23}$ and Hypergraft HB-PCL$_{23}$-g-PTEGMA$_{13}$.

~7.8 ppm ("a") can be attributed to the proton signal from the triazole ring,[44] indicating the formation of a triazole five-membered ring, which is also reflected in the significant chemical shifts of protons "b" and "v" from the branching linkages and terminal groups of macromonomers. Figure S4 further shows the FTIR spectra of macromonomers, hyperbranched polymers, and other intermediate polymers. Obviously, the strong vibration at ~2100 cm^{-1} can be ascribed to azide asymmetric stretching vibration,[35,44] reflecting the successful substitution of bromine groups by azide groups for macromonomers PCL$_{26}$-b-PTEGMA$_{12}$-2N$_3$ and PCL$_{23}$-2N$_3$. After the click reaction, the vibration intensity decreases, reflecting the decrease in the mass fraction of azide groups during polycondensation process. The significant difference between final Hyperblock HB-PCL$_{26}$-b-PTEGMA$_{12}$ and Hypergraft HB-PCL$_{23}$-g-PTEGMA$_{13}$ is indicated by the stretching vibration intensity of azide groups. The vibration signal of azide groups of HB-PCL$_{23}$-g-PTEGMA$_{13}$ seems to totally disappear after the grafting process, indicating the high grafting efficiency (up to 90%). Overall, the structures of resultant Hyperblock HB-PCL$_{26}$-b-PTEGMA$_{12}$ and Hypergraft HB-PCL$_{23}$-g-PTEGMA$_{13}$ amphiphilic copolymers were confirmed by a combination of GPC, ^1H NMR, and FTIR characterization. The above results clearly demonstrate that the two model hyperbranched systems have a similar PCL/PTEGMA composition but different block sequences and distributions, which can be further used as meaningful

reference models for the investigation of how the block sequence and distribution affect the degradation behavior.

For HB-PCL-b-PTEGMA, we systematically regulated the chain length of the hydrophilic PTEGMA block in the macromonomer to obtain a set of HB-PCL$_x$-b-PTEGMA$_y$ with almost identical hydrophobic block (x = 25−26) but with different PTEGMA block lengths (y = 6, 12, and 26). For HB-PCL$_{x'}$-g-PTEGMA$_{y'}$, we also got a set of samples with identical hydrophobic block (x' = 23−25) but with different PTEGMA block lengths (y' = 12 and 21). The detailed GPC characterization results of these samples are shown in Figure S5 (^1H NMR and FTIR results are not shown), and their chain parameters are summarized in Table S3.

Degradation of Hyperblock and Hypergraft Copolymers in an Organic Solvent. As mentioned earlier, each branching point of HB-PCL-b-PTEGMA and HB-PCL-g-PTEGMA contains only one cleavable disulfide bond. All the degradable sites are perfectly distributed along the hyperbranched backbone. Following our previous study of degradable hyperbranched polystyrene, we preferred to choose dithiothreitol (DTT)[45] as the reducing agent because (1) its induced disulfide reduction is highly efficient because of its high conformational tendency to form a six-membered ring and (2) it is soluble in a range of solvents such as THF and water, providing an opportunity to carry out the experiments in both nonaqueous and aqueous solutions.

Hyperblock HB-PCL$_{26}$-b-PTEGMA$_{12}$ and Hypergraft HB-PCL$_{23}$-g-PTEGMA$_{13}$ were used as model samples to investigate the degradation behavior of hyperbranched copolymers in organic solvent. In experiments, the degradation of model samples in THF solution (10 mM DTT) was monitored quantitatively by GPC. As shown in Figures 6a and
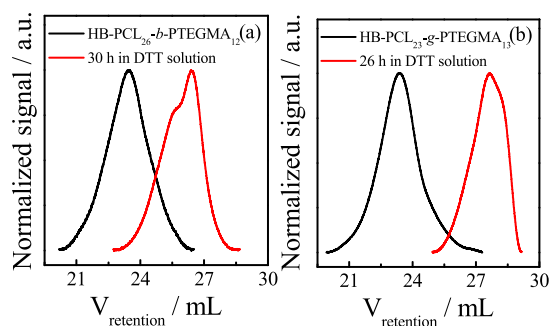

Figure 6. GPC curves for the two AHPs before and after degradation in THF at [DTT] = 10 mM: (a) fractionated HB-PCL$_{26}$-b-PTEGMA$_{12}$ and (b) fractionated HB-PCL$_{23}$-g-PTEGMA$_{13}$.

6b (data for reference samples are shown in Figure S6), the degradation of HB-PCL$_{26}$-b-PTEGMA$_{12}$ and HB-PCL$_{23}$-g-PTEGMA$_{13}$ is almost accomplished within ~30 h.[46] The apparent molecular information about the degradation products is summarized in Table S2. However, the nonaqueous solution is not the appropriate choice to mimic the real environment of drug releasing process. Taking the advantages of biocompatibility and water solubility of prepared Hyperblock HB-PCL-b-PTEGMA and Hypergraft HB-PCL-g-PTEGMA, we further monitored the degradation behavior of their self-assembly amphiphiles (SAs) in aqueous solutions (10 mM DTT) by stand-alone laser light scattering (LLS). The changes in the relative scattering intensity (I_t/I_0) and hydrodynamic radius ($\langle R_h \rangle$) were monitored over degradation time.
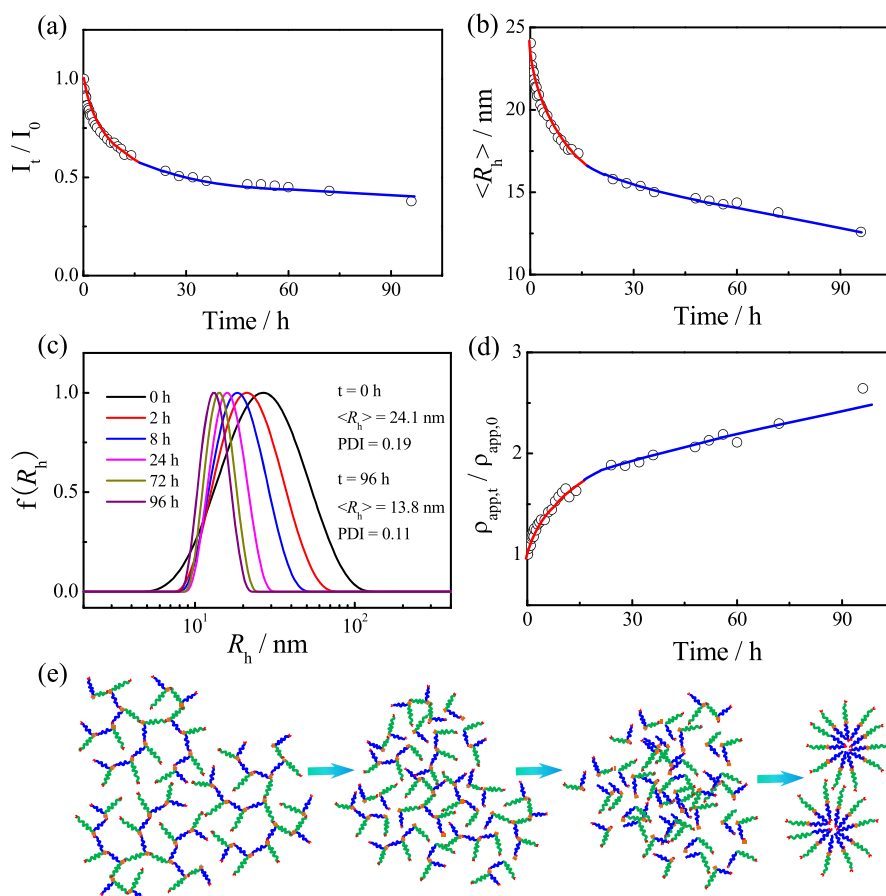
Figure 7. Degradation time (t) dependence of (a) ratio (I_t/I_0) of scattering intensities at $t = t$ (I_t) and $t = 0$ (I_0), (b) average hydrodynamic radius $\langle R_h \rangle$, (c) hydrodynamic radius distribution $f(R_h)$, and (d) ratio ($\rho_{app,t}/\rho_{app,0}$) of apparent chain segment densities at $t = t$ ($\rho_{app,t}$) and $t = 0$ ($\rho_{app,0}$) for HB-PCL$_{26}$-b-PTEGMA$_{12}$ SAs in aqueous solutions with [DTT] = 10 mM, where $C_{polymer}$ = 0.6 mg/mL. (e) Schematic illustration of degradation process for HB-PCL-b-PTEGMA SAs in aqueous solution.

Degradation of Hyperblock and Hypergraft Copolymers in Aqueous Solutions: The Effect of Chain Architecture.

Using HB-PCL$_{26}$-b-PTEGMA$_{12}$ and HB-PCL$_{23}$-g-PTEGMA$_{13}$ with a similar block composition as model samples, we first investigated how the block distribution influences the degradation behavior of hyperbranched SAs in aqueous solutions. The results of degradation study for HB-PCL$_{26}$-b-PTEGMA$_{12}$ SAs are summarized in Figure 7. Figure 7a shows that the relative scattering intensity I_t/I_0 decreases rapidly in the first 20 h and then smoothly with degradation time, signifying a two-step degradation process (red and blue lines). The two-step degradation process can also be reflected in the evolution of $\langle R_h \rangle$ as a function of degradation time in Figure 7b, where the $\langle R_h \rangle$ of HB-PCL$_{26}$-b-PTEGMA$_{12}$ SAs rapidly decreases from ~24 to ~17 nm within the first 20 h, and subsequently a smooth decrease to ~12 nm can be observed in the following 80 h. Moreover, Figure 7c shows that the hydrodynamic radius distribution $f(R_h)$ becomes narrower as time proceeds, signifying the uniformity of the SAs composed of degradation products. It is worth noting that we also measured the $f(R_h)$ of SAs composed of diblock PCL$_{26}$-b-PTEGMA$_{12}$ macromonomer in aqueous solution for comparison (Figure S7), which shows similar $\langle R_h \rangle$s and polydispersity indexes to those of degradation products, implying that the molecular structure of degradation products is similar to that of the macromonomer.

Figure 7d further shows that the relative apparent chain density ($\rho_{app,t}/\rho_{app,0}$), defined as $\rho_{app,t}/\rho_{app,0} = (I_t/\langle R_h \rangle^3)_{t=t}/(I_t/\langle R_h \rangle^3)_{t=0}$, gradually increases with the degradation time. This change reflects that the SAs made of huge hyperbranched chains own a much lower apparent chain density than that of initial linear macromonomer, which can be attributed to the more compact structure of SAs composed of diblock amphiphiles. By taking $R_h \sim M^{0.5}$ into $\rho \sim M/R_h^3$ for hyperbranched chains in a good solvent,[47] we can get $\rho \sim M^{-0.5}$; i.e., a polymer chain with a smaller molecular weight has a higher apparent chain density. Thus, the apparent chain density increases with the degradation of Hyperblock copolymers. It is also worth noting that the intermediate and final degradation product (PCL$_{26}$-b-PTEGMA$_{12}$) is not able to be further cleaved into individual PCL and PTEGMA blocks as they are chemically bonded, which leads to an unchanged hydrophobic/hydrophilic balance for SAs during the whole degradation process. At any point, no turbidity was observed in the SAs aqueous solution, even at the end of experiment. The degradation process for Hyperblock HB-PCL$_{26}$-b-PTEGMA$_{12}$ is schematically illustrated in Figure 7e.

In contrast, HB-PCL$_{23}$-g-PTEGMA$_{13}$ SAs showed different degradation kinetics as shown in Figures 8a−d. We hypothesize that this difference originates from the different branching patterns of the two model systems; namely, the PCL/PTEGMA blocks are randomly distributed within the whole framework of Hyperblock HB-PCL-b-PTEGMA, while
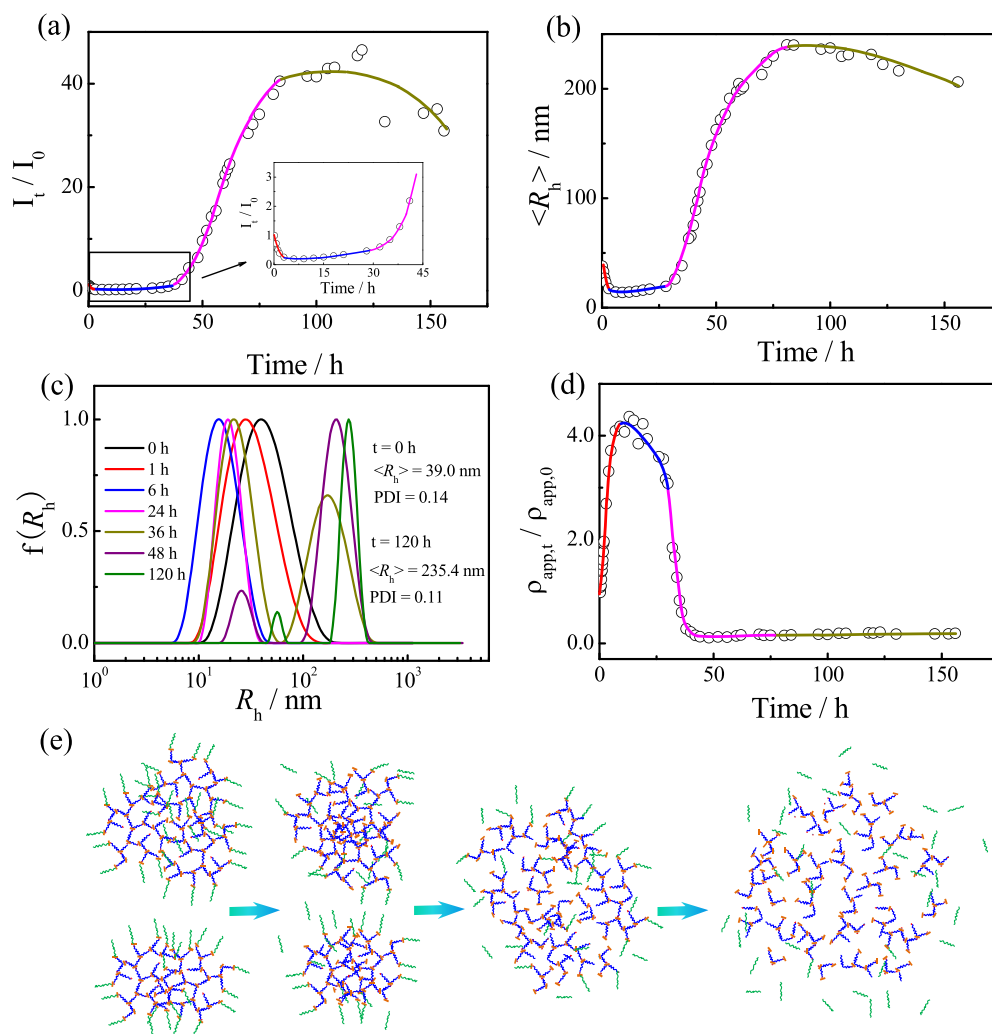
Figure 8. Degradation time (t) dependence of (a) ratio (I_t/I_0) of scattering intensities $t = t$ (I_t) and $t = 0$ (I_0), (b) average hydrodynamic radius $\langle R_h \rangle$, (c) hydrodynamic radius distribution $f(R_h)$, and (d) ratio ($\rho_{app,t}/\rho_{app,0}$) of apparent chain segment densities at $t = t$ ($\rho_{app,t}$) and $t = 0$ ($\rho_{app,0}$) for HB-PCL$_{23}$-g-PTEGMA$_{13}$ SAs in aqueous solutions with [DTT] = 10 mM, where $C_{polymer}$ = 0.6 mg/mL. (e) Schematic illustration of degradation process for HB-PCL-g-PTEGMA SAs in aqueous solution.

spatially separated hydrophobic PCL and hydrophilic PTEGMA domains exist for Hypergraft HB-PCL-g-PTEGMA. Relying on the observed different change rates in light scattering intensity and size, the whole degradation process can be divided into four time intervals: (i) $t < 4$ h, a fast degradation process was observed, reflected in the significant decrease of I_t/I_0 from ~1.0 to ~0.3 (Figure 8a) and size from ~24 to ~16 nm (Figures 8b,c); (ii) 4 h < t < 29 h, the determined values of I_t/I_0 and $\langle R_h \rangle$ weakly increase with time; (iii) 29 h < t < 82 h, I_t/I_0 and $\langle R_h \rangle$ start to rapidly increase with degradation time, ~12 times increase in $\langle R_h \rangle$ was observed; (iv) $t > 82$ h, the average size of assemblies slowly decreases with degradation time.

Reasonably, the change during the first time interval could be mainly attributed to the degradation process of the PTEGMA shell, where the DTT molecules can quickly permeate the periphery of Hypergraft HB-PCL$_{23}$-g-PTEGMA$_{13}$ due to the hydrophilic nature of PTEGMA shells. The phenomenon of second time interval can be related to the balance between degradation and aggregation of SAs. As mentioned earlier, the hydrophobic/hydrophilic balance is almost constant for Hyperblock HB-PCL$_{26}$-b-PTEGMA$_{12}$

during the degradation process, while this is not the case for Hypergraft HB-PCL$_{23}$-g-PTEGMA$_{13}$. As shown in Figure 8e, there is always one disulfide linkage between PCL and PTEGMA blocks, which leads to the fact that both the PCL and PTEGMA blocks in hyperbranched assemblies can be independently degraded, inevitably leading to significant change in hydrophobic/hydrophilic balance of remaining assemblies. Consequently, the weight fraction of hydrophobic PCL blocks on some of Hypergraft chains and their assemblies will significantly increase as the degradation proceeds, resulting in the disturbance of the hydrophobic/hydrophilic balance. Thermodynamically, aggregation of unstable SAs with high content of PCL blocks inevitably leads to an increase in both apparent molar mass and hydrodynamic radius of SAs.

Furthermore, it is not difficult to understand the experimental phenomenon in the third time interval between 29 h < t < 82 h, where the cleavage of disulfide bonds further leads to serious imbalance of hydrophobicity/hydrophilicity and strong aggregation of degradation products. It is resonable to predict that the aggregation process will finally determine the apparent molar mass and size of SAs existing in the system. Indeed, macroscopic precipitates were observed at the bottom
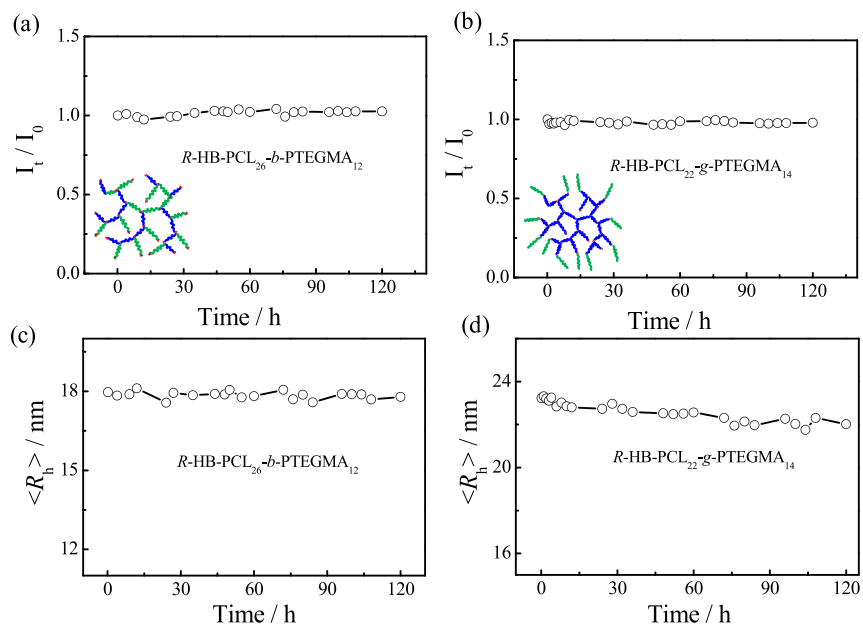
Figure 9. Degradation time (t) dependence of (a) and (b) ratio (I_t/I_0) of scattering intensities at $t = t$ (I_t) and $t = 0$ (I_0); (c) and (d) average hydrodynamic radius $\langle R_h \rangle$ for R-HB-PCL$_{26}$-b-PTEGMA$_{12}$ and R-HB-PCL$_{22}$-g-PTEGMA$_{14}$ SAs in aqueous solutions with [DTT] = 10 mM.
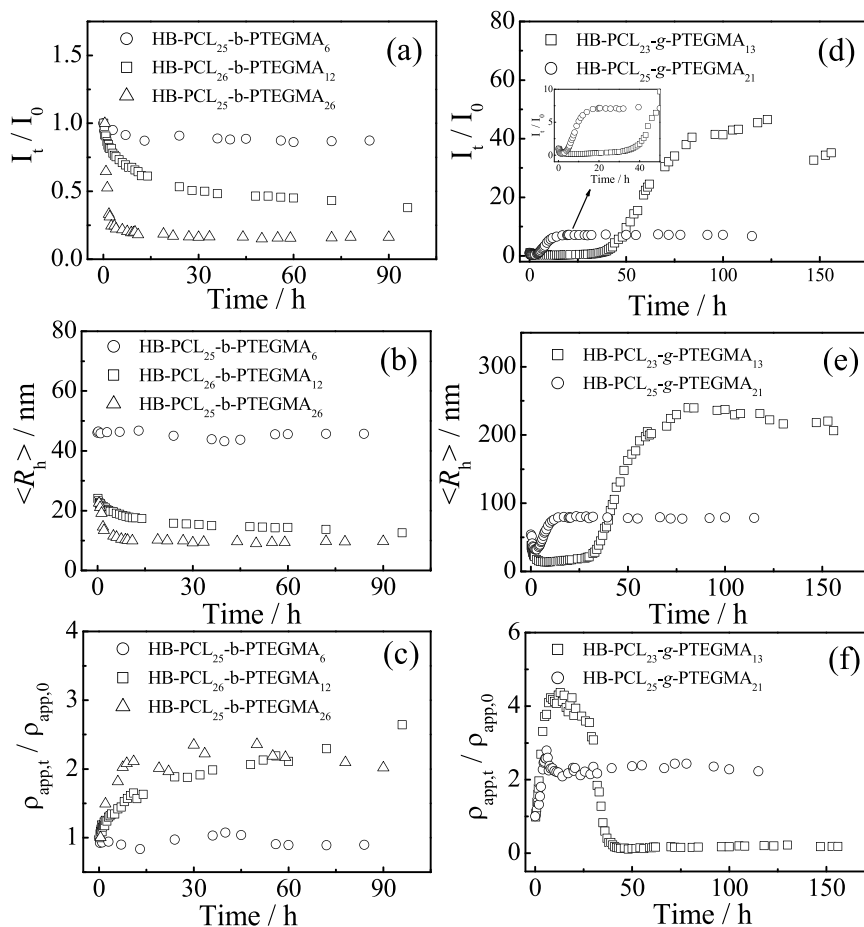
Figure 10. Degradation time (t) dependence of (a, d) ratio (I_t/I_0) of scattering intensities at $t = t$ (I_t) and $t = 0$ (I_0); (b), (e) average hydrodynamic radius $\langle R_h \rangle$; (c, f) ratio ($\rho_{app,t}/\rho_{app,0}$) of chain segment densities at $t = t$ ($\rho_{app,t}$) and $t = 0$ ($\rho_{app,0}$) for SAs of HB-PCL-b-PTEGMA and HB-PCL-g-PTEGMA with different compositions in aqueous solutions with [DTT] = 10 mM, where $C_{polymer} = 0.6$ mg/mL.

of experimental vial after 100 h, further supporting our explanation.

The changes in apparent chain density can be interpreted as follows: (1) For the first time interval, the degradation of

PTEGMA shell leads to a compact structure. Thus, the apparent chain density increases. (2) For the second time interval, both of the disulfide linkages in the shell and core degrade. However, the degradation of disulfide linkages in the hydrophobic core leads to a loose structure. The combination effect shows a little decrease in the apparent chain density. (3) For the third and the fourth time intervals, more and more disulfide linkages were degraded. Large but loose aggregates were generated, so the M increased and the apparent chain density decreased as $\rho \sim M^{-0.5}$. Moreover, it should be noted that for the fourth time interval the measured chain apparent density is related to the species suspended in the solutions due to the formation of precipitates.

The TEM data (Figures S8 and S9) also show similar evolution during the course of degradation in an aqueous phase. On the basis of the above results, it is clear that even for hyperbranched systems with a similar block composition, the difference of the sequence and spatial distribution of hydrophobic/hydrophilic blocks can also lead to distinct degradation behavior of hyperbranched assemblies. The above results also highlight the importance of utilizing model samples with controlled branching structure and degradable sites for the structure−property study. Overall, the Hypergraft HB-PCL-*g*-PTEGMA presented a much more complicated degradation process.

Up until now, the result has shown how the branching pattern of amphiphilic hyperbranched assemblies affects their degradation in aqueous solutions and quantitatively analyzed the chain architecture−degradation property relation. However, for unambiguous conclusion, the reference hyperbranched systems without cleavable disulfide bonds should also be studied for meaningful comparison. Thus, we further prepared two reference samples without disulfide linkages named *R*-HB-PCL$_{26}$-*b*-PTEGMA$_{12}$ and *R*-HB-PCL$_{22}$-*g*-PTEGMA$_{14}$ for control experiments. The ^{1}H NMR, FTIR, and GPC measurements confirmed the structures of the initiators, macromonomers, and resultant hyperbranched polymers (Figures S10−S16), and the synthesis details can be found in Schemes S1 and S2.

Overall, compared with HB-PCL$_{26}$-*b*-PTEGMA$_{12}$ and HB-PCL$_{23}$-*g*-PTEGMA$_{13}$, the two reference samples own a similar composition of hydrophobic/hydrophilic block and overall average molar mass (Figure S15). Moreover, the size of SAs composed of the two reference AHPs is determined to be ~18 and ~23 nm, respectively, very close to the previously measured sizes for HB-PCL$_{26}$-*b*-PTEGMA$_{12}$ and HB-PCL$_{23}$-*g*-PTEGMA$_{13}$, demonstrating that the existing disulfide linkages on the branching units actually play negligible role in affecting the hydrophobic/hydrophilic balance. More importantly, the LLS study of degradation kinetics of the two reference AHPs shows no evidence for their degradation in aqueous solutions, reflected by the constant scattering intensity and average hydrodynamic size (Figure 9), further proving that the observed decrease of light scattering intensity and average hydrodynamic size is indeed originated from the cleavage of disulfide bonds instead of the degradation of PCL block.

Degradation of Hyperblock and Hypergraft Copolymers in Aqueous Solutions: The Effect of Block Composition. For a given chain architecture, the block composition is also important for the regulation of degradation behavior of resultant hyperbranched amphiphiles. Thus, we studied how the hydrophilic block length affects the self-

assembly and degradation of Hyperblock and Hypergraft copolymers. As shown in Figures 10a,b for Hyperblock HB-PCL$_x$-*b*-PTEGMA$_y$, as the DP of PTEGMA increases from 6 to 26, the degradation rate significantly increases, reflected in the evolutions of I_t/I_0 and $\langle R_h \rangle$ with degradation time. Specifically, no obvious change was observed for HB-PCL$_{25}$-*b*-PTEGMA$_6$ with shortest PTEGMA block length, and we attributed this phenomenon to frozen state of the amphiphilic SAs induced by the strong hydrophobic interaction between PCL$_{25}$ blocks. Namely, even the cleavable disulfide bonds could be attacked by DTT molecules; the diffusion of degradation product PCL$_{25}$-*b*-PTEGMA$_6$ might be completely prohibited due to the much strong hydrophobic interaction among PCL$_{25}$ blocks in PCL$_{25}$-*b*-PTEGMA$_6$. Figure 10c quantitatively shows that the apparent density monotonically increases with degradation time for HB-PCL$_{26}$-*b*-PTEGMA$_{12}$ and HB-PCL$_{25}$-*b*-PTEGMA$_{26}$.

Figures 10d−f summarize the corresponding results for Hypergraft copolymers HB-PCL$_{x'}$-*g*-PTEGMA$_{y'}$. Clearly, a four-step degradation process was also observed for HB-PCL$_{25}$-*g*-PTEGMA$_{21}$ with longer PTEGMA block length. For HB-PCL$_{25}$-*g*-PTEGMA$_{21}$, the transition points of the degradation curve shift to earlier time points, reflecting the accelerated degradation process, but the number of transition points is unchanged as the PTEGMA block length increases, indicating that the structures for SAs with different PTEGMA block lengths are almost similar.

The above studies unambiguously reveal that the factors of chain architecture and block composition play different roles for the regulation of degradation behavior of long-subchain hyperbranched SAs; namely, the degradation model is mainly affected by the chain architecture and the structure of resultant SAs, while for a given architecture, the degradation rate can be regulated by systematically varying the block composition. Overall, the above result also demonstrates that the synergistic effect of the two factors determine the details of degradation behavior of hyperbranched SAs.

Thermal Properties of Hyperblock and Hypergraft Copolymers in Bulk. Another important factor that may be closely related to the degradation behavior of hyperbranched assemblies is the crystallization of the PCL block. It is known that PCL is a semicrystalline polymer; thus, its crystallization property actually plays an important role in determining both permeability and biodegradability of bulk materials,[48,49] which may further influence the degradation behavior of PCL-based assemblies in aqueous solutions. To clarify whether it is the block sequence and distribution or the crystallization of PCL block that induces the difference in observed degradation behavior of the two model systems, DSC measurements were conducted to investigate the crystallization property of these powder samples. Figure 11 shows the obtained DSC curves during reheating. The degree of crystallinity (χ_c) of Hyperblock HB-PCL$_{26}$-*b*-PTEGMA$_{12}$ decreases from 41.6% to 30.4% compared with its macromonomer, indicating that the crystallization of PCL segments is suppressed by the branching structure, to some extent. However, the observed phenomenon is different from our previous work[35] for Hyperblock HB-PCL-*b*-PS, where the crystallization of PCL segments in HB-PCL-*b*-PS was completely suppressed, and no obvious crystallization behavior was observed in DSC measurement. This inconsistency can be attributed to the fact that PTEGMA block is more flexible as compared to PS block. For the Hypergraft HB-PCL-*g*-PTEGMA system shown in Figure 11b, the value of χ_c
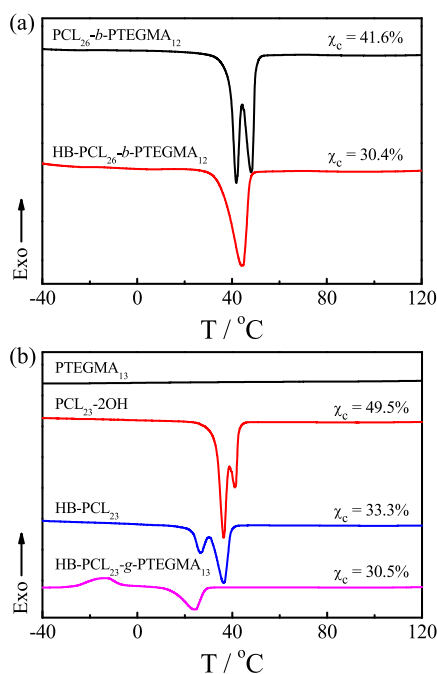
Figure 11. DSC curves (10 °C/min) during reheating of (a) Hyperblock HB-PCL$_{26}$-*b*-PTEGMA$_{12}$ and PCL$_{26}$-*b*-PTEGMA$_{12}$-2N$_3$. (b) Hypergraft HB-PCL$_{23}$-*g*-PTEGMA$_{13}$, PCL$_{23}$-2OH, and other intermediate polymers.

of hyperbranched PCL core is also found to be smaller than that of the macromonomer. After grafting the hydrophilic PTEGMA blocks to form the final HB-PCL$_{23}$-*g*-PTEGMA$_{13}$, the determined χ_c shows no obvious difference compared with the hyperbranched PCL core alone. The above observation further supports that as flexible segments,[50] PTEGMA blocks have little impact on the crystallization of PCL blocks. Overall, the determined degrees of crystallinity of Hyperblock HB-PCL$_{26}$-*b*-PTEGMA$_{12}$ (χ_c = 30.4%) and Hypergraft HB-PCL$_{23}$-*g*-PTEGMA$_{13}$ (χ_c = 30.5%) are almost similar to each other, further indicating that the observed difference in their degradation behavior in solution phase is unlikely to be affected by the crystallization property of the PCL block. In addition, the two reference AHPs *R*-HB-PCL$_{26}$-*b*-PTEGMA$_{12}$ and *R*-HB-PCL$_{22}$-*g*-PTEGMA$_{14}$ also show similar degrees of crystallinity (Figure S17, χ_c = 33.4% and χ_c = 32.1%), supporting the negligible influence of disulfide bonds on the crystallization of PCL.

Moreover, the TGA test was also performed for HB-PCL$_{26}$-*b*-PTEGMA$_{12}$ and HB-PCL$_{23}$-*g*-PTEGMA$_{13}$. Data are shown in Figure S18. The temperature and weight change of their decomposition reactions are almost the same. No significant differences were found between these two structures. The results may be ascribed to their similar chemical compositions.

Studies of Drug Loading and Release. The drug loading related properties including drug loading content (DLC) and drug loading efficiency (DLE) were also studied, where DOX was used as model hydrophobic drug. The R_h values of drug loaded SAs, DLC, and DLE results are summarized in Table 1. The R_h value of HB-PCL$_{23}$-*g*-PTEGMA$_{13}$-DOX is ∼135 nm (Figure S19), which has a large difference with its bare SAs (∼39 nm). This difference can also be seen in TEM results (Figure S20). A possible explanation for this could be ascribed to their different branching patterns of the two model systems (Scheme 3). Compared with Hyperblock SAs, the Hypergraft

Table 1. DLC and DLE of DOX Loaded SAs

sample	$\langle R_h \rangle$ (nm)	DLC (%)	DLE (%)
HB-PCL$_{26}$-*b*-PTEGMA$_{12}$-DOX	21.9	5.3	28.0
HB-PCL$_{23}$-*g*-PTEGMA$_{13}$-DOX	135.1	3.0	15.3

SAs own much larger and more continuous hydrophobic domains, which probably makes the assembled structures more sensitive to hydrophobic−hydrophilic balance. Consequently, the size change for Hypergraft SAs is more significant after drug loading. This difference may also induce the fact that HB-PCL$_{26}$-*b*-PTEGMA$_{12}$ possesses higher DLC and DLE than that of HB-PCL$_{23}$-*g*-PTEGMA$_{13}$. Overall, both of the systems have considerable DLC[19,22] but not that much as those reported values in previous literature.[51,52] In addition, the stability results (Figure S21) show that the average hydrodynamic radii $\langle R_h \rangle$s of drug-loaded SAs HB-PCL$_{26}$-*b*-PTEGMA$_{12}$-DOX and HB-PCL$_{23}$-*g*-PTEGMA$_{13}$-DOX remain constant within 72 h in PBS solutions with or without the addition of 10% fetal bovine serum, indicating their high stability.

In addition to the careful investigation of degradation behavior, we also performed a study of the drug release of drug-loaded SAs and the cell viability of hyperbranched assemblies with and without drug loading using HeLa cells as model cells. The drug release results indicate that Hyperblock copolymer nanostructures have a faster release rate than Hypergraft copolymer nanostructures, as shown in Figure S22. For Hyperblock copolymers, the amphiphilic blocks may release drugs in the hydrophobic domains easily once degraded from the mother structure. For Hypergraft copolymers, the hydrophobic core maintains compact structure even after some disulfide groups were degraded according to the degradation data. Figure 12a (also Figure S23) shows that without drug loading the cell viability for HB-PCL$_{26}$-*b*-PTEGMA$_{12}$ and HB-PCL$_{23}$-*g*-PTEGMA$_{13}$ SAs are >80% after 48 h incubation, indicating the biocompatibility of our hyperbranched systems. With drug loading, both of them possess good inhibition of HeLa cells proliferation. Both of them have considerable IC$_{50}$ values according to the literature,[19,53−55] and the data are shown in Figure 12b. The inhibition of HeLa cells proliferation by DOX-loaded SAs HB-PCL$_{26}$-*b*-PTEGMA$_{12}$-DOX seems better than that of the HB-PCL$_{23}$-*g*-PTEGMA$_{13}$-DOX analogue (Figure 12b) even though the HB-PCL$_{23}$-*g*-PTEGMA$_{13}$-DOX exhibits higher cell uptake than HB-PCL$_{26}$-*b*-PTEGMA$_{12}$-DOX (Figure S24). This difference can probably be attributed to their different release rates. Moreover, by comparison of the results for drug-loaded hyperbranched assemblies with and without disulfide linkages (Figure S25), the existing disulfide linkages seem to provide a better inhibition efficiency of HeLa cells proliferation due to their redox responsiveness.[56] As it is widely accepted that the intracellular glutathione (GSH) level in cancer cells is higher than that in normal cells,[57,58] the results imply that the high GSH level in cancer cells may accelerate the destabilization of SAs with disulfide linkages.[45,58,59]

■ **CONCLUSION**

The effects of block composition and distribution on the degradation behavior of hyperbranched amphiphiles and the drug release kinetics were investigated by using a set of Hyperblock HB-PCL-*b*-PTEGMA and Hypergraft HB-PCL-*g*-PTEGMA copolymers with controlled parameters as model samples. The degradation study monitored by GPC and DLS

Scheme 3. Schematic Illustration of Hydrophobic Domain and Loaded Drug for (a) Hyperblock HB-PCL-*b*-PTEGMA and (b) Hypergraft HB-PCL-*g*-PTEGMA
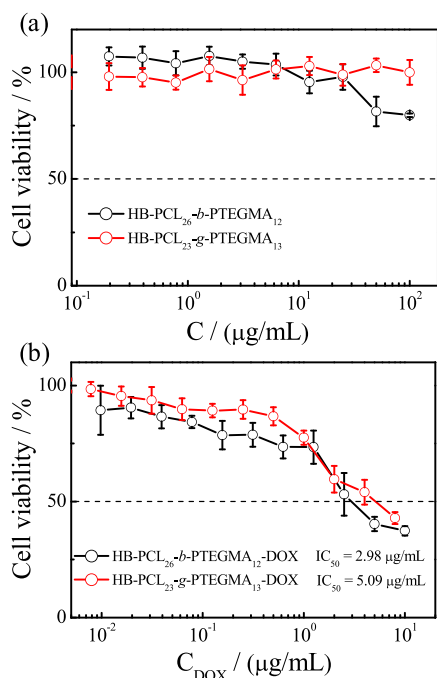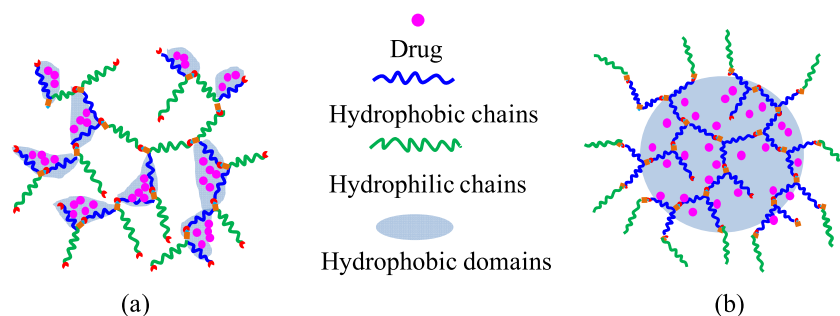

(a)   (b)

Figure 12. In vitro cytotoxicity of Hela cells against (a) bare polymeric SAs of Hyperblock HB-PCL$_{26}$-*b*-PTEGMA$_{12}$ and Hypergraft HB-PCL$_{23}$-*g*-PTEGMA$_{13}$ and (b) DOX loaded SAs of Hyperblock HB-PCL$_{26}$-*b*-PTEGMA$_{12}$ and Hypergraft HB-PCL$_{23}$-*g*-PTEGMA$_{13}$ for 48 h.

clearly demonstrated that both of the model systems can be degraded by using DTT as the reducing agent. In addition, the degradation results of self-assembly amphiphiles (SAs) reveal that the factors of block distribution and composition play different roles for the regulation of degradation behavior of long-subchain hyperbranched SAs; namely, the degradation process is mainly affected by the chain architecture and the structure of resultant SAs, while for a given chain architecture, the degradation rate can be regulated by systematically varying the block composition. In addition, control experiments indicated the neglected effect of embedded disulfide linkages on the crystallization of PCL block and the degradation process. It is well-known that the stability and release kinetics for a given drug-loaded SAs system will be influenced by multifactors, such as the degradation behavior of polymer assembly itself, the concentration of trigger molecules, the hydrophilic/hydrophobic balance of drug molecules, and the special interaction between drug molecules and polymer framework. It is not an easy task to realize the controlled

release of target drug molecules by optimizing all these factors simultaneously. This study shows that even for hyperbranched systems with a similar hydrophobic/hydrophilic block composition, the minor change of block sequence and distribution can lead to totally different degradation behavior. Thus, a careful examination of the polymer structure–degradation property relation is the prerequisite for further comprehensive adjustment of multifactors to realize the controlled degradation of polymer assembly and release of target drug.

■ ASSOCIATED CONTENT

Ⓢ Supporting Information

The Supporting Information is available free of charge on the ACS Publications website at DOI: 10.1021/acs.macro-mol.8b01784.

Molar mass information from GPC and ^{1}H NMR data; schematic illustration of the synthesis of reference samples; standard curve of DOX in DMSO; fluorescence intensity ratio I_{338}/I_{335}; ^{1}H NMR spectra; IR spectra; GPC curves; hydrodynamic radius distribution $f(R_h)$; TEM micrograph; DSC curves; TGA curves; time dependence of average hydrodynamic radius; drug release kinetics; cytotoxicity; flow cytometric analyses (PDF)

■ AUTHOR INFORMATION

Corresponding Authors
*E-mail xdye@ustc.edu.cn.
*E-mail llw@mail.ustc.edu.cn.
ORCID Ⓘ
Lianwei Li: 0000-0002-1996-6046
Xiaodong Ye: 0000-0003-2143-1726
Notes
The authors declare no competing financial interest.

■ ACKNOWLEDGMENTS

■ REFERENCES

(1) Wang, Y.; Grayson, S. M. Approaches for the Preparation of Non-Linear Amphiphilic Polymers and Their Applications to Drug Delivery. *Adv. Drug Delivery Rev.* **2012**, *64*, 852–865.

(2) Yates, C. R.; Hayes, W. Synthesis and Applications of Hyperbranched Polymers. *Eur. Polym. J.* **2004**, *40*, 1257−1281.

(3) Konkolewicz, D.; Gray-Weale, A.; Perrier, S. Hyperbranched Polymers by Thiol-Yne Chemistry: from Small Molecules to Functional Polymers. *J. Am. Chem. Soc.* **2009**, *131*, 18075−18077.

(4) Kurniasih, I. N.; Keilitz, J.; Haag, R. Dendritic Nanocarriers Based on Hyperbranched Polymers. *Chem. Soc. Rev.* **2015**, *44*, 4145−4164.

(5) Kim, Y. H.; Webster, O. W. Hyperbranched Polyphenylenes. *Macromolecules* **1992**, *25*, 5561−5572.

(6) Yang, G.; Jikei, M.; Kakimoto, M. A. Successful Thermal Self-Polycondensation of AB$_2$ Monomer to Form Hyperbranched Aromatic Polyamide. *Macromolecules* **1998**, *31*, 5964−5966.

(7) Stiriba, S. E.; Kautz, H.; Frey, H. Hyperbranched Molecular Nanocapsules: Comparison of the Hyperbranched Architecture with the Perfect Linear Analogue. *J. Am. Chem. Soc.* **2002**, *124*, 9698−9699.

(8) Prabaharan, M.; Grailer, J. J.; Pilla, S.; Steeber, D. A.; Gong, S. Q. Folate-Conjugated Amphiphilic Hyperbranched block Copolymers Based on Boltorn® H40, Poly(L-lactide) and Poly(ethylene glycol) for Tumor-Targeted Drug Delivery. *Biomaterials* **2009**, *30*, 3009−3019.

(9) Liu, J. Y.; Pang, Y.; Huang, W.; Zhu, X. Y.; Zhou, Y. F.; Yan, D. Y. Self-Assembly of Phospholipid-Analogous Hyperbranched Polymers Nanomicelles for Drug Delivery. *Biomaterials* **2010**, *31*, 1334−1341.

(10) Follmann, H. D.; Oliveira, O. N.; Lazarin-Bidóia, D.; Nakamura, C. V.; Huang, X.; Asefa, T.; Silva, R. Multifunctional Hybrid Aerogels: Hyperbranched Polymer-Trapped Mesoporous Silica Nanoparticles for Sustained and Prolonged Drug Release. *Nanoscale* **2018**, *10*, 1704−1715.

(11) Sideratou, Z.; Agathokleous, M.; Theodossiou, T. A.; Tsiourvas, D. Functionalized Hyperbranched Polyethylenimines as Thermosensitive Drug Delivery Nanocarriers with Controlled Transition Temperatures. *Biomacromolecules* **2018**, *19*, 315−328.

(12) Wais, U.; Chennamaneni, L. R.; Thoniyot, P.; Zhang, H.; Jackson, A. W. Main-Chain Degradable Star Polymers Composed of pH-Responsive Hyperbranched Cores and Thermoresponsive Polyethylene Glycol-Based Coronas. *Polym. Chem.* **2018**, *9*, 4824−4839.

(13) Hu, X. L.; Zhai, S. D.; Liu, G. H.; Xing, D.; Liang, H. J.; Liu, S. Y. Concurrent Drug Unplugging and Permeabilization of Polyprodrug-Gated Crosslinked Vesicles for Cancer Combination Chemotherapy. *Adv. Mater.* **2018**, *30*, 1706307.

(14) Cao, Y. W.; He, J. L.; Liu, J.; Zhang, M. Z.; Ni, P. H. Folate-Conjugated Polyphosphoester with Reversible Cross-Linkage and Reduction Sensitivity for Drug Delivery. *ACS Appl. Mater. Interfaces* **2018**, *10*, 7811−7820.

(15) Ju, P. F.; Hu, J.; Li, F.; Cao, Y. W.; Li, L.; Shi, D. J.; Hao, Y.; Zhang, M. Z.; He, J. L.; Ni, P. H. A biodegradable Polyphosphoester-Functionalized Poly (disulfide) Nanocarrier for Reduction-Triggered Intracellular Drug Delivery. *J. Mater. Chem. B* **2018**, *6*, 7263−7273.

(16) Ikladious, N. E.; Mansour, S. H.; Asaad, J. N.; Emira, H. S.; Hilt, M. Synthesis and Evaluation of New Hyperbranched Aalkyds for Coatings. *Prog. Org. Coat.* **2015**, *89*, 252−259.

(17) Grimsdale, A. C.; Leok Chan, K.; Martin, R. E.; Jokisz, P. G.; Holmes, A. B. Synthesis of Light-Emitting Conjugated Polymers for Applications in Electroluminescent Devices. *Chem. Rev.* **2009**, *109*, 897−1091.

(18) Wang, J.; Mei, J.; Zhao, E. G.; Song, Z. G.; Qin, A. J.; Sun, J. Z.; Tang, B. Z. Ethynyl-Capped Hyperbranched Conjugated Polytriazole: Click Polymerization, Clickable Modification, and Aggregation-Enhanced Emission. *Macromolecules* **2012**, *45*, 7692−7703.

(19) Liu, J. Y.; Huang, W.; Pang, Y.; Huang, P.; Zhu, X. Y.; Zhou, Y. F.; Yan, D. Y. Molecular Self-assembly of a Homopolymer: an Alternative to Fabricate Drug-delivery Platforms for Cancer Therapy. *Angew. Chem.* **2011**, *123*, 9328−9332.

(20) Lee, S.; Saito, K.; Lee, H. R.; Lee, M. J.; Shibasaki, Y.; Oishi, Y.; Kim, B. S. Hyperbranched Double Hydrophilic Block Copolymer Micelles of Poly (ethylene oxide) and Polyglycerol for pH-Responsive Drug Delivery. *Biomacromolecules* **2012**, *13*, 1190−1196.

(21) Hu, X. L.; Liu, G. H.; Li, Y.; Wang, X. R.; Liu, S. Y. Cell-Penetrating Hyperbranched Polyprodrug Amphiphiles for Synergistic Reductive Milieu-Triggered Drug Release and Enhanced Magnetic Resonance Signals. *J. Am. Chem. Soc.* **2015**, *137*, 362−368.

(22) Liu, J. Y.; Huang, W.; Pang, Y.; Zhu, X. Y.; Zhou, Y. F.; Yan, D. Y. Self-Assembled Micelles from an Amphiphilic Hyperbranched Copolymer with Polyphosphate Arms for Drug Delivery. *Langmuir* **2010**, *26*, 10585−10592.

(23) Liu, J. Y.; Pang, Y.; Huang, W.; Huang, X. Y.; Meng, L. L.; Zhu, X. Y.; Zhou, Y. F.; Yan, D. Y. Bioreducible Micelles Self-Assembled from Amphiphilic Hyperbranched Multiarm Copolymer for Glutathione-Mediated Intracellular Drug Delivery. *Biomacromolecules* **2011**, *12*, 1567−1577.

(24) Zhuang, Y. Y.; Deng, H. P.; Su, Y.; He, L.; Wang, R. B.; Tong, G. S.; He, D. N.; Zhu, X. Y. Aptamer-Functionalized and Backbone Redox-Responsive Hyperbranched Polymer for Targeted Drug Delivery in Cancer Therapy. *Biomacromolecules* **2016**, *17*, 2050−2062.

(25) Fréchet, J. M. J.; Henmi, M.; Gitsov, I.; Aoshima, S.; Leduc, M. R.; Grubbs, R. B. Self-Condensing Vinyl Polymerization: An Approach to Dendritic. *Science* **1995**, *269*, 1080−1083.

(26) Hawker, C. J.; Frechet, J. M. J.; Grubbs, R. B.; Dao, J. Preparation of Hyperbranched and Star Polymers by a "Living", Self-Condensing Free Radical Polymerization. *J. Am. Chem. Soc.* **1995**, *117*, 10763−10764.

(27) Peleshanko, S.; Gunawidjaja, R.; Petrash, S.; Tsukruk, V. V. Synthesis and Interfacial Behavior of Amphiphilic Hyperbranched Polymers: Poly(ethylene oxide)-Polystyrene Hyperbranches. *Macromolecules* **2006**, *39*, 4756−4766.

(28) Liu, M. J.; Vladimirov, N.; Fréchet, J. M. J. A New Approach to Hyperbranched Polymers by Ring-Opening Polymerization of an AB Monomer: 4-(2-Hydroxyethyl)-ε-caprolactone. *Macromolecules* **1999**, *32*, 6881−6884.

(29) Magnusson, H.; Malmström, E.; Hult, A. Synthesis of Hyperbranched Aliphatic Polyethers via Cationic Ring-Opening Polymerization of 3-ethyl-3-(hydroxymethyl)oxetane. *Macromol. Rapid Commun.* **1999**, *20*, 453−457.

(30) Hutchings, L. R.; Roberts-Bleming, S. J. DendriMacs. Well-Defined Dendritically Branched Polymers Synthesized by an Iterative Convergent Strategy Involving the Coupling Reaction of AB$_2$ Macromonomers. *Macromolecules* **2006**, *39*, 2144−2152.

(31) He, C.; Li, L. W.; He, W. D.; Jiang, W. X.; Wu, C. Click" Long Seesaw-Type A ∼ ∼B∼∼ A Chains Together into Huge Defect-Free Hyperbranched Polymer Chains with Uniform Subchains. *Macromolecules* **2011**, *44*, 6233−6236.

(32) Li, L. W.; He, C.; He, W. D.; Wu, C. Formation Kinetics and Scaling of "Defect-Free" Hyperbranched Polystyrene Chains with Uniform Subchains Prepared from Seesaw-Type Macromonomers. *Macromolecules* **2011**, *44*, 8195−8206.

(33) Li, L. W.; Zhou, J. F.; Wu, C. Intrachain Folding and Interchain Association of Hyperbranched Chains with Long Uniform Subchains Made of Amphiphilic Diblock Copolymers. *Macromolecules* **2012**, *45*, 9391−9399.

(34) Li, L. W.; He, C.; He, W. D.; Wu, C. How Does a Hyperbranched Chain Pass through a Nanopore? *Macromolecules* **2012**, *45*, 7583−7589.

(35) Yang, J. X.; Li, L. W.; Jing, Z. Y.; Ye, X. D.; Wu, C. Construction and Properties of Hyperbranched Block Copolymer with Independently Adjustable Heterosubchains. *Macromolecules* **2014**, *47*, 8437−8445.

(36) Li, L. W.; Wang, X.; Yang, J. X.; Ye, X. D.; Wu, C. Degradation Kinetics of Model Hyperbranched Chains with Uniform Subchains and Controlled Locations of Cleavable Disulfide Linkages. *Macromolecules* **2014**, *47*, 650−658.

(37) Ryu, J. H.; Roy, R.; Ventura, J.; Thayumanavan, S. Redox-Sensitive Disassembly of Amphiphilic Copolymer Based Micelles. *Langmuir* **2010**, *26*, 7086−7092.

(38) Liu, S. Q.; Wiradharma, N.; Gao, S. J.; Tong, Y. W.; Yang, Y. Y. Bio-Functional Micelles Self-Assembled from a Folate-Conjugated Block Copolymer for Targeted Intracellular Delivery of Anticancer Drugs. *Biomaterials* **2007**, *28*, 1423−1433.

(39) Cuong, N. V.; Li, Y. L.; Hsieh, M. F. Targeted Delivery of Doxorubicin to Human Breast Cancers by Folate-Decorated Star-Shaped PEG-PCL Micelle. *J. Mater. Chem.* **2012**, *22*, 1006−1020.

(40) Sun, Y.; Yan, X. L.; Yuan, T. M.; Liang, J.; Fan, Y. J.; Gu, Z. W.; Zhang, X. D. Disassemblable Micelles Based on Reduction-Degradable Amphiphilic Graft Copolymers for Intracellular Delivery of Doxorubicin. *Biomaterials* **2010**, *31*, 7124−7131.

(41) Nojima, S.; Fujimoto, M.; Kakihira, H.; Sasaki, S. Effects of Copolymer Composition on the Crystallization and Morphology of Poly (ε-caprolactone)-*block*-Polystyrene. *Polym. J.* **1998**, *30*, 968−975.

(42) Shi, G. Y.; Yang, L. P.; Pan, C. Y. Synthesis and Characterization of Well-Defined Polystyrene and Poly (ε-caprolactone) Hetero Eight-Shaped Copolymers. *J. Polym. Sci., Part A: Polym. Chem.* **2008**, *46*, 6496−6508.

(43) Lee, R. S.; Li, H. R.; Yang, J. M.; Tsai, F. Y. Synthesis of Biodegradable Poly (trans-4-hydroxy-N-benzyloxycarbonyl-l-proline)-Block-Poly (ε-caprolactone) Copolymers and Micellar Characterizations. *Polymer* **2005**, *46*, 10718−10726.

(44) Riva, R.; Schmeits, S.; Jérôme, C.; Jérôme, R.; Lecomte, P. Combination of Ring-Opening Polymerization and "Click Chemistry": toward Functionalization and Grafting of Poly (ε-caprolactone). *Macromolecules* **2007**, *40*, 796−803.

(45) Oh, J. K.; Siegwart, D. J.; Matyjaszewski, K. Synthesis and Biodegradation of Nanogels as Delivery Carriers for Carbohydrate Drugs. *Biomacromolecules* **2007**, *8*, 3326−3331.

(46) Pinnel, P.; Mendez-Nelson, A.; Noh, S. M.; Nam, J. H.; Oh, J. K. Rapid and Tunable Reductive Degradation of Disulfide-Labeled Polyesters. *Macromol. Chem. Phys.* **2012**, *213*, 678−685.

(47) Li, L. W.; Lu, Y. Y.; An, L. J.; Wu, C. Experimental and Theoretical Studies of Scaling of Sizes and Intrinsic Viscosity of Hyperbranched Chains in Good Solvents. *J. Chem. Phys.* **2013**, *138*, 114908.

(48) Yasin, M.; Tighe, B. J. Polymers for Biodegradable Medical Devices: VIII. Hydroxybutyrate-hydroxyvalerate Copolymers: Physical and Degradative Properties of Blends with Polycaprolactone. *Biomaterials* **1992**, *13*, 9−16.

(49) Bogdanov, B.; Vidts, A.; Schacht, E.; Berghmans, H. Isothermal Crystallization of Poly (ε-caprolactone-ethylene glycol) Block Copolymers. *Macromolecules* **1999**, *32*, 726−731.

(50) You, J. H.; Choi, S. W.; Kim, J. H.; Kwak, Y. T. Synthesis and Microphase Separation of Biodegradable Poly (ε-caprolactone)-Poly (ethylene glycol)-Poly (ε-caprolactone) Multiblock Copolymer Films. *Macromol. Res.* **2008**, *16*, 609−613.

(51) Li, Y. L.; Zhu, L.; Liu, Z. Z.; Cheng, R.; Meng, F. H.; Cui, J. H.; Ji, S. J.; Zhong, Z. Y. Reversibly Stabilized Multifunctional Dextran Nanoparticles Efficiently Deliver Doxorubicin into the Nuclei of Cancer Cells. *Angew. Chem., Int. Ed.* **2009**, *48*, 9914−9918.

(52) Su, W.; Luo, X. H.; Wang, H. F.; Li, L.; Feng, J.; Zhang, X. Z.; Zhuo, R. X. Hyperbranched Polycarbonate-Based Multimolecular Micelle with Enhanced Stability and Loading Efficiency. *Macromol. Rapid Commun.* **2011**, *32*, 390−396.

(53) Wang, W.; Sun, H. L.; Meng, F. H.; Ma, S. B.; Liu, H. Y.; Zhong, Z. Y. Precise Control of Intracellular Drug Release and Anti-Tumor Activity of Biodegradable Micellar Drugs via Reduction-Sensitive Shell-Shedding. *Soft Matter* **2012**, *8*, 3949−3956.

(54) Shi, C. L.; Guo, X.; Qu, Q. Q.; Tang, Z. M.; Wang, Y.; Zhou, S. B. Actively Targeted Delivery of Anticancer Drug to Tumor Cells by Redox-Responsive Star-Shaped Micelles. *Biomaterials* **2014**, *35*, 8711−8722.

(55) Liu, J. Y.; Pang, Y.; Huang, W.; Zhu, Z. Y.; Zhu, X. Y.; Zhou, Y. F.; Yan, D. Y. Redox-Responsive Polyphosphate Nanosized Assemblies: a Smart Drug Delivery Platform for Cancer Therapy. *Biomacromolecules* **2011**, *12*, 2407−2415.

(56) Sun, H. L.; Guo, B. N.; Li, X. Q.; Cheng, R.; Meng, F. H.; Liu, H. Y.; Zhong, Z. Y. Shell-Sheddable Micelles Based on Dextran-SS-Poly (ε-caprolactone) Diblock Copolymer for Efficient Intracellular Release of Doxorubicin. *Biomacromolecules* **2010**, *11*, 848−854.

(57) Russo, A.; DeGraff, W.; Friedman, N.; Mitchell, J. B. Selective Modulation of Glutathione Levels in Human Normal versus Tumor Cells and Subsequent Differential Response to Chemotherapy Drugs. *Cancer Res.* **1986**, *46*, 2845−2848.

(58) Ko, N. R.; Oh, J. K. Glutathione-Triggered Disassembly of Dual Disulfide Located Degradable Nanocarriers of Polylactide-Based Block Copolymers for Rapid Drug Release. *Biomacromolecules* **2014**, *15*, 3180−3189.

(59) Sun, H. L.; Guo, B. N.; Cheng, R.; Meng, F. H.; Liu, H. Y.; Zhong, Z. Y. Biodegradable Micelles with Sheddable Poly (ethylene glycol) Shells for Triggered Intracellular Release of Doxorubicin. *Biomaterials* **2009**, *30*, 6358−6366.
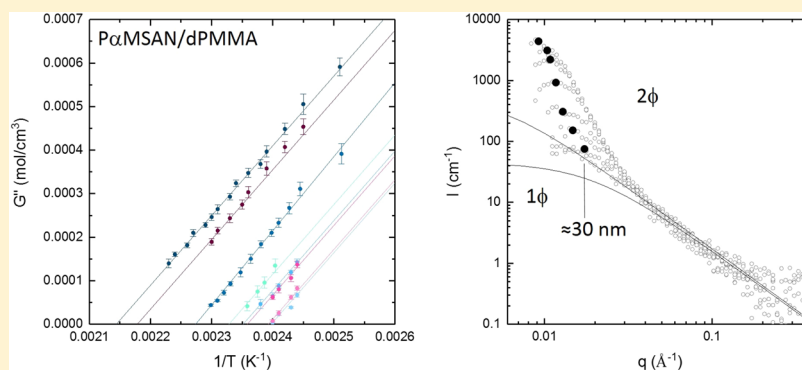
Small Angle Neutron Scattering Study of the Thermodynamics of Highly Interacting PαMSAN/dPMMA Blends

Yutaka Aoki,[†] Haoyu Wang,[†] William Sharratt,[†] Robert M. Dalgliesh,[‡] Julia S. Higgins,[†] and João T. Cabral*,[†]

[†]Department of Chemical Engineering, Imperial College London, London SW7 2AZ, United Kingdom
[‡]Rutherford Appleton Laboratory, ISIS, Harwell, Didcot OX11 0QX, United Kingdom

S *Supporting Information*

ABSTRACT: Poly(methyl methacrylate) (PMMA) and poly(α-methylstyrene-*co*-acrylonitrile) (PαMSAN) form partially miscible blends with lower critical solution temperature (LCST) behavior. We revisit this system using small angle neutron scattering (SANS), examining the effect of molecular weight (M_w) of deuterated PMMA (dPMMA), blend composition (ϕ), and temperature (T) in the homogeneous region. All data are well-described by the Random Phase Approximation (RPA) theory, enabling us to determine thermodynamic and structural parameters, including the correlation length ξ, G'' (the second derivative of the free energy of mixing with respect to composition), and the statistical segment length a of each component. Phase boundaries are computed by extrapolation of G'' with temperature, to yield the spinodal, and inspection of Kratky plots to yield the binodal. For PαMSAN, a is determined to be 10.1 ± 0.4 Å. Unsurprisingly, this system deviates strongly from Flory–Huggins expectations, exhibiting a minimal M_w dependence of the phase boundaries and ϕ dependence of effective interaction parameter ($\tilde{\chi}$). Comparison of G'' with values for other blend systems places PαMSAN/dPMMA in a class of highly interacting blends, expected from Cahn–Hilliard theory to yield small initial phase sizes upon spinodal demixing. This is confirmed experimentally, with an illustrative temperature jump resulting in an initial phase size of $\simeq 30$ nm.

INTRODUCTION

Demixing of polymer blends provides an attractive route to the fabrication of nano- and microporous materials, with applications ranging from membranes for separations,[1] biological scaffolds, to organic photovoltaics.[2] The characteristic length scale of the demixed structure is generally key to material performance and set by, often complex, phase separation pathways. These include rapid solvent evaporation or phase inversion and kinetic arrest, starting from polymer–polymer–solvent, ternary (or multicomponent) mixtures, or via the processing of immiscible blends. Thermal (or pressure) induced demixing of partially miscible binary systems yields a potentially simple and controlled approach to inducing well-defined polymeric structures. From an equilibrium state, in the homogeneous region of the phase diagram, a temperature jump (T-jump) into the two-phase, unstable, region can yield well-defined bicontinuous materials with prescribed dimensions. This method is in principle less costly and synthetically

demanding than block copolymer assembly, and provided that the structure of interest can be rapidly quenched (e.g., by cooling below glass transition temperature), it is exceptionally versatile.

Predictions of spinodal structures via polymer blend demixing strategy rely on the Cahn–Hilliard–Cook (C–H) theory,[3−5] adapted to the context of polymer blends.[6] In short, at early times, the dominant wavenumber of the isotropic, periodic structure can be analytically estimated to be $q^* = \sqrt{-G''/4k}$, where $G'' \equiv \frac{\partial^2 \Delta G_m}{\partial \phi^2}$ is the second derivative of the free energy of mixing ΔG_m with respect to composition (ϕ), and k is the so-called "square gradient term". The driving force for demixing is subsumed in G'' while the energetic

Table 1. Polymer Sample Characteristics: PαMSAN Comprises 30% AN and 70% α-MSt[a]

	$\langle M \rangle_w$ [kg/mol]	$\langle M \rangle_w / \langle M \rangle_n$	m [g/mol]	T_g [°C]	b [fm]	a [Å]	$\langle R_g \rangle_w$ [nm]
PαMSAN	122	2.6	98.66	118 ± 1	21.12	10.1 ± 0.4	14.5
dPMMA40k	39.5	1.1	108.1	115 ± 1	98.20	6.9	5.4
dPMMA99k	99.1	1.1	108.1	122 ± 1	98.20	6.9	8.5
dPMMA130k-P	131	2.0	108.1	117 ± 1	98.20	6.9	9.8

[a]Segment lengths a for PαMSAN were obtained from this work and for dPMMA from the previous literature.[19,20] Chain dimensions R_g were computed according to $\langle R_g \rangle_w = (\langle N \rangle_w a^2 / 6)^{0.5}$ from the tabulated values. Parameter b is the coherent neutron scattering length, and m is the mass of each repeat unit.

penalty associated with composition gradients due to fluctuations is quantified by k.

The predictive ability of polymer blend thermodynamic theory to compute phase behavior and G'' is currently limited, given the well-known shortcomings of Flory−Huggins (FH) lattice theory, and the relative complexity of models such as polymer reference interaction site model (PRISM),[7] lattice cluster theory (LCT),[8] locally correlated lattice (LCL)[9,10] theory, and others. These incorporate some structural information about the polymeric constituents, chain conformation statistics, and interaction potentials in some form. For instance, LCT explicitly considers monomer architecture, chain stiffness, energetic asymmetries, and nonrandom mixing, while LCL is an equation of state approach able to accommodate volume changes upon mixing as well as nonrandom mixing.[9,10] Accurate blend data and rigorous theoretical comparisons with experimental data are still needed to advance this field.

Small angle neutron scattering (SANS) is a powerful means to investigate the thermodynamics of polymer blends and directly determine G'' and k in the one-phase region. The former can be simply related to forward scattering intensity $S(q \rightarrow 0)$, and both can be obtained from de Gennes Random Phase Approximation (RPA) theory.[11] Over the past four decades, various authors have experimentally investigated the early stages of spinodal decomposition (e.g., refs 12−14) with a combination of light, neutron, and X-ray scattering as well as various microscopies. A few studies have examined the validity of the C−H prediction of the initial length scale of polymer blend demixing, which we have recently reviewed and found to be remarkably accurate,[15] despite neglecting hydrodynamic interactions, nonlinear terms to the diffusion equation, and limitations of the mean field assumption for blends (involved in estimating G'' and particularly k). Extrapolation of $G''(T)$ with temperature from the one-phase region, which is positive, to the two-phase region, across the spinodal line, where it becomes negative, appears thus an effective approach to selecting G'' and, in turn, $q*$ to predictively design bicontinuous structures.

In this paper, we investigate a model blend of poly(α-methylstyrene-co-acrylonitrile) (PαMSAN) with (deuterated) poly(methyl methacrylate) (dPMMA) by SANS. PαMSAN/dPMMA forms a lower critical solution temperature (LCST) mixture, whose glass transition temperature ($T_g \approx 120$ °C) is near the critical temperature (≈140 °C), thus enabling precise time-resolved SANS experiments. This system has been previously reported by Higgins et al.[16] and identified as a highly interacting blend,[15] in terms of the magnitude of G'' for a modest, accessible quench depth ΔT within the spinodal line. In simple terms, refined below, this blend exhibits a large β (or slope) in the descriptive relation $G'' = \alpha + \beta/T$. We employ a M_w series of atactic dPMMA ($M_w = 40−130$ kg/mol) with

different polydispersity (PDI) and investigate an unprecedented composition window, encompassing critical and off-critical mixtures, and temperature range. We systematically map G'' (and effective $\tilde{\chi}$), correlation length ξ of concentration fluctuations, and segment lengths a across all conditions in the homogeneous region. We finally provide an illustration of a T-jump experiment into the unstable region to induce a bicontinuous nanoscale morphology of prescribed dimensions.

■ EXPERIMENTAL SECTION

Polymer Mixtures. Poly(α-methylstyrene-co-acrylonitrile) (PαMSAN) was kindly donated by BASF (Luran KR2556) with 30% AN and 70% α-MSt.[17] Deuterated poly(methyl methacrylate) was purchased from Polymer Source Inc. (40k and 99k) and synthesized in our laboratory (130k-P). The 40k and 99k were prepared by living group transfer polymerization and living anionic polymerization, respectively, while the 130k-P was obtained by radical polymerization,[18] and all specimens are largely atactic. Key characteristics of the polymers used are summarized in Table 1, and the monomer chemical structures are given in Figure 1. Glass transition temper-
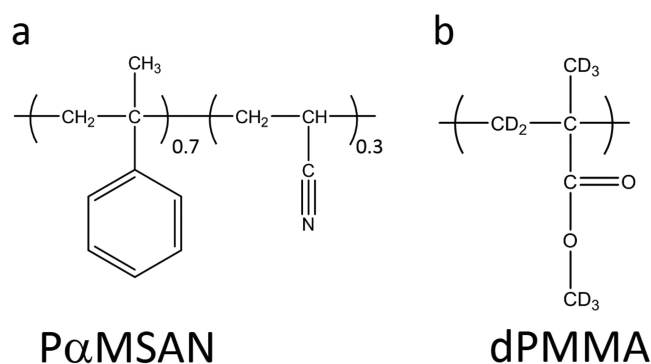

Figure 1. Monomer repeat units of poly(α-methylstyrene-co-acrylonitrile) and (deuterated) poly(methyl methacrylate).

atures of the pure components were determined by differential scanning calorimetry (DSC) using a TA Instruments Q2000 instrument, at 10 °C/min heating rate, and computed with the midpoint method.

Blends of PαMSAN and dPMMA, at various M_w and compositions, were prepared by solution casting. All blend compositions were prepared by mass and then converted into volumetric ratio of PαMSAN using the pure component densities ($\rho_{PαMSAN} = 1.07(5)$ g/cm³ and $\rho_{dPMMA} = 1.27(5)$ g/cm³). The polymers were first dissolved in tetrahydrofuran (THF, purity ≥99.7% unstabilized HPLC grade, VWR) at a concentration of 8% w/v and stirred at room temperature for 48 h. The solution was drop cast onto glass coverslips (19 mm in diameter, VWR), and the solvent was allowed to evaporate at ambient conditions for 1 week. The resulting films (of approximately 100 μm thickness) were then carefully peeled off, stacked together, and gently pressed (Specac hydraulic press, 4 ton) at room temperature with an aluminum mold to obtain approximately 1 mm thick films. The films were then placed under vacuum (20 mbar) for 4 weeks, while
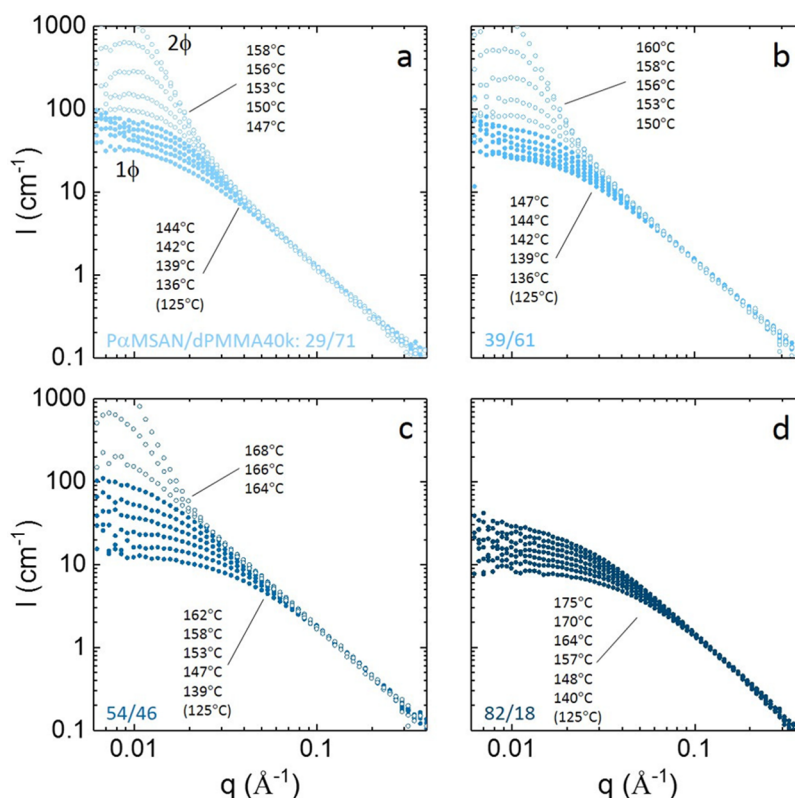
Figure 2. Coherent SANS scattering data for PαMSAN/dPMMA40k blends of four different compositions: (a) 29/71, (b) 29/61, (c) 54/46, and (d) 82/18 v/v. Samples were heated in a stepwise manner for time intervals ranging from 120 min (near T_g) to 3 min, near the phase boundary. The filled symbols indicate data in the one-phase region of the phase diagram, while open symbols indicate demixed, out-of-equilibrium conditions. Data at 125 °C correspond to specimens annealed for 36 h prior to the experiment.

gradually increasing the temperature up to 110 °C, which is just below the blend T_g. Prior to the SANS experiment, the temperature was increased to 125 °C for 36 h and then cooled down to room temperature under (20 mbar) vacuum to prevent absorption of moisture. The 1 mm thick films were then wrapped in a thin aluminum foil (22 μm) sachet to be mounted onto the temperature-controlled cell to acquire SANS data in the one-phase region. Selected thin (100 μm) samples were also prepared for T-jump experiments into the two-phase region.

Cloud point curves of the various PαMSAN/dPMMA were measured using a temperature-controlled stage (Linkam Scientific THMS600) upon heating at 0.5 °C/min until the sample became cloudy and bluish. These optical cloud point measurements were consistently higher (by approximately 20−30 °C) that those determined by SANS, which is not unexpected given the smaller length scales probed by the latter.

Small Angle Neutron Scattering. SANS experiments were performed at ISIS (UK) Larmor, with a polychromatic $\lambda = 0.9–13.3$ Å unpolarized incident beam and $D_{s-d} = 4.1$ m, yielding a fixed momentum transfer range of approximately $0.003 < q < 0.7$ Å^{-1}. For these measurements, a larger incident divergence was used to increase flux at the cost of a truncated momentum transfer range of $0.006 < q < 0.6$ Å^{-1}. The elastic scattering vector is $q = \frac{4\pi}{\lambda} \sin\left(\frac{\theta}{2}\right) \approx \frac{2\pi}{\lambda}$, for small scattering angles θ.

A custom-made T-jump cell was employed for both equilibrium, one-phase, and demixing experiments. The cell consists of two brass ovens with quartz windows and a motorized sample carrier, which rapidly (<1 s) transports the sample between the two ovens. The setup has been described elsewhere.[21,22] For equilibrium, one-phase experiments, the sample was loaded at 125 °C (the final oven temperature) into the measurement oven, and the temperature was systematically increased, in a stepwise fashion, in steps of 8 °C (close to T_g) to 2 °C, near the phase boundary. Acquisition times varied

from 120 min (close to T_g) and 3 min, near demixing, for PαMSAN/dPMMA blends, and 30 min for backgrounds and empty cells. All data were acquired in "event mode/list" enabling the measurement time-resolution to be selected *a posteriori*. This feature is particularly useful to ensure that data are at equilibrium (e.g., near T_g and phase boundaries), and data sets can be truncated accordingly. Sample thicknesses were determined using a digital micrometer, and self-consistency with neutron transmission was confirmed.

Scattering data were reduced and calibrated, and the contribution from the empty cell was subtracted, using Mantid.[23] The coherent scattering function was then obtained after subtraction of the appropriate volume fraction of the calibrated spectra of the hydrogenous component PαMSAN (provided in the Supporting Information, Figure S1).

■ RESULTS AND DISCUSSION

Optical Cloud Point Boundaries. Prior to SANS measurements, the binary temperature−composition phase diagram of PαMSAN/dPMMA blends was estimated optically at a relatively low heating rate of 0.5 °C/min. For blends containing dPMMA40k, we obtained cloud points of 172, 170, 177, and 198 °C for compositions PαMSAN/dPMMA 29/71, 39/61, 54/46, and 82/18, respectively. Similar results were obtained for 99k and 130k-P, as shown in the Supporting Information, Figure S2. The optical cloud points thus indicate an asymmetric LCST phase diagram, with critical point (≈30/70−40/60 v/v), in broad agreement with previous work.[16,24] The faint, bluish, cloudy appearance of the specimens suggests demixed structures at a fine (≲1 μm) length scale. We take these as upper estimates of the phase boundaries of the system, given the relative proximity to T_g (≈120 °C), the limited spatial resolution of optical microscopy, and the finite heating

rate employed in the measurement. Offsets of up to 30 °C between optical microscopy data upon demixing and one-phase SANS were found, and these were consistent with the coarsening data obtained by time-resolved SANS following temperature jumps and ramps into the two-phase region. We have therefore relied on isothermal SANS in the one phase to establish the phase boundaries, as described below.

Inspection of SANS Coherent Scattering Data. The coherent scattering data for PαMSAN/dPMMA40k blends of various compositions, as a function of temperature, are shown in Figure 2. Filled symbols correspond to data identified in the one-phase region, with no structural peak, while open symbols indicate samples which have crossed into the two-phase region. Particular attention was given to lower temperature SANS measurements, as equilibration of concentration fluctuations is expected to be slow near T_g. The first measurements were carried out at 125 °C, following a 36 h annealing (*ex situ*); inspection of the data revealed that all samples, regardless of M_w and ϕ, had not reached equilibrium, as gauged by extrapolation from higher temperature measurements. These were therefore disregarded and are shown in brackets in Figure 2. Isothermal SANS measurements were carried out by increasing temperature in a stepwise manner, and waiting for the temperature of the experimental cell to be reached (within ±0.2 °C, typically 300 s); we then ensured that the scattering intensity profile no longer evolved in time (made possible by the "event" mode operation of LARMOR). Typically, these additional "wait" time intervals (attributed to the equilibration of concentration fluctuations) ranged from 600 to 100 s, at approximately $T_g + 20$ °C to $T_g + 50$ °C. These data were then analyzed within the RPA and Ornstein−Zernike (OZ) formalisms, detailed below.

Upon increasing temperature further, a number of blend compositions (PαMSAN/dPMMA40k 29/71, 39/61, 54/46 v/v) exhibited a structural peak associated with demixing. From these observations, the phase boundaries can be estimated as approximately 144 °C at 29/71, 147 °C at 39/61, 162 °C at 54/46, and above 175 °C at 82/18. The highest temperature investigated was 175 °C to prevent sample degradation. Near the critical point, the experimentally available temperature window within the one-phase region is thus very narrow, $T_c - T_g \simeq 20-25$ °C.

RPA and OZ Analysis. The absolute coherent scattering intensity (in $[cm^{-1}]$ units) from a binary polymer blend in the one-phase region is given by

$$I(q) = N_A \left(\frac{b_1}{v_1} - \frac{b_2}{v_2} \right)^2 S(q) \tag{1}$$

where b_1 and b_2 are the coherent scattering lengths of monomer units 1 and 2, v_1 and v_2 are their monomer molar volumes of the units, and N_A is the Avogadro number. The forward scattering intensity (at a given temperature) has particular significance, as $G''(T) \equiv 1/S(q = 0, T)$ providing a direct estimation of the second derivative of the free energy of mixing. We refer to component 1 as PαMSAN, and 2 as dPMMA, for which $b_1 = 21.12$ fm, $v_1 = 91.77$ cm³/mol, $b_2 = 98.20$ fm, and $v_1 = 84.79$ cm³/mol, yielding a contrast prefactor $N_A(b_1/v_1 - b_2/v_2)^2 = 5.19 \times 10^{-3}$ cm⁻⁴ mol. The structure factor of the homogeneous binary blend is written according to de Gennes' Random Phase Approximation (RPA),[11] as

$$\frac{1}{S(q)} = \frac{1}{S_1(q)} + \frac{1}{S_2(q)} - 2\frac{\tilde{\chi}_{12}}{v_0} \tag{2}$$

where $S_i(q)$ $[cm^3/mol]$ is the structure factor of each component, and χ_{12} is monomer−monomer interaction parameter. Considering component polydispersity, $S_i(q)$ can be written as[25]

$$S_i(q) = \phi_i v_i \langle N_i \rangle_n \langle g_D(R_{gi}^2 q^2) \rangle_w \tag{3}$$

where ϕ_i is volume fraction, v_0 is a reference molar volume taken as $v_0 \equiv \sqrt{v_1 v_2}$, and $\langle N_i \rangle_n$ is the number-average degree of polymerization of component i. Term $\langle g_D(R_{gi}^2 q^2) \rangle_w$ is the weight-average form factor of a Gaussian chain, computed from the Debye function, assuming a Schultz−Zimm polydispersity distribution:[22,25−28]

$$\langle g_D(x) \rangle_w = \frac{2}{\langle x \rangle^2} \left[\left(\frac{h}{h+x} \right)^h - 1 + x \right] \tag{4}$$

where $x \equiv q^2 \langle R_g^2 \rangle_n$, $h = (M_w/M_n - 1)^{-1}$, and the n-average radius of gyration for a Gaussian coil $\langle R_g^2 \rangle_n^{1/2} \equiv \langle N \rangle_n a^2/6$, where a is the statistical segment length. For polydisperse components, care is needed in the estimation of a from SANS, which directly measures z-average dimensions and w-average masses (or N). From eq 4, in the limit $q \to 0$, then $\langle g_D(x \to 0) \rangle_w \to 1$, and eq 2 becomes

$$\frac{1}{S(0)} = \frac{1}{\phi_1 v_1 \langle N_1 \rangle_w} + \frac{1}{\phi_2 v_2 \langle N_2 \rangle_w} - 2\frac{\chi_{12}}{v_0} \tag{5}$$

recalling the Flory−Huggins χ value at the spinodal

$$\chi_s = \frac{v_0}{2} \left(\frac{1}{\phi_1 v_1 \langle N_1 \rangle_w} + \frac{1}{\phi_2 v_2 \langle N_2 \rangle_w} \right) \tag{6}$$

yields from eq 5 that

$$(G'' \equiv) \frac{1}{S(0)} = \frac{2}{v_0}(\chi_s - \tilde{\chi}_{12}) \tag{7}$$

where $\tilde{\chi}_{12}$ is an *effective* interaction parameter, measured by SANS, which can be related to the common Flory−Huggins parameter χ_{12} by

$$\tilde{\chi}_{12} = -\frac{1}{2} \frac{\partial^2 [\phi(1-\phi)\chi_{12}]}{\partial \phi^2} \tag{8}$$

where $\tilde{\chi}_{12} \equiv \chi_{12}$ for composition-independent interactions. At low angle scattering angles ($qR_g < 1$) the simpler OZ provides a good approximation to the data, where

$$S(q) = \frac{S(0)}{1 + \xi^2 q^2} \tag{9}$$

and thus

$$\frac{1}{S(q)} = \frac{1}{S(0)} + Aq^2 \tag{10}$$

with

$$A = \frac{1}{3} \left(\frac{\langle R_{g1}^2 \rangle_z}{\phi_1 v_1 \langle N_1 \rangle_w} + \frac{\langle R_{g2}^2 \rangle_z}{\phi_2 v_2 \langle N_2 \rangle_w} \right) = \frac{1}{18} \left(\frac{(h_1+2)a_1^2}{(h_1+1)\phi_1 v_1} + \frac{(h_2+2)a_2^2}{(h_2+1)\phi_2 v_2} \right) \tag{11}$$
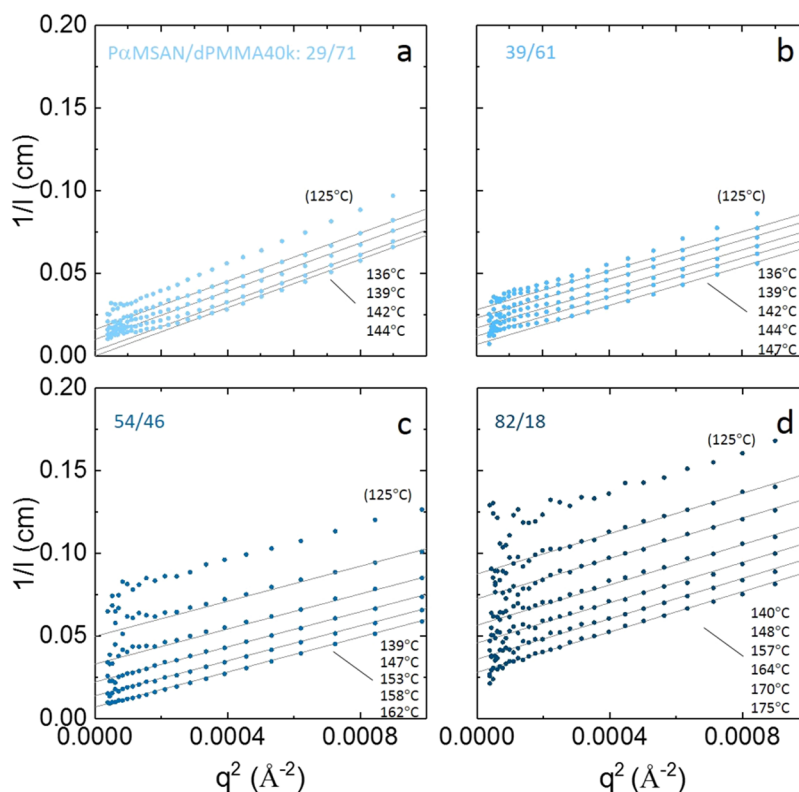
Figure 3. Ornstein−Zernike fits to the low q coherent SANS scattering data, in the one-phase region, for PαMSAN/dPMMA40k at the v/v compositions indicated. The specimens annealed at 125 °C for 36 h have not reached equilibrium, as seen by the curved $1/I$ vs q^2, and by an offset of the expected trend of $1/I(0)$ with temperature (Supporting Information, Figure S3). From these OZ fits, the forward scattering intensity $S(0)$ and the correlation lengths ξ are extracted as a function of temperature and composition.

where the last equality is obtained by noting that $\langle R_g^2 \rangle_z = \frac{h+2}{h+1} \langle R_g^2 \rangle_w$ for finite (Schultz−Zimm) polydispersity. The correlation length is thus obtained as $\xi \equiv \sqrt{AS(0)}$ where, as previously noted, $1/S(0) \equiv G''$. An important self-consistency test for the RPA involves the link between the correlation length ξ^2 and the forward scattering intensity, $S(0)$ expressed by $\xi^2 = AS(0)$ which was ensured for all data (provided in the Supporting Information, Figure S3).

All SANS profiles of homogeneous blends, at temperatures above T_g, were analyzed with RPA and OZ formalisms, and the latter is illustrated for the PαMSAN/dPMMA40k blend series in Figure 3. As expected, the inverse scattering intensity varies linearly with q^2, and the slope of the curves yields thus A in eq 10, from which chain dimensions and segment lengths can be computed according to eq 11. The intercept of this plot is directly proportional to G'' allowing a direct estimation of the spinodal temperature by extrapolation to zero, as described below. Slope A is expected to be constant with temperature, according to eq 11. At 125 °C we observe this slope deviates from those measured at higher temperatures, away from T_g, and that the dependence with (inverse) temperature departs from the linearity expected from $G'' = \alpha + T/\beta$. These measurements in near proximity to T_g are thus taken to be out of equilibrium and not analyzed further. Further, data at the lowest q values ($q^2 < 0.0001$ Å^{-2}) in Figure 3a,b somewhat deviate from linearity, interpreted as due to the slow equilibration of long wavelength concentration fluctuations near T_g.

While extrapolation of G'' to zero provides robust estimates of the spinodal line, locating the binodal is generally more

involved. We therefore use deviations from RPA and the emergence of a shoulder or peak at temperatures sufficiently above T_g as evidence of demixing. Kratky plots (Iq^2 vs q) provide a useful means of identifying small departures from q^{-2} scaling. We therefore estimate spinodal lines from $G''(T)$ and the binodal lines from Kratky deviations, ensuring self-consistency with the spinodal.

Kratky Asymptote. The structure factor of one-phase blends at high wavenumber ($qR_g \gg 1$) is given by

$$S(q)q^2 \approx 12 \Big/ \left(\frac{a_1^2}{\phi_1 v_1} + \frac{a_2^2}{\phi_2 v_2} \right) \tag{12}$$

reaching therefore a constant value at high q in a so-called "Kratkty plot" (Iq^2 vs q). Illustrative plots for PαMSAN/dPMMA40k blends are shown in Figure 4. We observe a peak emerging at 142 °C for PαMSAN/dPMMA40k:29/71, 147 °C for PαMSAN/dPMMA40k:39/61, and 164 °C for PαMSAN/dPMMA40k:54/46, while no peak is observed for PαMSAN/dPMMA40k:82/18. Scattering profiles deviating for the lines computed from RPA theory are thus concluded to be in the two-phase region, shown by open symbols in the graph. Demixing temperatures determined using Kratky plots are lower than those estimated from the coherent scattering shown in Figure 2 for PαMSAN/dPMMA40k:29/71 and 39/61, and are therefore taken as more accurate, given the higher sensitivity of this method.

The high q asymptote of Iq^2 depends thus only on the polymer component volume fraction ϕ_i, the monomer molar volume v_i, and the segment length a_i of each polymer. Significantly, it does not depend on the polymer molecular
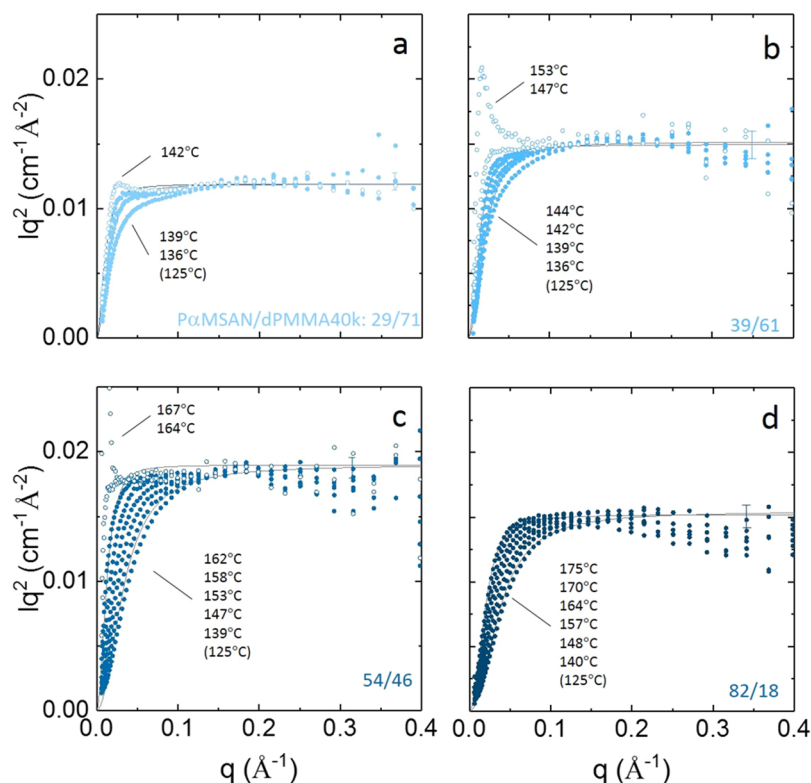
Figure 4. Kratky plots of PαMSAN/dPMMA40k at the four different compositions indicated. The filled symbols indicate one-phase region of the phase diagram. The lines correspond to RPA theory at the temperatures of lowest and highest of equilibrium with adjusting segment length of PαMSAN and fixing well-known segment length of dPMMA. The specimens annealed at 125 °C for 36 h have not reached equilibrium. The Kratky plateau depends on composition ratio and the segment length of each component. The open symbols indicate the two-phase region of the phase diagram, the lowest temperature of which gives our best indication of the binodal temperature.

weight distribution, nor temperature, unlike the preceding equations for lower angle scattering, since it measures the *local* polymer conformation. Since ϕ_i and v_i are known, a_i can be determined directly from the Kratky asymptote. To increase the accuracy of the measurement of a of PαMSAN, we fix the well-known PMMA segment length to $a(\text{PMMA}) = 6.9$ Å.[19,20,29] Further, we collectively fit $a(\text{PαMSAN})$ as a function of composition ϕ_i for the various $M_w(\text{dPMMA})$ in Figure 5, where the lines represent confidence intervals. The upper and lower lines indicate $a(\text{PαMSAN}) = 10.5$ and 9.7 Å, respectively. We therefore obtain $a(\text{PαMSAN}) = 10.1 \pm 0.4$ Å which is, to our knowledge, the first determination of the segment length for this polymer.

Correlation Length and Second Derivative of Free Energy. RPA is found to fit well all one-phase scattering data as shown in Figure 6. During data analysis, the higher q region is preferentially fitted, given the lower angle deviations discussed above and related to slow thermal equilibration of long wavelength concentration fluctuations near T_g, which is evidently faster at higher q, as described by C–H theory in the homogeneous region.[30,31]

Figure 7 provides RPA parameters G'', $\tilde{\chi}/v_0$, as well as OZ correlation length squared ξ^{-2}, as a function of temperature. Since $\xi^{-2} = (AS(0))^{-1} = G''/A$, both G'' and ξ^{-2} show an inverse temperature dependence $(1/T)$, whose extrapolation to zero yields the spinodal temperature (for a given ϕ and M_w). The effective interaction parameter $\tilde{\chi}_{12}/v_0$ is then computed from eq 7 assuming a χ_s/v_0 calculated from Flory–Huggins theory, eq 6, indicated as a horizontal line in the figure. (RPA
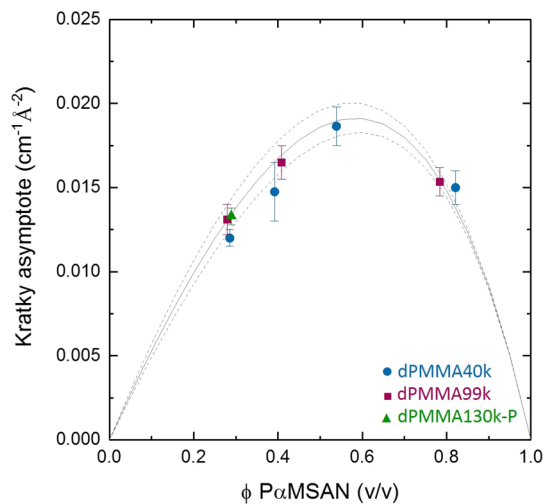

Figure 5. Kratky asymptote as a function of composition of PαMSAN for blends with three dPMMA $M_w = 40\text{k}$, 99k, and 130k-P, where P indicates a polydisperse sample $(M_w/M_n \approx 2.0)$. The symbols correspond to the experimentally measured Kratky asymptote values and associated uncertainty. The lines correspond to data fits to eq 12 for the segment length of PαMSAN, encompassing the largest and smallest values compatible with the data, yielding $a_{\text{PαMSAN}} = 10.1 \pm 0.4$ Å (while fixing $a_{\text{dPMMA}} = 6.9$ Å).

parameters for other M_w's are provided in the Supporting Information, Figures S4 and S5.)

The second derivative of the free energy G'' as a function of inverse temperature $1/T$ for all compositions ϕ and dPMMA
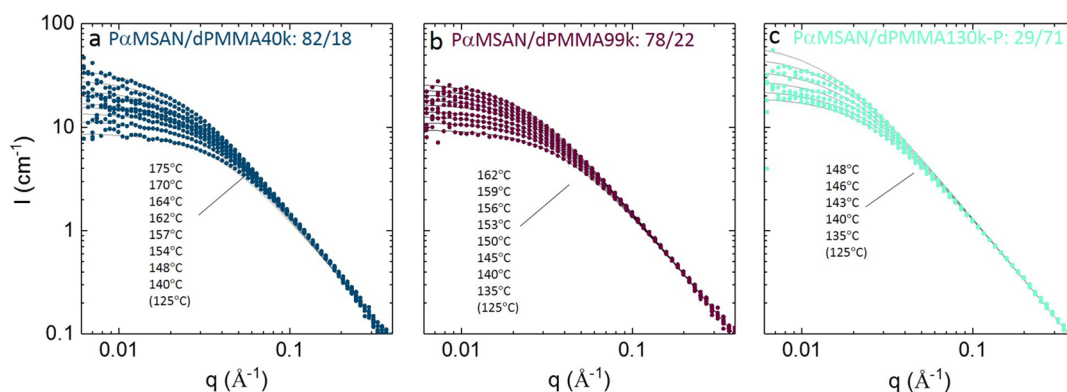
Figure 6. Coherent scattering intensity and RPA fits for one-phase data of blends of PαMSAN/dPMMA of different M_w: (a) PαMSAN/dPMMA40k:82/18, (b) PαMSAN/dPMMA99k:78/22, and (c) PαMSAN/dPMMA130k-P:29/71, measured as a function of temperature.
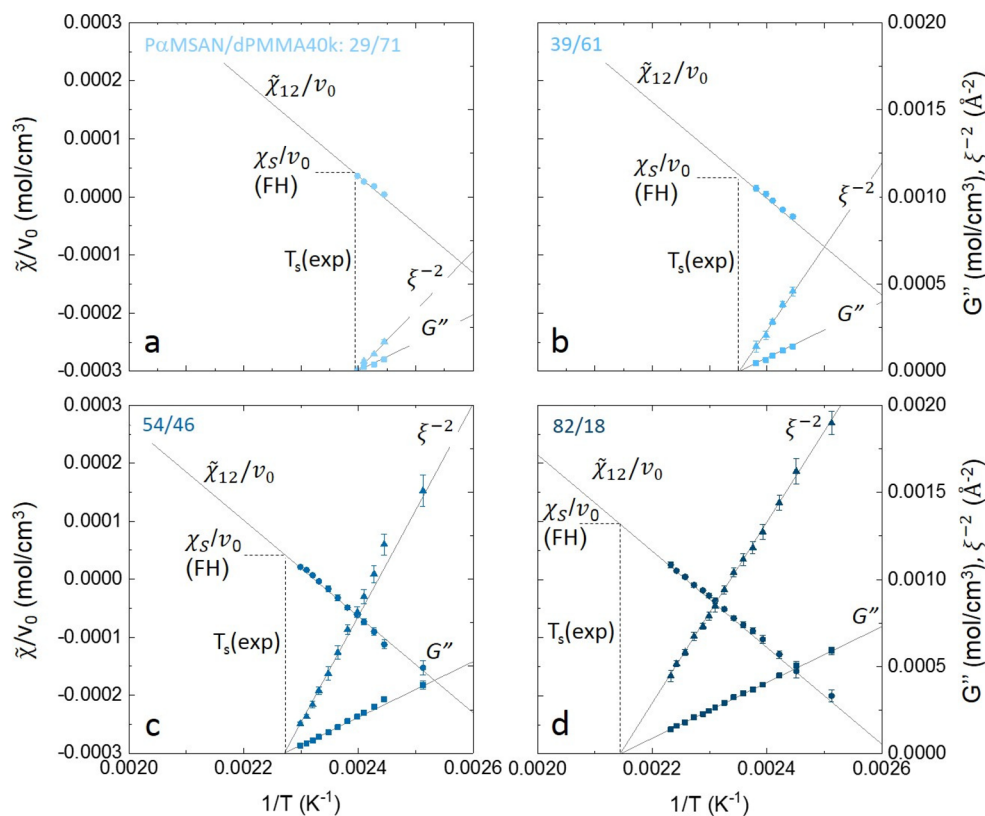

Figure 7. Correlation length ξ^{-2}, second derivative of free energy of mixing G'', and effective interaction parameter $\tilde{\chi}_{12}/v_0$ as a function of inverse temperature $1/T$ for PαMSAN/dPMMA40k with four compositions. Vertical dash lines indicates the experimentally measured spinodal temperature.

M_w is given in Figure 8. All data fit linearly, following $G'' = \alpha + \beta/T$ with the same slope $\alpha = 1.60$ remarkably well. The intercept α is tabulated in Table 2. The large α (and thus steep temperature dependence of blend component interactions) established this as a "highly interacting" blend, as detailed below. (A comparison with the previous measurement of G'' as a function of $1/T$ is provided in the Supporting Information, Figure S6).[16]

The phase diagram for all blends investigated is shown in Figure 9, in broad agreement with that reported by Higgins et al.[16] The solid lines indicate the spinodal, while the dashed line estimates the binodal. We find that both the shape and location of the phase diagram vary little with M_w, and the critical point for this blend is estimated at ≤30% v/v PαMSAN. The phase

boundaries remain asymmetrical regardless of varying M_w. The spinodal curve of PαMSAN/dPMMA40k is above that of PαMSAN/dPMMA99k, which is consistent with the M_w dependence expected for LCST polymer blends. However, boundaries for PαMSAN/dPMMA130k-P appear above the lower M_w data. We note that the polydispersity of dPMMA130k-P is 2.0, while those of dPMMA40k and dPMMA99k are 1.1 and 1.1, respectively, which should affect the coexistence curve but not the spinodal, as this is expected to be determined by M_w and not the full size distribution. Although we do not have a complete SANS phase diagram for this blend (and optical microscopy data shown to be inaccurate, Figure S2), this might be due to an increased asymmetry of the phase boundaries upon increasing M_w, or an
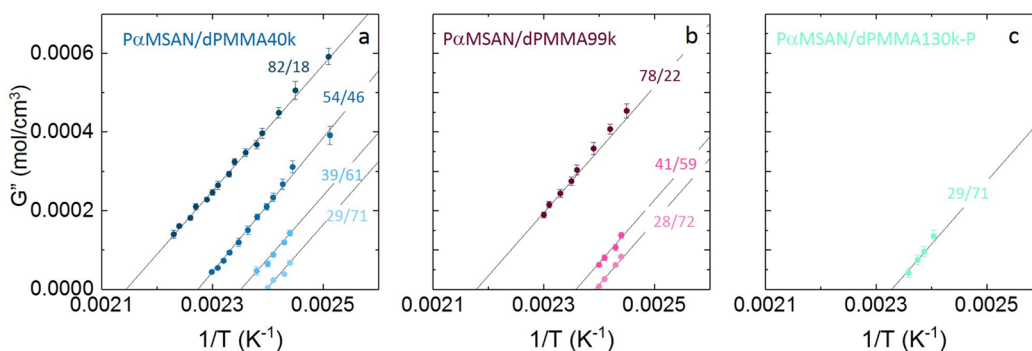
Figure 8. Second derivative of the free energy G'' as a function of inverse temperature $(1/T)$ for (a) PαMSAN/dPMMA40k, (b) PαMSAN/dPMMA99k, and (c) PαMSAN/dPMMA130k-P:29/71, at the compositions indicated in the one-phase region. The lines are simultaneous data fits to $G'' = \alpha + \beta/T$ with constant slope β.

Table 2. Tabulated Values[a] G'' and $\tilde{\chi}_{12}/v_0$ of PαMSAN/dPMMA Obtained by SANS in the One-Phase Region

dPMMA	$\phi_{\text{P}\alpha\text{MSAN}}$	$G'' = \alpha + 1.60/T$, α (mol/cm^3)	$\tilde{\chi}_{12}/v_0 = A - 0.83/T$, A (mol/cm^3)
40k	29/71	−0.003 84	0.002 03
	39/61	−0.003 76	0.001 99
	54/46	−0.003 63	0.001 93
	82/18	−0.003 43	0.001 87
99k	28/72	−0.003 83	0.002 01
	41/59	−0.003 77	0.001 98
	78/22	−0.003 49	0.001 84
130k-P	29/71	−0.003 73	0.001 95

[a]In the form $G'' = \alpha + \beta/T$, where $\beta = 1.60$ mol K/cm^3; and $\tilde{\chi}_{12}/v_0 = A + B/T$, where $= -0.83$ mol K/cm^3, respectively.
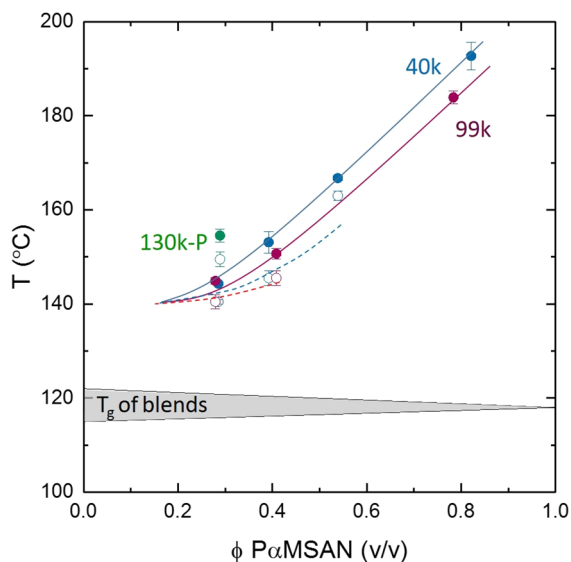

Figure 9. Phase diagram of PαMSAN/dPMMA40k, 99k, and 130k-P computed from SANS data. The filled symbols correspond to the spinodal temperature estimated by extrapolation of $G'' \rightarrow 0$ vs $1/T$. The open symbols indicate the estimated binodal temperatures from deviation of the one-phase Kratky plots. Lines serve as guide to the eye. We note that all blends, despite the varying M_w, exhibit nearly identical, asymmetric, phase boundaries. Blend T_g's were estimated from pure component data by the Fox equation:[32] $\frac{1}{T_{g,\text{blend}}} = \frac{\phi_{\text{P}\alpha\text{MSAN}}}{T_{g,\text{P}\alpha\text{MSAN}}} + \frac{\phi_{\text{dPMMA}}}{T_{g,\text{dPMMA}}}$, and indicated by the gray area.

apparent upward shift caused by slow equilibration of concentration fluctuations during SANS measurement. Our

main observation, however, is that all blends of different M_w studied exhibit remarkably similar phase boundaries. This is rather typical of systems where the contribution of combinatorial entropy is small compared to that of specific interaction. Evidently, these results deviate from Flory–Huggins predictions, which is unsurprising, in particular for highly interacting blends.

Effective Specific Interaction Parameter $\tilde{\chi}_{12}$. In the context of Flory–Huggins lattice theory,[33−35] the free energy of mixing is written as

$$\frac{\Delta G_m}{k_B T} = \frac{\phi \ln \phi}{v_1 N_1} + \frac{(1 - \phi)\ln(1 - \phi)}{v_2 N_2} + \frac{\phi(1 - \phi)}{v_0}\tilde{\chi}_{12}$$

$$(13)$$

which, in turn, implies that

$$G'' \equiv \frac{\partial^2\left(\frac{\Delta G_m}{k_B T}\right)}{\partial \phi^2} = \frac{1}{\phi_1 v_1 N_1} + \frac{1}{\phi_2 v_2 N_2} - 2\frac{\tilde{\chi}_{12}}{v_0}$$

$$(14)$$

which, combined with eq 7, allows for $\tilde{\chi}_{12}$ to be readily computed from experimental SANS data of $1/S(0) \equiv G''$. The temperature dependences of $\tilde{\chi}_{12}/v_0$ for PαMSAN/dPMMA40k blends of various compositions are shown in Figure 10a, and for various dPMMA M_w at a fixed composition $\approx$29/71 in Figure 10b. Following from Figure 8, all are well-described by a linear dependence $\tilde{\chi}/v_0 = A - 0.83/T$, whose intercept A varies with composition ϕ, and marginally with M_w as tabulated in Table 2. The composition dependence of $\tilde{\chi}/v_0$ is apparent given the different intercepts in Figure 10a. In Figure 10b, $\tilde{\chi}_{12}/v_0$ are found to differ slightly with M_w, at the same composition and temperature. We therefore parametrize $\tilde{\chi}_{12}/v_0$ in terms of composition ϕ as well as molecular weight M_w, as previously done by several authors.[36,37] We therefore write $\tilde{\chi}/v_0 = A' + B/T + C(\phi, M_w)$, where $A = A' + C(\phi, M_w)$. In the limit of $\phi \rightarrow 0$, A' can be estimated as $A' = 0.0021$. Figure 11 shows the composition dependence of $C(\phi, M_w)$ obtained as $C(\phi, M_w) \equiv A - A'$. Therefore, $\tilde{\chi}/v_0$ can be summarized as $\tilde{\chi}/v_0 = 0.0021 - 0.83/T - 0.000\,280\phi_{\text{P}\alpha\text{MSAN/dPMMA40k}}$, $\tilde{\chi}/v_0 = 0.0021 - 0.83/T - 0.000\,315\phi_{\text{P}\alpha\text{MSAN/dPMMA99k}}$, and $\tilde{\chi}/v_0 = 0.0021 - 0.83/T - 0.000\,483\phi_{\text{P}\alpha\text{MSAN/dPMMA130k-P}}$. Previously, Madbouly et al.[28] found $\chi = (0.525 - 22.5/T)/(1 - 0.4\phi_{\text{PMMA}})$ for blend of PαMSAN 97k (with 31% AN content) and PMMA 14k, by fitting phase boundaries obtained by light scattering to Flory–Huggins theory. This result is not in agreement with our SANS scattering data (as shown in the Supporting Information, Figure S7), likely due to the slow demixing kinetics and low
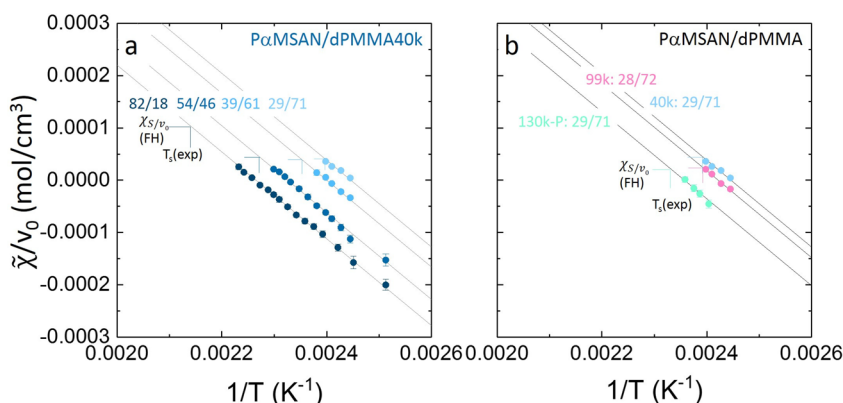
Figure 10. Effective $\tilde{\chi}_{12}/v_0$ as a function of $1/T$ for (a) PαMSAN/dPMMA40k with four compositions and (b) at constant composition, but three different $M_w = 40k$, 99k, and 130k-P. The filled symbols correspond to experimental data obtained from SANS and RPA analysis, and the lines are fits $\tilde{\chi}_{12}/v_0 = A + B/T$ in the one-phase region, with constant slope B. The vertical ticks mark the experimentally measured spinodal temperature, while the open circles show the χ_s calculated by Flory−Huggins theory.
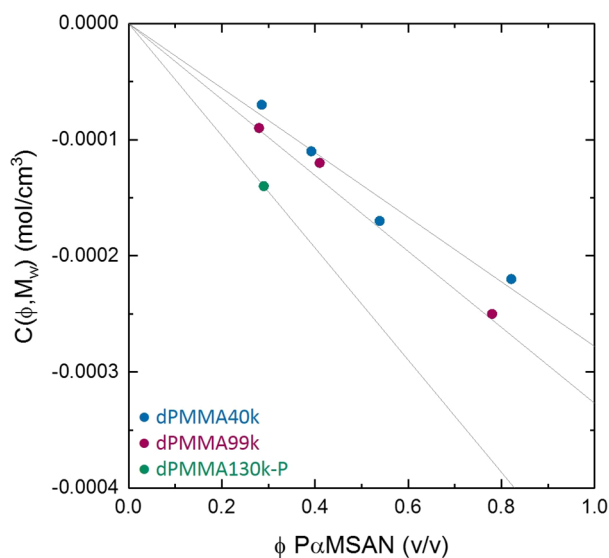

Figure 11. Parameter $C(\phi, M_w)$, subsuming the composition ϕ and M_w dependence of $\tilde{\chi}_{12}/v_0 = A + B/T + C(\phi, M_w)$ for all PαMSAN/dPMMA blends investigated, with $M_w = 40k$, 99k, and 130k-P, with common $A = 0.0021$ mol/cm^3 and $B = -0.83$ mol K/cm^3. The temperature was fixed at 139 °C (composition dependences of $\tilde{\chi}_{12}$ for various temperatures are provided in the Supporting Information, Figure S8).

refractive contrast for this blend, as also found in the context of our optical microscopy estimates. The significance and role of noncombinatorial entropy in the thermodynamics of this system will be discussed in a separate publication.

Magnitude of G'' and Spinodal Structure Design. A key prediction of the C−H theory of spinodal decomposition is that the initial length scale of the resulting bicontinuous structure has a dominant wavenumber given by

$$q^*(t=0) \simeq \sqrt{\frac{-G''}{4k}} \qquad (15)$$

yielding a length scale of $\Lambda \approx 2\pi/q^*$.[30] The generation of nanoscale spinodal structures by demixing induced by a T-jump thus requires a large G'' driving force for a relatively modest temperature quench depth. Large ΔT quenches are generally expected to lead to noninstantaneous processes, via a cascade of demixing steps.[38] To search for "highly interacting"

blends,[15] we focus on $G'' = \alpha + \beta/T$ noting that not only the magnitude of β is relevant but specifically the *value* of G'' at a given $\Delta T \equiv T - T_s$. For instance, manipulating α by tuning M_w (following Flory−Huggins expectations, eq 14) can also displace $T_s \equiv -\beta/\alpha$ and thus increase ΔT. However, the operational range for a temperature quench is bound by T_g and a ceiling (or depolymerization) temperature (for an LCST system), and is thus relatively small (symptomatic of the few partially miscible polymer pairs known). Further, in the framework of RPA and FH theories, the "square gradient" parameter k [Å^2 mol/cm^3] becomes

$$k = \frac{1}{6}\left(\frac{\langle R_{g1}^2 \rangle_z}{\phi_1 v_1 \langle N_1 \rangle_w} + \frac{\langle R_{g2}^2 \rangle_z}{\phi_2 v_2 \langle N_2 \rangle_w}\right) \qquad (16)$$

and thus $k \equiv A/2$ by comparison with eq 11. Parameter k thus relates to $\sim b_i^2/v_i$ as well as composition, typically varying from 0.05 to 0.2 Å^2 mol/cm^3 across typical systems.[15] We therefore compile previously reported data for G''/k as a function of ΔT for a range of representative systems, including the extensive measurements presented in the current work, in Figure 12. On the right axis, we show the corresponding Λ [nm] computed using the C−H prediction discussed above. The lines and shaded areas in red correspond to our current work with the PαMSAN/dPMMA system, establishing this as one of the most highly interacting systems reported in the literature. While these ($\sim$10 nm) length scales are commonly accessible via microphase separation of block copolymers (albeit requiring rather exacting synthesis and monodispersity), nanoscale demixing of polymer blends (whose component synthesis is generally larger scale, lower cost, and with lenient polydispersity) is perceived as challenging. Blends of solution chlorinated polyethylene (SCPE) with dPMMA might have even steeper G''/k slopes,[15,39,40] albeit within a narrow miscibility window, highly sensitive to the regularity and extent of chlorination of PE.[39] From a practical standpoint, the proximity of T_g and T_s in PαMSAN/dPMMA blends makes T-jump experiments feasible with the expectation of relatively slow structural coarsening. This contrasts with, for instance, the TMPC/dPS system also shown in Figure 12,[22] for which $T_s - T_g \geq 100$ °C, or polycarbonate/dPMMA for which T_s is likely below T_g (and thus preventing measurement of G'' in the one-phase region).[41]
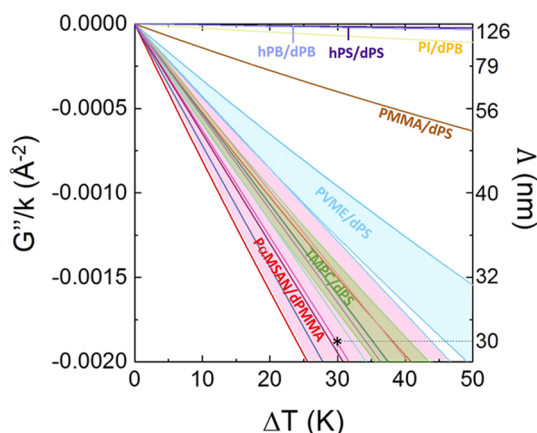
Figure 12. Second derivative of the free energy divided by square gradient term, G''/k, and initial spinodal length scale $\Lambda \equiv 2\pi/\sqrt{-G''/(4k)}$ as a function of quench depth ΔT. A range of LCST blends are included for comparison, alongside our current work on PαSAN/dPMMA: previous PαSAN 85k/dPMMA 112k:24/76 by Higgins et al.,[16] $k = 0.086$ Å^2 mol/cm^3; poly-(tetramethyl bisphenol A polycarbonate) 54k/deuterated polystyrene 225k (TMSC/dPS),[22] $k = 0.091-0.096$ Å^2 mol/cm^3; PVME 64.3-159k/dPS 195−783k,[42,43] $k = 0.073$ Å^2 mol/cm^3; polyisoprene 85k/1,4-polybutadiene 374k (PI/dPB),[44] $k = 0.071$ Å^2 mol/cm^3; as well as UCST systems of isotopic polybutadiene (hPB, $N = 3180$/dPB, $N = 3550$),[13] $k = 0.077$ Å^2 mol/cm^3; hPS/dPS, $k = 0.050$ Å^2 mol/cm^3; and PMMA/dPS, $k = 0.048$ Å^2 mol/cm^3; data computed by assuming $N = 1000$ for hPS/dPS, and $N = 50$ for PMMA/dPS.[45]

The asterisk in Figure 12 corresponds the expected outcome of a T-jump with $\Delta T \approx 30$ K, which we would thus expect to yield a structure with $\Lambda \simeq 30$ nm according to C−H theory. Such an experiment was carried out by time-resolved SANS for a blend of PαSAN/dPMMA99k:41/59, quenched from 140 to 180 °C, corresponding to $\Delta T \equiv T - T_s = 30$ K, since $T_s \approx 150$ °C for this system, as shown in Figure 13. At this

composition, $k = 0.151$ Å^2 mol/cm^3 taking into account component polydispersity, following eq 16.

The data shown in Figure 13a do not exhibit a time-invariant "early stage" regime as strictly expected for C−H theory (although unsurprising for such deep quench). The intensity peak is indicated by the black markers, and its location is plotted in Figure 13b as a function of time. The shift toward low q is expected for structural coarsening. The solid line is a guide to the eye facilitating the extrapolation to an initial q^* ($t \approx 0$), bounded by the uncertainty shown by the horizontal dashed lines (at $0.018 \leq q^* \leq 0.024$). The initial length scale is thus $\Lambda \equiv 2\pi/q^* \approx 30$ nm, in good agreement with our expectations above. Equivalently, analysis of q^* ($t \approx 0$) following a quench in the two-phase region data with C−H theory enables G'' to be *independently* estimated by rearranging eq 15 into $G'' = -4kq^{*2}$. We obtain $G'' \approx -2.7 \times 10^{-4}$ mol/cm^3, and plot this measurement (open symbol) alongside the one-phase, equilibrium data (closed symbols) in Figure 13c. The G'' results across the two sides of the stability boundary are in remarkable agreement and corroborate the validity of predictive structural design of spinodal structures based on this approach, and in particular approaching dimensions nearing R_g by employing deep quenches and highly interacting blend pairs.

CONCLUSIONS

We investigated the thermodynamics of PαSAN/dPMMA blends by small angle neutron scattering (SANS) as a function of temperature, composition, and molecular mass (of dPMMA). In total, 8 distinct blends and up to 15 temperatures (each) were measured. In the one-phase region, the forward scattering intensity $S(q \to 0)$ was measured to yield G'', the second derivative of the free energy of mixing with respect to composition, employing an Ornstein−Zernike analysis of $1/S(q)$ vs q^2. All $S(q)$ profiles in the one phase were well-described by RPA theory (eq 2), from which the polymer segment lengths a and effective $\tilde{\chi}/v_0$ interaction parameters (as well as G'') were computed. Combined with an ensemble
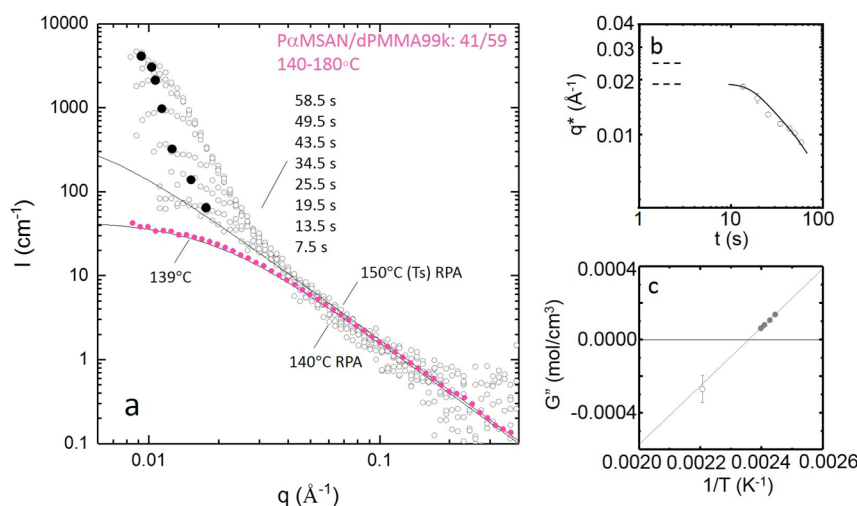

Figure 13. T-jump experiment from 140 to 180 °C for a blend of PαSAN/dPMMA99k:41/59. (a) The open symbols correspond to coherent SANS scattering data at various times after the jump, and the black filled symbols indicate the peak position q^* of the profile. The lines show the calculated RPA $S(q)$ at 140 °C, at the start of the T-jump, and that near the spinodal at 150 °C. (b) Time dependence of q^* during (rapid) coarsening with line as guide to the eye. Dashed lines show the range of q^* at $t \approx 0$ as guide to the eye. (c) Second derivative of the free energy G'' as a function of inverse temperature $1/T$: filled symbols correspond to one-phase data, and the open symbol shows G'' estimated from the T-jump data with $G'' = -4kq^{*2}$. The line has the same slope and intercept as that obtained in Figure 8b.

Kratky asymptote analysis of all data, the segment length for PαMSAN was determined, for the first time, to be 10.1 ± 0.4 Å. The phase diagram for all blends was estimated by systematic analysis of $S(q)$ data as a function of temperature: the spinodal line was obtained by extrapolation of G'' vs $1/T$ to zero, corresponding to the thermodynamic stability limit. The metastable zone was instead estimated from analysis of $S(q)$ and deviation for RPA approaching the phase boundaries. A structural peak in $S(q)$ clearly corresponded to temperatures above demixing; however detection approaching the binodal line was more complex due to the associated slow demixing kinetics, in particular close to T_g. In this instance, the emergence of a peak in the Kratky analysis Iq^2 vs q provided a useful indicator for deviations from the q^{-2} scaling law for miscible blends. Further, given the proximity between T_g and the binodal line, great care was taken to ensure that the samples were thermally equilibrated by analyzing time-resolved $S(q)$ data between temperature changes. Namely, the T_g(PαMSAN) = 118 °C and T_g(dPMMA) = 115–122 °C (with varying M_w), while the critical point ∼ 140 °C, which meant that measurements at the lower temperatures (up to 135 °C) could not reach equilibrium within experimental time scales and were thus not considered for analysis. All equilibrated one-phase measurements yielded self-consistent trends for G'' and correlation length ξ, following expectations from RPA.

The phase diagram obtained clearly does not follow Flory–Huggins expectations, in that the critical point and location of spinodal and binodal lines are broadly independent of M_w. The critical temperature is approximately 140 °C at a very asymmetric composition of ≃20% PαMSAN (v/v), even though the M_w of the polymer pairs is commensurate. We find that (model-free) G'' estimates follow $G'' = \alpha + \beta/T$ for all blend compositions, with a $\beta = 1.60$ mol K/cm³, meaning that the temperature dependence of G'' was the same for all blends. The intercept α evidently differed, from which the T_s was calculated, and found to deviate from Flory–Huggins expectations, which is unsurprising.

The effective Flory–Huggins parameter $\tilde{\chi}_{12}/v_0$ was then computed (eq 14) for all temperatures, composition ϕ, and M_w. Often, this parameter is expressed as $\tilde{\chi}_{12}/v_0 = A + B/T$. However, as found in several other polymer blends,[45] χ for this system is not only a function of T, but also ϕ- and M_w-dependent, and an expression $\tilde{\chi}_{12}/v_0 = A' + B/T + C(\phi, M_w)$ was thus adopted. A common reference volume $v_0 \equiv \sqrt{v_{P\alpha MSAN} v_{dPMMA}} \equiv 88.21$ cm³/mol was employed. Isolating the T-independent terms A' and $C(\phi, M_w)$ enabled a relatively simple parametrization, namely $A' = 0.0021$ mol/cm³ and $B = -0.83$ mol K/cm³. Parameter $C(\phi, M_w) = -3.15 \times 10^{-4}\phi$ [mol/cm³] for $M_w = 99$k and varies relatively little with M_w, viz. -2.8 to $4.8 \times 10^{-4}\phi$ across the M_w range. These (common) deviations from Flory–Huggins theory are generally attributed to additional noncombinatorial constraints to the free energy caused by monomer architecture, specific interactions, connectivity, compressibility, etc. These are generally subsumed into such complex parametrizations of $\tilde{\chi}_{12}$ for reasons of practicality. Physical insight can be gained by the detailed data interpretation with more comprehensive theories such as polymer reference interaction site model (PRISM),[7] or lattice cluster theory (LCT)[8] that explicitly incorporated structural information, chain conformation statistics, and interaction potentials in some form, or with equations of state, such as those of locally correlated lattice (LCL) theory which are for volume changes and nonrandom mixing.[9,10]

A survey of the magnitude of the interaction G'' and its temperature dependence indicates that PαMSAN/dPMMA is one of the most highly interacting blends known.[15,45] Interaction "strength" is defined here in terms of, not only the value of β in $G'' = A + \beta/T$, but actually the value of G'' at a specific $\Delta T \equiv |T - T_s|$. With these ideas in mind, we test the hypothesis that correspondingly small spinodal phase sizes can be achieved with rather modest T-jumps into the unstable region. We have recently reviewed the celebrated prediction of linearized C–H theory that the initial $q^* = \sqrt{-G''/4k}$ which we find to generally apply across a large range of systems. Selecting a representative blend and a rather deep quench (≈30 °C), specifically with a T-jump experiment from 140 to 180 °C and a blend of PαMSAN/dPMMA99k:41/59, we obtain the initial spinodal length scale $\Lambda \approx 30$ nm, in good agreement with linearized C–H theory.[3,4,6] The temperature dependence of G'' thus seems to continue across the two-phase region, at least away from the immediacy of the stability lines where deviations from mean-field theory are expected. Our T-jump experimental data fit well with G'' extracted from our single-phase region data, which is promising for further T-jump experiments. By analysis with linearized C–H theory or C–H–C theory, we would work to establish the limitation of these theories in prediction of the characteristic length scales. Overall, our results comprehensively map the thermodynamics of a highly interacting polymer blend, benchmarked against a range of other systems, and demonstrate the possibility of generating nanoscale bicontinuous structures by extrapolation from one-phase thermodynamic data uniquely accessible by SANS. These length scales are commensurate with those obtained by block copolymer microphase separation, albeit requiring kinetic arrest during demixing for their practical utilization, for instance, in photovoltaics, catalysis, membranes, or scaffolds. Further improvements in the predictive ability of blend thermodynamic and dynamic theory remain a significant requirement to the full exploitation of such otherwise facile approaches to generating nano- and microscale demixed polymeric materials.

■ ASSOCIATED CONTENT

Ⓢ Supporting Information

The Supporting Information is available free of charge on the ACS Publications website at DOI: 10.1021/acs.macromol.8b02431.

> Incoherent SANS background for PαMSAN, phase diagrams estimated by optical microscopy, RPA self-consistency test (ξ^2 vs $I(0)$), RPA data and parameters for dPMMA 99k and 130k-P blends, comparison with previous measurements of $G''(T)$, and composition dependence of $\tilde{\chi}_{12}/v_0$ (PDF)

■ AUTHOR INFORMATION

Corresponding Author

*E-mail: j.cabral@imperial.ac.uk. Phone: +44 207 594 5571.

ORCID Ⓘ

Haoyu Wang: 0000-0002-6563-8633

William Sharratt: 0000-0003-2148-8423

João T. Cabral: 0000-0002-2590-225X

Notes

The authors declare no competing financial interest.
Data presented in this paper are available on the Zenodo repository at 10.5281/zenodo.2537068.

■ REFERENCES

(1) Robeson, L. M. *Polymer Blends*; Carl Hanser Verlag GmbH Co. KG, 2007.

(2) Ma, W.; Yang, C.; Heeger, A. Spatial Fourier-Transform Analysis of the Morphology of Bulk Heterojunction Materials Used in Plastic Solar Cells. *Adv. Mater.* **2007**, *19*, 1387−1390.

(3) Cahn, J. W.; Hilliard, J. E. Free Energy of a Nonuniform System. I. Interfacial Free Energy. *J. Chem. Phys.* **1958**, *28*, 258−267.

(4) Cahn, J. W.; Hilliard, J. E. Free Energy of a Nonuniform System. III. Nucleation in a TwoComponent Incompressible Fluid. *J. Chem. Phys.* **1959**, *31*, 688−699.

(5) Cook, H. Brownian motion in spinodal decomposition. *Acta Metall.* **1970**, *18*, 297−306.

(6) Binder, K.; Frisch, H. L.; Jckle, J. Kinetics of phase separation in the presence of slowly relaxing structural variables. *J. Chem. Phys.* **1986**, *85*, 1505−1512.

(7) Schweizer, K. S.; Curro, J. G. In *Atomistic Modeling of Physical Properties*; Monnerie, L., Suter, U. W., Eds.; Springer Berlin Heidelberg: Berlin, Heidelberg, 1994; pp 319−377.

(8) Freed, K. F.; Dudowicz, J. In *Phase Behaviour of Polymer Blends*; Freed, K. F., Ed.; Springer Berlin Heidelberg: Berlin, Heidelberg, 2005; pp 63−126.

(9) Higgins, J. S.; Lipson, J. E. G.; White, R. P. A simple approach to polymer mixture miscibility. *Philos. Trans. R. Soc., A* **2010**, *368*, 1009−1025.

(10) White, R. P.; Lipson, J. E. G.; Higgins, J. S. New Correlations in Polymer Blend Miscibility. *Macromolecules* **2012**, *45*, 1076−1084.

(11) De Gennes, P.-G. *Scaling concepts in polymer physics*; Cornell university press, 1979.

(12) Sato, T.; Han, C. C. Dynamics of concentration fluctuation in a polymer blend on both sides of the phase boundary. *J. Chem. Phys.* **1988**, *88*, 2057−2065.

(13) Bates, F. S.; Wiltzius, P. Spinodal decomposition of a symmetric critical mixture of deuterated and protonated polymer. *J. Chem. Phys.* **1989**, *91*, 3258−3274.

(14) Hashimoto, T. Dynamics in spinodal decomposition of polymer mixtures. *Phase Transitions* **1988**, *12*, 47−119.

(15) Cabral, J. T.; Higgins, J. S. Spinodal nanostructures in polymer blends: On the validity of the Cahn-Hilliard length scale prediction. *Prog. Polym. Sci.* **2018**, *81*, 1−21.

(16) Higgins, J. S.; Fruitwala, H.; Tomlins, P. E. Correlation of phase-separation behavior in polymer blends with thermodynamic measurements in the one-phase region. *Macromolecules* **1989**, *22*, 3674−3681.

(17) Altstadt, V.; de Freitas, L. L.; Schubert, D. W. Rheological and mechanical properties of poly(α-Methylstyrene-co-Acrylonitrile)/poly(methylacrylate-co-methyl methacrylate) blends in miscibe and phase-separated regimes of various morphologies. *Pure Appl. Chem.* **2004**, *76*, 389−413.

(18) Phillips, A. L. Synthesis and Characterisation of novel polymers based on methyl methacrylate. Ph.D. thesis, Imperial College London, 1998.

(19) Wang, M.; Braun, H.-G.; Meyer, E. Crystalline structures in ultrathin poly(ethylene oxide)/poly(methyl methacrylate) blend films. *Polymer* **2003**, *44*, 5015−5021.

(20) Tanaka, K.; Takahara, A.; Kajiyama, T. Film Thickness Dependence of the Surface Structure of Immiscible Polystyrene/Poly(methyl methacrylate) Blends. *Macromolecules* **1996**, *29*, 3232−3239.

(21) Cabral, J. T. Polymer Blends: Equilibrium, Dynamics and Phase Separation. Ph.D. thesis, Imperial College London, 2002.

(22) Cabral, J. T.; Higgins, J. S. Small Angle Neutron Scattering from the Highly Interact- ing Polymer Mixture TMPC/PSd: No Evidence of Spatially Dependent Parameter. *Macromolecules* **2009**, *42*, 9528−9536.

(23) Arnold, O.; et al. MantidData analysis and visualization package for neutron scattering and SR experiments. *Nucl. Instrum. Methods Phys. Res., Sect. A* **2014**, *764*, 156−166.

(24) Madbouly, S. A.; Ougizawa, T. Spinodal Decomposition in Binary Blend of Poly(methyl methacrylate)/Poly(-methyl styrene-co-acrylonitrile): Analysis of Early and Late Stage Demixing. *Macromol. Chem. Phys.* **2004**, *205*, 979−986.

(25) Sakurai, S.; Hasegawa, H.; Hashimoto, T.; Hargis, I. G.; Aggarwal, S. L.; Han, C. C. Microstructure and isotopic labeling effects on the miscibility of polybutadiene blends studied by the small-angle neutron scattering technique. *Macromolecules* **1990**, *23*, 451−459.

(26) Zimm, B. H. Apparatus and Methods for Measurement and Interpretation of the Angular Variation of Light Scattering; Preliminary Results on Polystyrene Solutions. *J. Chem. Phys.* **1948**, *16*, 1099−1116.

(27) Sakurai, S.; Izumitani, T.; Hasegawa, H.; Hashimoto, T.; Han, C. C. Small-angle neutron scattering and light scattering study on the miscibility of poly(styrene-ran- butadiene)/polybutadiene blends. *Macromolecules* **1991**, *24*, 4844−4851.

(28) Sakurai, S.; Jinnai, H.; Hasegawa, H.; Hashimoto, T.; Han, C. C. Microstructure effects on the lower critical solution temperature phase behavior of deuterated polybutadiene and protonated polyisoprene blends studied by small-angle neutron scattering. *Macromolecules* **1991**, *24*, 4839−4843.

(29) Ballard, D.; Wignall, G.; Schelten, J. Measurement of molecular dimensions of polystyrene chains in the bulk polymer by low angle neutron diffraction. *Eur. Polym. J.* **1973**, *9*, 965−969.

(30) Cahn, J. W. Phase Separation by Spinodal Decomposition in Isotropic Systems. *J. Chem. Phys.* **1965**, *42*, 93−99.

(31) Strobl, G. R. Structure evolution during spinodal decomposition of polymer blends. *Macromolecules* **1985**, *18*, 558−563.

(32) Fox, T. G. Influence of Diluent and of Copolymer Composition on the Glass Temperature of a Polymer System. *Bull. Am. Phys. Soc.* **1956**, *1*, 123.

(33) Flory, P. J. Thermodynamics of High Polymer Solutions. *J. Chem. Phys.* **1941**, *9*, 660−660.

(34) Flory, P. J. Thermodynamics of High Polymer Solutions. *J. Chem. Phys.* **1942**, *10*, 51−61.

(35) Huggins, M. L. Solutions of Long Chain Compounds. *J. Chem. Phys.* **1941**, *9*, 440−440.

(36) Han, C. C.; Bauer, B. J.; Clark, J. C.; Muroga, Y.; Matsushita, Y.; Okada, M.; Tran-cong, Q.; Chang, T.; Sanchez, I. C. Temperature, composition and molecular-weight dependence of the binary interaction parameter of polystyrene/poly(vinyl methyl ether) blends. *Polymer* **1988**, *29*, 2002−2014.

(37) Londono, J. D.; Narten, A. H.; Wignall, G. D.; Honnell, K. G.; Hsieh, E. T.; John-son, T. W.; Bates, F. S. Composition Dependence of the Interaction Parameter in Iso- topic Polymer Blends. *Macromolecules* **1994**, *27*, 2864−2871.

(38) Carmesin, H. O.; Heermann, D. W.; Binder, K. Influence of a continuous quenching procedure on the initial stages of spinodal decomposition. *Z. Phys. B: Condens. Matter* **1986**, *65*, 89−102.

(39) Hill, R. G.; Tomlins, P. E.; Higgins, J. S. Preliminary study of the kinetics of phase separation in high molecular weight poly(methyl methacrylate)/solution-chlorinated polyethylene blends. *Macromolecules* **1985**, *18*, 2555−2560.

(40) Clark, J. N.; Fernandez, M. L.; Tomlins, P. E.; Higgins, J. S. Small-angle neutron scattering studies of phase equilibria in blends of deuterated poly(methyl methacrylate) with solution chlorinated polyethylene. *Macromolecules* **1993**, *26*, 5897−5907.

(41) Motowoka, M.; Jinnai, H.; Hashimoto, T.; Qiu, Y.; Han, C. C. Phase separation in deuterated polycarbonate/poly-(methylmethacrylate) blend near glass transition temperature. *J. Chem. Phys.* **1993**, *99*, 2095−2100.

(42) Hammouda, B.; Briber, R. M.; Bauer, B. J. Small angle neutron scattering from deuterated polystyrene/poly(vinylmethyl ether)/protonated polystyrene ternary poly- mer blends. *Polymer* **1992**, *33*, 1785−1787.

(43) Schwahn, D.; Janssen, S.; Springer, T. Early state of spinodal decomposition studied with small angle neutron scattering in the blend deuteropolystyrene and polyvinyl- methylether: A comparison with the CahnHilliardCook theory. *J. Chem. Phys.* **1992**, *97*, 8775−8788.

(44) Takenaka, M.; Takeno, H.; Hashimoto, T.; Nagao, M. Viscoelastic effects on early stage of spinodal decomposition in dynamically asymmetric polymer blends. *J. Chem. Phys.* **2006**, *124*, 104904.

(45) Eitouni HB, B. N. *Physical Properties of Polymers Handbook*; AIP Press: New York, 2007.

A Molecular Explanation for Anomalous Diffusion in Supramolecular Polymer Networks

Jorge Ramirez,[†,‡] Thomas J. Dursch,[†] and Bradley D. Olsen*,[†]

†Department of Chemical Engineering, Massachusetts Institute of Technology, Cambridge, Massachusetts 02139, United States
‡Department of Chemical Engineering, Universidad Politécnica de Madrid, Madrid, Spain

S Supporting Information

ABSTRACT: Recent experiments have revealed that a variety of associative polymers with different architecture (linear and branched) and different nature of the associating interaction (associative protein domains and metal−ligand bonds) exhibit unexplained superdiffusive behavior. Here, Brownian dynamics simulations of unentangled coarse-grained associating star-shaped polymers are used to establish a molecular picture of chain dynamics that explains this behavior. Polymers are conceptualized as particles with effective Rouse diffusivities that interact with a mean field background through attachments by stickers at the end of massless springs that represent the arms of the polymer. The simulations reveal three mechanisms of molecular diffusion at length scales much larger than the radius of gyration: hindered diffusion, walking diffusion, and molecular hopping, all of which depend strongly on polymer concentration, arm length, and the association/dissociation rate constants. The molecular model establishes that superdiffusive scaling results primarily from molecular hopping, which only occurs when the kinetics of attachment are slower than the relaxation time of dangling strands. Scaling relationships can be used to identify the range of rate constants over which this behavior is expected. The formation of loops in the networks promotes this superdiffusive scaling by reducing the total number of arms that must detach in order for a hopping step to occur.
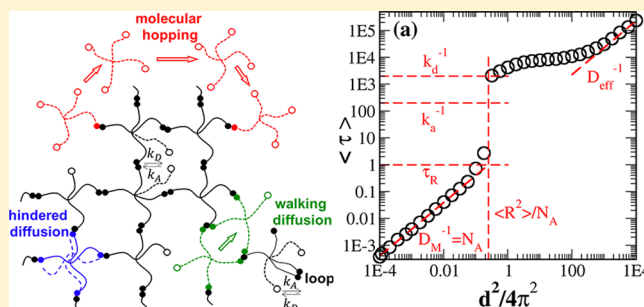
■ INTRODUCTION

Supramolecular networks are an exciting class of soft materials with significant impact in fields as diverse as enhanced oil recovery,[1] synthetic extracellular matrices for tissue engineering,[2] injectable biomaterials for minimally invasive surgery,[3,4] sacrificial components in tough and fatigue resistant physical double networks,[5] and self-healing soft materials for autonomous damage repair.[6] In contrast to their chemically cross-linked counterparts, supramolecular networks are formed by temporary physical[7−12] or chemical bonds[7,8,13] whose rates of association/dissociation govern junction dynamics and, consequently, the rheological response of the network.[10−12,14−17] As a result of the transient nature of the bonds, associative polymers can inherently dissipate part of the stress stored in the network strands, and the constituent molecules can diffuse within the networks on length scales greater than their radius of gyration.[1,10−12,14,18−24] This allows the network to dynamically rearrange and to respond to mild external stimuli. Therefore, a quantitative description of molecular motion is critical to overcoming important challenges such as predicting the rate of degradation of implantable biomaterials,[25] determining the time scale of self-healing in networks,[26] understanding how cells dynamically remodel hydrogels,[27] and calculating the rheological response of shear-thinning materials.[3]

Theoretical efforts have addressed supramolecular-network dynamics on the macroscopic and molecular levels;[14−17,20−24,28] however, knowledge of diffusive dynamics, especially self-diffusion, of the network-forming constituents remains limited.[10−12] Diffusion measurements provide a complementary probe of molecular dynamics to rheology, and comparison of dynamic theories with diffusion data provides critical insight into the testing and development of dynamic models. In addition, diffusion itself is an important dynamic property in many polymeric systems.

Recent studies[10−12,28] have shown that self-diffusive polymer dynamics often contain unexpected physics; in particular, apparent superdiffusive scaling regimes (i.e., when the distance versus time dependence is stronger than Fickian diffusion) are observed on length scales much larger than the radius of gyration of the polymers that make up the gel. Using forced Rayleigh scattering (FRS), Tang et al.[10−12] observed such superdiffusive regimes in metal coordinate star-polymer gels and associative linear coiled-coil protein gels. These non-Fickian scaling regimes are not predicted by the sticky Rouse/reptation theories,[21−24] indicating that the state-of-the-art understanding of associative polymer dynamics is incomplete.

To explain the observed superdiffusive scaling regimes, Tang, Wang, and Olsen[10−12] developed an empirical two-state model

where a diffusing species is in dynamic equilibrium between a molecular state ("fast") and an associated ("slow") state, and molecules can exchange between both states by means of first-order reactions. Despite its seeming simplicity, the model quantitatively captured the transition from superdiffusive scaling at intermediate length scales to Fickian diffusion at large scales. In this Fickian regime, the effective diffusivity is governed by the fast-state diffusivity and corresponding fraction of time spent in the fast state, whereas in the apparent superdiffusive regime, the rate of diffusion is governed by the transition rate between the fast and slow diffusing states.

While the two-state model proved quantitatively accurate in predicting the dynamics of the materials, it does not provide insight into the detailed mechanisms underlying these surprising observations. Recently, Tirrell and co-workers[28] demonstrated that diffusion of telechelic molecules (i.e., with only two associative groups and three molecular associative states) measured by fluorescence recovery after photobleaching (FRAP) can be accurately captured by a three-state model accounting for all molecular states (zero, one, and two stickers attached to the network). While the ability of Tirrell and co-workers[28] to reduce the telechelic system to three states is intuitive based on the limited number of molecular configurations, the systems studied by Tang et al.[10−12] have significantly more than two molecular configurations, making the efficacy of the two-state model surprising.

Here, it is hypothesized that the superdiffusive scaling results from molecular hopping, where a molecule detaches completely from the network and diffuses a distance much larger than its own size. The goal of this work is to systematically test this hypothesis using molecular simulations. Specifically, Brownian dynamics of unentangled coarse-grained associating star-shaped polymers (a direct analogue to the system studied experimentally in ref 10) is employed to capture the essential physics of self-diffusion in supramolecular networks. The model is validated through comparison with previously reported experiments.

■ MODEL AND METHODS

In our model, the supramolecular network is formed by n four-armed star-shaped molecules in a well-stirred solution of constant volume $\tilde{V}$. The position of each polymer is tracked by the coordinates of its junction point $\tilde{r}_i$, $i = 1...n$. Each arm is a Gaussian chain of N Kuhn steps of length b and friction coefficient ξ_0 and is decorated with an associative group or sticker at the end that can dynamically form connections with other free stickers, as illustrated in Figure 1. The one-dimensional stochastic differential equation to update the position of molecule i is

$$d\tilde{r}_i = d\tilde{t} \frac{k}{\xi} \sum_{j=1}^{N_A} (\tilde{a}_{ij} - \tilde{r}_i) l_{ij} + \sqrt{\frac{2k_B T}{\xi}} d\tilde{W}_i \tag{1}$$

where k_B is Boltzmann's constant, T is the temperature, $\tilde{W}_i$ is a standard Wiener process (Gaussian with zero mean and variance $d\tilde{t}$),[29] $N_A = 4$, $k = k_B T/Nb^2$ is the strength of the spring constant associated with each arm, $\xi = N_A N \xi_0$ is the total friction coefficient of the molecule, assumed to act at the junction point, $\tilde{a}_{ij}$ is the attachment point of sticker j of molecule i, and l_{ij} is a Boolean variable that is 0 when the sticker is free or attached to another sticker of the same molecule (forming an intramolecular association or loop) and 1 when it is attached to a sticker in a different molecule (forming an
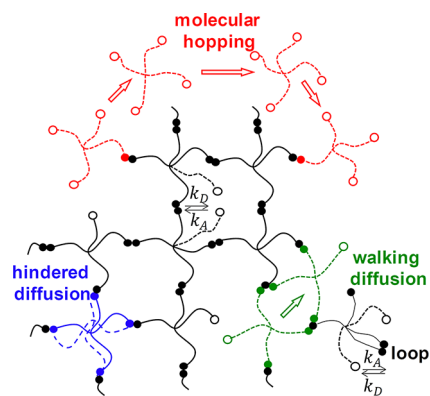

Figure 1. Schematic view of the association reactions (filled/open symbols represent associated/free stickers), the formation of loops, and the three main diffusion mechanisms in associating star-shaped polymers.

intermolecular association). As a result, the sum only runs over arms that form intermolecular bonds.

In previous experiments,[10] the polymers are in semidilute conditions and below the entanglement concentration, and star arms can be regarded as Rouse chains of correlation blobs whose size and terminal time scale with concentration according to[30,31]

$$\langle R^2 \rangle = R_g^2 \left(\frac{\phi^*}{\phi} \right)^{(2\nu-1)/(3\nu-1)} \tag{2}$$

and

$$\tau_R = \tau_F \left(\frac{\phi^*}{\phi} \right)^{(3\nu-2)/(3\nu-1)} \tag{3}$$

where ϕ is the polymer volume fraction (ϕ^* at overlap conditions), R_g^2 and τ_F are the arm size and relaxation time in dilute conditions, respectively, and $\nu = 0.588$ in a good solvent. In the experiments,[10] the anomalous diffusive scaling is observed at length and time scales that are much greater than the size (R_g) and Rouse time (τ_R) of the arms, respectively. Therefore, in the model, the internal molecular degrees of freedom are coarse-grained, and the arms are treated as Hookean dumbbells. The model represents the center-of-mass dynamics well even at shorter length and time scales, provided that star arms completely relax their conformation during the time that the associative group is detached (i.e., $1/k_A \gg \tau_R$).

The system is considered to be well stirred so all free stickers can react with each other. It is assumed that the attachment reactions are governed by second-order kinetics, whereas the detachment is first-order. Note that in the two-state model of Tang et al.[12] and in the three-state model of Rapp et al.[28] association reactions are considered to be first-order and pseudo-first-order, respectively. In our model, every time two stickers form an intermolecular association, they are linked virtually, but each sticker is effectively attached to the background at point $\tilde{a}_{ij}$, which is selected randomly from a Gaussian distribution centered at the junction point of each molecule $\tilde{r}_i$, with variance Nb^2. In this work, fluctuations of the attachment points of stickers have not been considered, and as the concentration is higher than the overlap, depletion effects in the number of intermolecular binding events have been neglected. Whenever two stickers of the same molecule create a loop, they are also linked virtually but not attached to the

background, so they do not exert any force to the molecule junction point. The kinetic constants of attachment and detachment are $\tilde{k}_A$ (units of volume/time) and $\tilde{k}_D$ (units of 1/time), respectively. The equilibrium constant of the association is $\tilde{k}_{eq} = \tilde{k}_A/\tilde{k}_D$ (units of volume).

We evolve the associative state of the stickers by means of a stochastic chemical kinetics algorithm.[32] The propensity for intermolecular bonding can be written as

$$\tilde{\alpha}^B = \frac{\tilde{k}_A}{\tilde{V}} \sum_{i=1}^{n} f_i (F - f_i) \tag{4}$$

where f_i is the total number of free arms of molecule i and F is the total number of free arms in the system. The propensity for looping reactions can be written as

$$\tilde{\alpha}^L = \frac{\tilde{k}_A}{\tilde{V}_{span}} \sum_{i=1}^{n} f_i (f_i - 1) \tag{5}$$

where $\tilde{V}_{span} = 4\pi \langle R^2 \rangle^{3/2}/3 = 4\pi N^{3/2} b^3/3$ is the volume spanned by one molecule, and the sum runs over molecules with more than one free arm. At overlap conditions, $\tilde{V} = n\tilde{V}_{span}$, which allows to express the system concentration as $\phi^*/\phi = V/nV_{span} = \tilde{V}/n\tilde{V}_{span}$. The bond dissociation reaction is the same independently of the bond being a loop or an intramolecular association. At any time, the total number of bonds in the system is equal to $(nN_A - F)/2$, so the total propensity for detachment is

$$\tilde{\alpha}^D = \frac{\tilde{k}_D}{2} (nN_A - F) \tag{6}$$

Each time step, $\Delta\tilde{t}$, the stochastic differential equation (1) is updated using an explicit Euler–Maruyama first-order algorithm,[29] and the states of the stickers are updated using the tau-leap algorithm.[32,33] In this algorithm, the numbers of bonding, looping, and detachment reactions are calculated by drawing random numbers from a Poisson distribution with mean and variance given by the product of the corresponding propensities, eqs 4–6, and the time step $\Delta\tilde{t}$.[30,32] Within each reaction channel (B, L, and D), the propensities of all possible reactions are equal, and thus the actual stickers that attach or detach are chosen randomly among all available candidates for each reaction. The simulations are run at equilibrium and the number of molecules n is large enough so that the leap condition is satisfied for the typical time steps used to update molecule positions.[33]

The arm size $\sqrt{Nb^2}$ and Rouse time $\tau_R = N\xi_0/k = N^2\xi_0 b^2/k_B T$ are chosen as the units of length and time in the system, respectively. In these units, the stochastic differential equation (1) becomes

$$dr_i = \frac{dt}{N_A} \sum_{j=1}^{N_A} (a_{ij} - r_i) l_{ij} + \sqrt{\frac{2}{N_A}} dW_i \tag{7}$$

and the kinetic constants have the following expressions:

$$k_A = \frac{\tau_R}{(Nb^2)^{3/2}} \tilde{k}_A$$

$$k_D = \tau_R \tilde{k}_D$$

$$K_{eq} = \frac{\tilde{K}_{eq}}{(Nb^2)^{3/2}} \tag{8}$$

The dimensionless volume spanned by a molecule is equal to $V_{span} = 4\pi/3$. The expressions for the nondimensional propensities are equivalent to eqs 4–6 but without the tildes. In total, the model has five parameters: k_A, K_{eq}, R_g, τ_F, and ϕ.

At every time step Δt, each sticker on the diffusing polymer may undergo one of four possible events (see Figure 1): (1) remain unreacted, (2) form a loop (intramolecular attachment), (3) form a bridge (intermolecular attachment), or (4) detach from a loop or bridge. Sticker association is considered in a mean-field sense: the probability of association of a sticker takes into account the state of all stickers in the system. For each time step, B, L, and D reactions and the molecules that react within each channel are sorted randomly to avoid bias.

In FRS measurements,[12] two coherent laser beams of wavelength λ cross at an angle θ inside a sample where a small fraction of tracer molecules have been labeled with chromophores. By constructive interference, the laser beams create a one-dimensional sine-shaped interference pattern of period $d = \lambda/2 \sin(\theta/2)$ in the sample. The chromophores are bleached in the higher intensity regions of the interference grating, effectively creating a sinusoidal concentration profile of nonbleached molecules. The diffusion of the tracers with time destroys the grating, and by tracking the decay of the scattered intensity of the sample as a function of time, it is possible to extract the characteristic relaxation time $\langle\tau\rangle$ of the system as a function of the grating period d. For a substance diffusing in the Fickian regime, the relationship between $\langle\tau\rangle$ and d^2 is linear with slope given by $1/4\pi^2 D$, where D is the molecular self-diffusion coefficient.

In order to model FRS experiments,[10−12] a large ensemble $n = 10^5$ of molecules, whose stickers' states have been previously equilibrated, are randomly distributed in a one-dimensional periodic domain of length d with normalized probability distribution $p(x) = (\sin(2\pi x/d) + 1)/d$ that represents the initial one-dimensional sinusoidal concentration profile of bleached dye-label molecules created during the writing interval of the FRS experiment, where d denotes the period of the grating[10−12] (see Figure 2b). In order to distribute the molecules randomly according to $p(x)$, we first calculate $P(x) = \int p(x) \, dx$ and use the standard transformation method described in section 7.2 of *Numerical Recipes*.[34] Then, the molecules are allowed to evolve (see Figure 2a), and periodically, a normalized histogram of molecular positions in the 1D domain is built (see Figure 2b). This histogram is Fourier transformed, and the amplitude of the longest mode at that time, $I(t)$, is calculated, which corresponds to the scattered intensity measured in the experiments. The simulations are run at equilibrium; therefore, the distribution of the states of the stickers is constant with time. As molecules diffuse over time, this intensity decays monotonically toward zero (see Figure 2c). To obtain the characteristic time, $\langle\tau\rangle$, an exponential function is fit to the resulting transient $I(t)/I(0)$ data. For intermediate values of d, the intensity shows two relaxation modes. A sum of two exponentials is used to fit $I(t)/I(0)$, and $\langle\tau\rangle$ is determined as the longest of the two relaxation times (details about the fitting procedure are provided in section 3 of the Supporting Information). Resulting characteristic times are then acquired as a function of domain size. It is important to note that although the distribution of molecules according to $p(x)$ suggests a nonhomogeneous density of molecules in the system, the whole ensemble of n molecules represents the equilibrium state of the system at any point in space. The gradient is only in the labeled tracer component. The
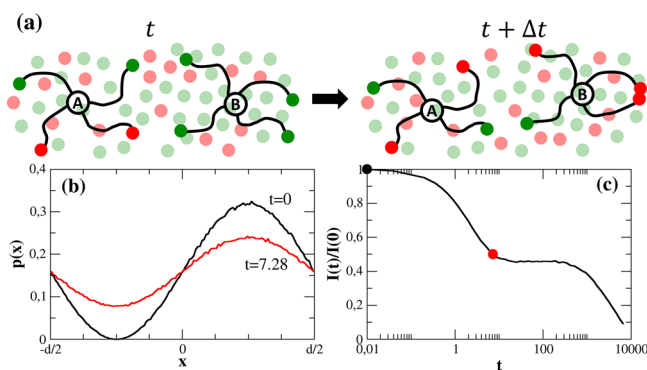
Figure 2. Schematic of the algorithm for the simulation of an FRS experiment. (b) Molecules are initially distributed in the domain $[-d/2, d/2]$ according to a sinusoidal probability distribution (panel b). (a) At time t, molecule A has two free stickers (green dots) and another two attached to the background (red dots), while molecule B has four free stickers. A and B diffuse over a mean-field background made of free and attached stickers (faded green and red dots, respectively), representing the current state all the stickers in the system. During the time step Δt, the centers of mass of A and B move according to eq 7, and the states of their stickers, as well as the states of the background stickers, change according to the stochastic reaction rules, with propensities given by eqs 4−6. (b) Due to the molecular motion, the density distribution of molecular centers of mass evolves, as seen here for a system of $N = 10^5$ star molecules with 4 arms, $k_A = 0.0025$, $K_{eq} = 5$, at overlap concentration, at times $t = 0$ and $t = 7.28$. (c) Normalized intensity decay calculated by Fourier transforming the distributions in (b), with the highlighted times $t = 0$ (black symbol) and $t = 7.28$ (red symbol).

probabilities of sticker binding are not dependent on the local density of free stickers. Any pair of molecules in the system may become virtually bonded by intermolecular association, independently of their relative positions in real space. This method to simulate the FRS experiment is fully equivalent to calculating the one-dimensional dynamic structure factor of the position of the junction points as the molecules diffuse in space.

■ RESULTS AND DISCUSSION

Figure 3a displays a typical plot of the characteristic time, $\langle \tau \rangle$, as a function of domain length squared, $d^2/4\pi^2$, from simulations of four-arm star polymers with $K_{eq} = 5$, $k_A = 0.0025$, and $\phi^*/\phi = 1$. The simulation results demonstrate that
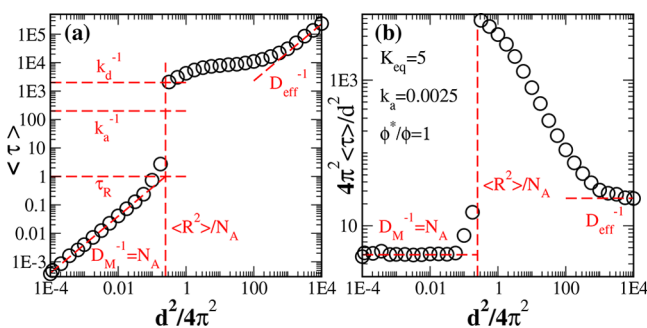
this relatively simple molecular model is able to capture both the apparent superdiffusive and large d^2 Fickian regimes observed in experimental measurements.[10−12]

The simulated FRS result contains four regimes: an early Fickian regime, a caging regime, an apparent superdiffusive regime, and a late Fickian regime. Given that $K_{eq} > 1$, at equilibrium most of the stickers are attached to the background. At times much smaller than τ_R (1 in nondimensional units), the molecules still do not feel the attachment potential and can move freely with diffusion coefficient $D = N_A^{-1}$, up to a maximum distance $\langle R^2 \rangle / N_A$ (N_A^{-1} in nondimensional units), which corresponds to the maximum mean-square displacement of the center of mass of a molecule that has N_A stickers attached to the background. In this regime, $\langle \tau \rangle$ increases linearly to τ_R with slope equal to $D^{-1} = N_A$. At τ_R, a sharp increase in $\langle \tau \rangle$ is observed due to a caging effect. Attached molecules are trapped in a cage of size $\langle R^2 \rangle / N_A$ and must wait for the arms to detach in order to diffuse over longer distances. For time scales, $\langle \tau \rangle$, larger than the inverse of the detachment rate, k_D^{-1}, stickers can detach from and reattach to the background, moving the molecular center of mass in the process. Motion of the center of mass over distances greater than $\langle R^2 \rangle / N_A$ through sequential detachment and reattachment of individual arms is termed walking. Walking is the most frequently observed diffusion event due to the relatively high likelihood of single arm detachment events. Infrequently, some molecules may also detach all their stickers and diffuse freely throughout the network in a process referred to as hopping. During this rare event, molecules diffuse with diffusion constant $D = N_A^{-1}$. It is hypothesized that in order to observe superdiffusive scaling in FRS experiments, hopping must be faster than the walking mechanism over large distances. For that to occur, the distance traveled by molecules during hopping events must be much larger than the molecular radius of gyration, which is the characteristic size of a walking step. In the crossover between the early and late Fickian regimes, the interplay between walking and hopping modes dictates the prominence and shape (i.e., amplitude and inflection) of the apparent superdiffusive regime. At large d^2, the polymers again exhibit Fickian diffusion, but now with an effective diffusivity, D_{eff}, that contains contributions from the walking and hopping mechanisms.

Differences in diffusivity between the two limiting Fickian regimes and the non-Fickian behavior at intermediate length scales are highlighted in Figure 3b, where the primary ordinate, $\langle \tau \rangle$, is renormalized by the abscissa, $d^2/4\pi$. Diffusion coefficients in the short and long length scale Fickian regimes are now given by the inverse of the plateau values. *A priori* calculation of self-diffusion coefficients in both Fickian regimes is provided in section 2 of Supporting Information.

The results from the simulations agree qualitatively with the experimental data at large d^2 values[12] (current experiments cannot resolve the early time Fickian diffusion and caging regimes). In the simulations, the escape from the cage occurs at $d^2 \approx 4\pi^2 \langle R^2 \rangle$, which is 1−2 orders of magnitude larger than the molecular size. The exact location of the large d^2 Fickian regime depends on the values of k_A and K_{eq}. In the particular example shown in Figure 3, this regime is observed at d^2 values that are 4−5 orders of magnitude larger than the molecular size, in reasonable qualitative agreement with the experiments.

A comparison of FRS simulations and mean-square displacement measurements shows that this unexpected regime is not observed in the mean-square displacement. In Figure 4a, the mean-square displacement of the center of mass of molecules
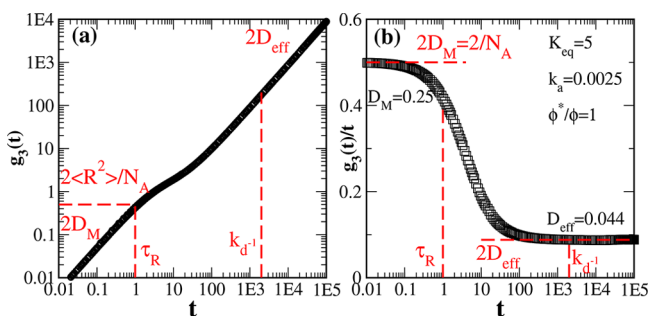

Figure 3. (a) Characteristic time $\langle \tau \rangle$ as a function of the domain length from BD simulations of FRS experiments of molecules with 4 arms, $k_A = 0.0025$ and $K_{eq} = 5$, at the overlap concentration. (b) Normalized $\langle \tau \rangle$ as a function of the domain length, revealing differences in the early- and large-distance diffusion coefficients as well as the apparent superdiffusive scaling.

Figure 4. (a) Mean-square displacement of the center of mass, $g_3(t)$, as a function of time from BD simulations of molecules with 4 arms, $k_A = 0.0025$ and $K_{eq} = 5$, at the overlap concentration. (b) $g_3(t)$ divided by time, highlighting the early and late Fickian behavior, as well as the subdiffusive regime in the crossover.

with 4 arms, $k_A = 0.0025$ and $K_{eq} = 5$, and at the overlap concentration (same case as Figure 3) is shown. Early and late Fickian diffusion regimes are clearly observed, with self-diffusion coefficients that agree well with those extracted from Figure 3. However, no superdiffusive scaling is observed in the crossover regime. Instead, a clear subdiffusive regime is found, as shown in Figure 4b, where the mean-square displacement is divided by time. Comparison between Figures 2 and 3 shows that the caging regime observed in the FRS simulation corresponds in time scale to the subdiffusive regime observed in the mean-square displacement; both the apparent superdiffusive and late Fickian regimes in the FRS simulation occur within the late Fickian regime of the mean-square displacement plot. Therefore, FRS results are more sensitive to the molecular association mechanisms than mean-square displacement, and the $\langle \tau \rangle$ vs d^2 plot shows richer features than the $\langle r^2 \rangle$ vs t plot, even though both methods are sampling different moments of the same distribution of displacements of the same physical model.

To illustrate the origin of these differences, the probability distribution of the center-of-mass displacement as a function of time for molecules with 4 arms, $k_A = 0.0025$ and $K_{eq} = 5$, and at the overlap concentration (same case as Figures 3 and 4) is shown in Figure 5a. When $t \leq \tau_R$, the molecules are trapped in the cage and the distribution is Gaussian, as proved by the small values of the one-dimensional non-Gaussian parameter[35] $\alpha = \langle r^4 \rangle / 3\langle r^2 \rangle^2 - 1$ shown in Figure 5b. At times $t \geq 10\tau_R$, the distribution becomes bimodal, with a Gaussian mode of small variance that represents the molecules that have not been able to detach completely from the background, and therefore have
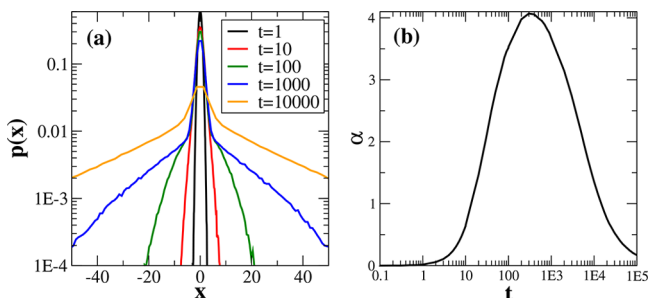
very small diffusivity, and a second mode that represents the displacement of molecules that have escaped the cage by means of the walking and hopping mechanisms. In this time region, the parameter $\alpha > 1$ indicating a non-Gaussian distribution, and superdiffusive scaling is observed in the FRS experiments. At times $t \gg k_D^{-1}$, the parameter α decreases slowly to zero, and the second Fickian regime is observed. The FRS simulations show an apparent superdiffusive regime while the mean-square displacement does not because the FRS simulations sample a different moment of the distribution of molecular motion (the one-dimensional dynamic structure factor of an isotropic system is equivalent to the average $\langle \cos(qr) \rangle$ that is more sensitive to the distribution of diffusivities while the mean-square displacement ($\langle r^2 \rangle$) is sensitive just to the average. Both ways of looking at the same molecular motion are qualitatively very similar up to the point when the molecules escape from the caging regime (in fact, up to that regime, one plot is approximately the reflection of the other by the diagonal line $y = x$). At longer times, the mean-square displacement of the system can be much larger than the size of the cage if a small fraction of molecules detaches from the network and diffuses over very long distances. However, in FRS measurements, when the period of the grating is larger than the molecular size, a large fraction of molecules must diffuse over distances of the order of d^2 in order to destroy the sinusoidal distribution of unbleached chromophores. For that to happen, the system needs to wait a very long time. Therefore, FRS is more sensitive to the large displacement tail of the distribution, providing a very important probe into molecular dynamics that complements other methods of measuring diffusion.

In understanding this effect, it is very illustrative to compare to the family of models originally proposed by Tang, Wang, and Olsen and Tirrell and co-workers. These models are continuum models of reaction−diffusion which are represented by one differential equation for each diffusing species, and the species are allowed to interconvert according to the laws of chemical kinetics. When mean-square displacement is plotted for any member of this family, only Fickian behavior is observed, where the diffusivity is an average of all the different species based on their relative abundance. While the average remains unchanged from a single effective species, the distribution of displacements changes substantially, showing a peak for the abundant, slow species and a long tail for the rare, fast diffusive events. The FRS measurement is therefore extremely useful in understanding different molecular mechanisms because it can differentiate between the single effective species and the multiple different species.

Comparing diffusion rates via different molecular mechanisms enables scaling relationships to be derived that estimate the range of molecular parameters over which the apparent superdiffusive regime can be observed. At large length and time scales, the effective diffusion coefficient D_{eff} has contributions from both walking and hopping mechanisms (Figure 1). Hopping diffusion can be calculated as the product of the diffusion constant of a free molecule, $D = 1/N_A$, times the probability that a molecule is completely detached from the network. Walking diffusion can be estimated by means of a simple scaling argument. During a walking event, a molecule that has j stickers bonded to the background detaches one with attempt frequency k_D. The mean-squared displacement of the center of mass during the walking step, before the free arm gets bonded again, is given by the size of the arms $\langle R^2 \rangle$ divided by the number of arms that remain attached to the network, i.e.,

Figure 5. (a) Probability distribution of the motion of the center of mass of molecules with 4 arms, $k_A = 0.0025$ and $K_{eq} = 5$, at the overlap concentration. (b) Time evolution of the one-dimensional non-Gaussian parameter $\alpha = \langle r^4 \rangle / 3\langle r^2 \rangle^2 - 1$ for the same system.

$\langle R^2 \rangle / (j-1)$ (equal to $1/(j-1)$ in the units of the simulation). Therefore, the diffusion coefficient of a molecule walking on j arms is $k_D/(j-1)$. A molecule can walk on $j = 2...N_A$ arms (when it has just one arm attached to the background, detachment leads to a hopping event), and each of the walking contributions must be multiplied by the probability of having j arms attached to the background. The scaling argument above assumes that walking occurs by detaching and reattaching a single arm at a time (i.e., it neglects rare but important events such as when a molecule goes from $j \to j-1 \to j-2$ arms attached). For $K_{eq} \gg 1$, it is more likely that a molecule will attach a free arm back to the background before it detaches a second one. The resulting effective diffusion coefficient of the walking and hopping mechanisms is

$$D_{eff} = D_{walk} + D_{hop} = \sum_{j=2}^{N_A} p_j k_D \frac{\langle R^2 \rangle}{j-1} + \frac{p_0}{N_A} \quad (9)$$

where p_j is the probability that a molecule has j arms attached to the background. Although eq 9 is approximate, it successfully permits quantitative prediction of diffusivities in the large length-scale regime as a function of a wide variety of parameters including K_{eq}, k_A, N_A, and concentration (see section 2 of the Supporting Information).

A general criterion for observing the apparent superdiffusion emerges by examining the curve shape as it exits the caging regime. In the case of no superdiffusive scaling, molecules should exhibit Fickian scaling immediately following the caging regime, at the point $d^2/4\pi^2 = 1/N_A$ and $\langle \tau \rangle = k_D^{-1}$. The self-diffusion coefficient of such Fickian process would be equal to k_D/N_A (see dashed blue line in Figure 6a). For the apparent
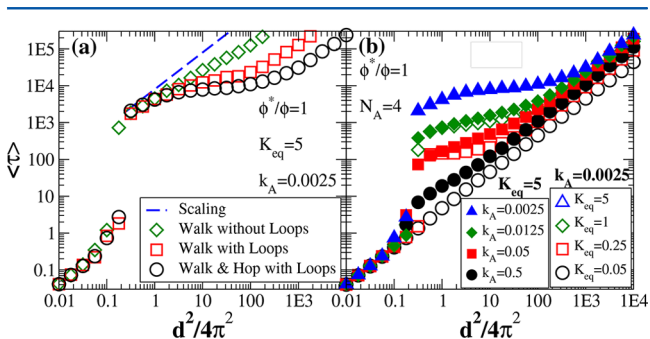

superdiffusive scaling to be observed, the effective diffusion coefficient at large distances should exceed that of the limiting Fickian scaling described above or

$$D_{eff} \gg \frac{k_D}{N_A} = \frac{k_A}{N_A K_{eq}} \quad (10)$$

which corresponds to the hypothetical diffusion coefficient of a molecule walking on $N_A + 1$ arms.

Although both walking and molecular hopping contribute to D_{eff}, the apparent superdiffusive scaling is most easily observed when molecular hopping is the primary diffusive mode, as

illustrated in Figure 6a. When hopping is switched off in the simulations, the apparent superdiffusive scaling is still observed but to a lesser extent. The ability to form loops enhances diffusion, as seen in Figure 6a, by effectively reducing the number of arms that need to be detached in order to hop and by increasing the walking diffusivity. When molecular hopping is prevalent, $D_{hop} \gg D_{walk}$ and $D_{eff} \approx D_{hop} = p_0/N_A$. In this case, the criterion for observing superdiffusive scaling in eq 10 becomes $k_A \ll p_0/K_{eq}$, where p_0 depends on the number of arms and the equilibrium constant of the attachment reactions. The calculation of the probabilities p_j can be difficult, in the full model, but they can be easily estimated if the looping reactions are turned off (see section 4 of Supporting Information). In that case, $p_0 \approx K_{eq}^{-N_A/2}$, so the requirement for observing superdiffusive scaling in the absence of looping becomes

$$k_A \ll K_{eq}^{1-N_A/2} \quad (11)$$

Although approximate, eq 11 reveals that superdiffusive scaling is less prevalent for star polymers containing many arms and for large values of the association equilibrium constant. Figure 6b, which plots the average characteristic time, $\langle \tau \rangle$, versus d^2 for four-arm star polymers at fixed concentration as a function of k_A (with constant K_{eq}) and K_{eq} (with constant k_A), respectively, clearly shows that the simulation results are consistent with this scaling prediction. The values of k_A and K_{eq} in both plots have been chosen to give identical inverse detachment times, k_D. In Figure 6b, superdiffusive scaling is observed when $k_A < 0.1$ in good agreement with eq 11, despite the presence of looping. For $k_A > 0.1$, superdiffusive scaling is less easily observed as indicated by eq 11. Walking diffusion becomes the prevalent diffusive mode, since D_{walk} increases strongly with increasing k_A, while D_{hop} is independent of k_A in eq 9. Superdiffusive scaling is observed for values of $K_{eq} > 1$ as expected because an associated network is required to produce differing diffusive mechanisms. The range of length scales over which the superdiffusive scaling is observed widens for increasing values of K_{eq}.

Loop formation increases the probability of hopping, increasing the likelihood of star polymers exhibiting super-diffusive scaling. The balance between intermolecular and intramolecular association of stickers is primarily governed by concentration. This effect is highlighted in Figure 7a, where $\langle \tau \rangle$ versus d^2 is shown for constant values of k_A and K_{eq}, at different

Figure 6. (a) $\langle \tau \rangle$ versus $d^2/4\pi^2$ for $N_A = 4$, $\phi^*/\phi = 1$, $K_{eq} = 5$, and $k_A = 0.0025$, with all diffusion mechanisms (black symbols), only walking mechanisms (red symbols), only walking mechanisms with loops forbidden (green symbols), and limiting inverse effective diffusion coefficient N_A/k_D when no superdiffusive scaling is observed (blue dashed line). (b) $\langle \tau \rangle$ versus $d^2/4\pi^2 N_A = 4$, $\phi^*/\phi = 1$, varying k_A at fixed $K_{eq} = 5$ (closed symbols), and varying K_{eq} at fixed $k_A = 0.0025$ (open symbols).
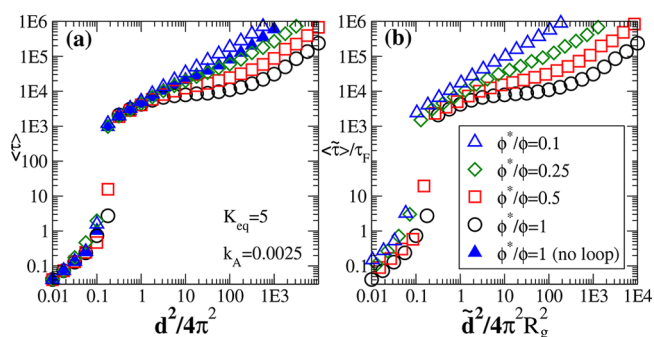
Figure 7. (a) $\langle \tau \rangle$ versus $d^2/4\pi^2$ for varying concentration, expressed as the ratio of the overlap volume fraction to the system volume fraction, ϕ^*/ϕ, with fixed $k_A = 0.0025$ and $K_{eq} = 5$, for molecules with $N_A = 4$ arms and loops allowed (open symbols). Filled symbols show a case in which loop reactions are not allowed. (b) Same results represented for real units, taking into account the scaling of the molecular size and relaxation time given by eqs 2 and 3.

polymer volume fractions. Below the overlap concentration ($\phi^*/\phi > 1$), looping is highly probable and hopping is more likely. As concentration increases above the overlap concentration ($\phi^*/\phi < 1$), hopping becomes increasingly difficult because star arms of different molecules interpenetrate and intermolecular associations are more likely. In Figure 7a, the width of the apparent superdiffusive region becomes narrower as the concentration of polymers increases, until it disappears completely for ($\phi^*/\phi < 0.1$). The diffusion behavior of a concentrated solution ($0.1 < \phi^*/\phi < 0.25$) is qualitatively similar to that of a solution at the overlap concentration for which looping reactions have been turned off.

In semidilute conditions, according to eqs 2 and 3, changes in concentration affect the molecular size and relaxation time, used as basic units of length and time in our simulations. In a good solvent, the arm size decreases with concentration, whereas the relaxation time increases. In Figure 7b, the nondimensional simulation results of Figure 7a are shown in real units, scaled by the size, R_g, and relaxation time, τ_F, of the arms in dilute conditions. Higher concentrations have a smaller cage size and slower diffusion constants. The $\langle \tilde{\tau} \rangle$ vs $\tilde{d}^2$ curves are more spread out than the same curves in nondimensional units.

In order to test the validity of the assumptions of the model, the theoretical predictions have been compared to experimental FRS measurements of four-arm poly(ethylene glycol) star polymers of $M_w = 10\,000$ g/mol, end-functionalized with terpyridine which associates with divalent Zn^{2+} ions in N,N-dimethylformamide, a good solvent for the polymer.[10] The units of length and time in the simulations are rescaled using eqs 8 and 9, respectively, and the values of the nondimensional rate and equilibrium constants are modified accordingly. Overall, the model has five fitting parameters: K_{eq}, k_A, R_g, τ_F, and ϕ. To reduce the complexity of the fitting procedure, the concentration ϕ is fixed based upon the experimental conditions, and the other four parameters are fit to the data. Figure 8a compares experimental data of Tang et al.[10] with the
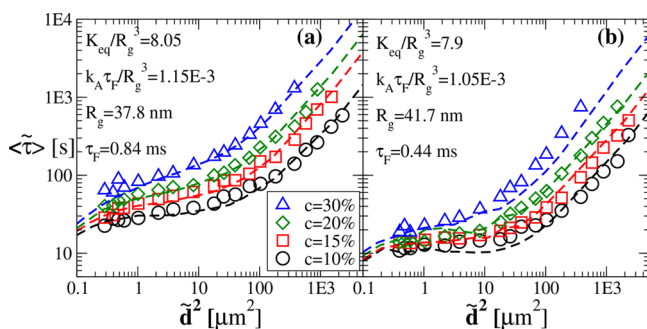

Figure 8. (a) Simultaneous fit of the theory to experimental self-diffusion data of telechelic 4-arm PEG stars at different concentrations; see Tang et al.[10] (b) Fit to experimental data of tracer diffusion of 3-arm star tracers through a 4-arm star gel matrix; see Tang et al.[10]

simulation results for the best-fit parameter set, values of which are included in the inset to the figure. Here, each theoretical point corresponds to a separate FRS simulation. In all cases, simulation results are in good qualitative agreement with experimental data over several decades of length and time, and at several polymer concentrations, using only the single set of fitting parameters.

In Figure 8b, the simulation results are fit to experimental measurements of four-arm tracer molecules with only three stickers diffusing in a mesh of four-arm molecules with four stickers. The predictions of the model have been calculated by diluting 2% of molecules with 4 arms and only three stickers in a matrix of stars with 4 stickers, following the same approach as in the experiment. The agreement of the theory with the experimental data is also good and manages to capture the faster diffusion and the sharper transition from the super-diffusive scaling to the Fickian regime at long distances. The fitting is somewhat noisier in this case because fewer molecules are used and the statistics are poorer. The values of the fitting parameters are very similar in both cases.

In contrast to the phenomenological two-state theory proposed previously,[12] the parameters extracted by fitting the simulations have a well-defined molecular interpretation given by the development of the model. In Figure 8a, however, the obtained values of $\tau_F = 0.84$ ms and $R_g = 37.8$ nm are unexpectedly large for the molecular weight of the star arms in the experiments (in ref 19 the value of R_g is estimated as 3.5 nm). Given the approximations inherent in the highly coarse-grained view of the polymers and bond kinetics and the many approximations necessary to map the parameters of the experiment to the simulation, this is reasonable qualitative agreement with the experimental result. However, it is clear that further advances can improve the accuracy of the predictions. Including junction fluctuations may also increase the effective size of the cage and reduce the value of the parameter R_g needed to fit the data, bringing it closer to the experimentally determined values. However, this effect alone cannot account for the 1 order of magnitude difference between the experimental and the fitted values of R_g. Alternately, even though the model is formulated with a single molecule in mind, it is possible that in the experiments the same molecular mechanisms described above occur for bundles of a few molecules, with corresponding larger size and relaxation time.

■ CONCLUSIONS

Four-arm star polymers were modeled as point particles that associate with a mean-field polymer network through massless associative arms, enabling simulation of self-diffusion of these molecules at length scales larger than the polymer size. The simulation results reveal the importance of multiple mechanisms of molecular motion to traverse distances larger than the molecular scale, particularly walking and hopping. The molecular model establishes that previously reported super-diffusive scaling regimes result primarily from molecular hopping which occurs when the kinetics of attachment are slower than the relaxation time of dangling strands. The role of these different molecular mechanisms is particularly clear in FRS data because of its sensitivity to the tail of the displacement distribution caused by rare but long-distance hopping events. The presence of looping defects within the networks strongly promotes hopping by allowing a molecule to effectively reduce the total number of elastically effective connections with the network. Because different measures of diffusion such as mean-square displacement and FRS measurement are sensitive to different moments of the displacement distribution, the diffusive process may simultaneously show characteristics of both superdiffusive and subdiffusive behavior depending upon how it is measured.

These findings can be generalized to more complex associating networks with polydisperse arm length, other

chain topology, chain statistics, and association kinetics. Separately quantifying the mechanisms of molecular diffusion in this work enables decoupling their impacts, which is essential to developing correlations between molecular and macroscopic transport properties, predicting material properties *de novo*, and aiding in the development of novel polymeric materials for next-generation applications.

■ ASSOCIATED CONTENT

Ⓢ Supporting Information

The Supporting Information is available free of charge on the ACS Publications website at DOI: 10.1021/acs.macromol.7b02465.

> (a) Effect of ensemble size in the simulation results; (b) validation of the model and method in simple cases; (c) detailed analysis of the intensity decay in simulations of FRS experiments; (d) review of scaling arguments in semidilute polymer solutions; (e) details of the calculation of volume fractions in experimental data; and (f) details about the methodology to fit the data (PDF)

■ AUTHOR INFORMATION

Corresponding Author

*(B.D.O.) Tel +1 617-715-4548; e-mail bdolsen@mit.edu.

ORCID Ⓘ

Bradley D. Olsen: 0000-0002-7272-7140

Notes

The authors declare no competing financial interest.

■ ACKNOWLEDGMENTS

■ REFERENCES

(1) Zhang, P.; Huang, W.; Jia, Z.; Zhou, C.; Guo, M.; Wang, Y. Conformation and adsorption behavior of associative polymer for enhanced oil recovery using single molecule force spectroscopy. *J. Polym. Res.* **2014**, *21*, 523.

(2) Lee, K. Y.; Mooney, D. J. Hydrogels for Tissue Engineering. *Chem. Rev.* **2001**, *101*, 1869−1880.

(3) Glassman, M. J.; Chan, J.; Olsen, B. D. Reinforcement of Shear Thinning Protein Hydrogels by Responsive Block Copolymer Self-Assembly. *Adv. Funct. Mater.* **2013**, *23*, 1182−1193.

(4) Lu, H. D.; Charati, M. B.; Kim, I. L.; Burdick, J. A. Injectable shear-thinning hydrogels engineered with a self-assembling Dock-and-Lock mechanism. *Biomaterials* **2012**, *33*, 2145−2153.

(5) Chen, Q.; Zhu, L.; Chen, H.; Yan, H.; Huang, L.; Yang, J.; Zheng, J. A Novel Design Strategy for Fully Physically Linked Double Network Hydrogels with Tough, Fatigue Resistant, and Self-Healing Properties. *Adv. Funct. Mater.* **2015**, *25*, 1598.

(6) An, S. Y.; Arunbabu, D.; Noh, S. M.; Song, Y. K.; Oh, J. K. Recent strategies to develop self-healable crosslinked polymeric networks. *Chem. Commun.* **2015**, *51*, 13058−13070.

(7) Seiffert, S.; Sprakel, J. Physical chemistry of supramolecular polymer networks. *Chem. Soc. Rev.* **2012**, *41*, 909−930.

(8) Appel, E. A.; del Barrio, J.; Loh, X. J.; Scherman, O. A. Supramolecular polymeric hydrogels. *Chem. Soc. Rev.* **2012**, *41*, 6195−6214.

(9) Holten-Andersen, N.; Harrington, M. J.; Birkedal, H.; Lee, B. P.; Messersmith, P. B.; Lee, K.Y. C.; Waite, J. H. pH-induced metal-ligand cross-links inspired by mussel yield self-healing polymer networks with near-covalent elastic moduli. *Proc. Natl. Acad. Sci. U. S. A.* **2011**, *108*, 2651−2655.

(10) Tang, S.; Habicht, A.; Li, S.; Seiffert, S.; Olsen, B. D. Self-Diffusion of Associating Star-Shaped Polymers. *Macromolecules* **2016**, *49*, 5599−5608.

(11) Tang, S.; Olsen, B. D. Relaxation Processes in Supramolecular Metallogels Based on Histidine−Nickel Coordination Bonds. *Macromolecules* **2016**, *49*, 9163−9175.

(12) Tang, S.; Wang, M.; Olsen, B. D. Anomalous Self-Diffusion and Sticky Rouse Dynamics in Associative Protein Hydrogels. *J. Am. Chem. Soc.* **2015**, *137*, 3946−3957.

(13) Yang, L.; Tan, X.; Wang, Z.; Zhang, X. Supramolecular Polymers: Historical Development, Preparation, Characterization, and Functions. *Chem. Rev.* **2015**, *115*, 7196−7239.

(14) Annable, T.; Buscall, R.; Ettelaie, R.; Whittlestone, D. The rheology of solutions of associating polymers: Comparison of experimental behavior with transient network theory. *J. Rheol.* **1993**, *37*, 695−726.

(15) Tanaka, F.; Edwards, S. F. Viscoelastic properties of physically crosslinked networks: Part 1. Non-linear stationary viscoelasticity. *J. Non-Newtonian Fluid Mech.* **1992**, *43*, 247−271.

(16) Tanaka, F.; Edwards, S. F. Viscoelastic properties of physically crosslinked networks: Part 2. Dynamic mechanical moduli. *J. Non-Newtonian Fluid Mech.* **1992**, *43*, 273−288.

(17) Tanaka, F.; Edwards, S. F. Viscoelastic properties of physically crosslinked networks: Part 3. Time-dependent phenomena. *J. Non-Newtonian Fluid Mech.* **1992**, *43*, 289−309.

(18) Hackelbusch, S.; Rossow, T.; van Assenbergh, P.; Seiffert, S. Chain Dynamics in Supramolecular Polymer Networks. *Macromolecules* **2013**, *46*, 6273−6286.

(19) Rossow, T.; Habicht, A.; Seiffert, S. Relaxation and dynamics in transient polymer model networks. *Macromolecules* **2014**, *47*, 6473−6482.

(20) Green, M.; Tobolsky, A. A new approach to the theory of relaxing polymeric media. *J. Chem. Phys.* **1946**, *14*, 80−92.

(21) Tripathi, A.; Tam, K. C.; McKinley, G. H. Rheology and dynamics of associative polymers in shear and extension: theory and experiments. *Macromolecules* **2006**, *39*, 1981−1999.

(22) Rubinstein, M.; Semenov, A. N. Thermoreversible gelation in solutions of associating polymers. 2. Linear dynamics. *Macromolecules* **1998**, *31*, 1386−1397.

(23) Leibler, L.; Rubinstein, M.; Colby, R. H. Dynamics of reversible networks. *Macromolecules* **1991**, *24*, 4701−4707.

(24) Cates, M. Reptation of living polymers: dynamics of entangled polymers in the presence of reversible chain-scission reactions. *Macromolecules* **1987**, *20*, 2289−2296.

(25) Shen, W.; Zhang, K.; Kornfield, J. A.; Tirrell, D. A. Tuning the erosion rate of artificial protein hydrogels through control of network topology. *Nat. Mater.* **2006**, *5*, 153−158.

(26) Cordier, P.; Tournilhac, F.; Soulie-Ziakovic, C.; Leibler, L. Self-healing and thermoreversible rubber from supramolecular assembly. *Nature* **2008**, *451*, 977−980.

(27) Chaudhuri, O.; Gu, L.; Klumpers, D.; Darnell, M.; Bencherif, S. A.; Weaver, J. C.; Huebsch, N.; Lee, H.-p.; Lippens, E.; Duda, G. N.; Mooney, D. J. Hydrogels with tunable stress relaxation regulate stem cell fate and activity. *Nat. Mater.* **2016**, *15*, 326−334.

(28) Rapp, P. B.; Omar, A. K.; Shen, J. J.; Buck, M. E.; Wang, Z.-G.; Tirrell, D. A. Analysis and Control of Chain Mobility in Protein Hydrogels. *J. Am. Chem. Soc.* **2017**, *139*, 3796−3804.

(29) Öttinger, H. C. *Stochastic Processes in Polymeric Fluids*; Springer-Verlag: Berlin, 1996.

(30) de Gennes, P.-G. *Scaling Concepts in Polymer Physics*; Cornell University Press: Ithaca, NY, 1979.

(31) Rubinstein, M.; Colby, R. H. *Polymer Physics*; Oxford University Press: New York, 2003.

(32) Gillespie, D. T. Stochastic Simulation of Chemical Kinetics. *Annu. Rev. Phys. Chem.* **2007**, *58*, 35−55.

(33) Cao, Y.; Gillespie, D. T.; Petzold, L. R. Efficient step size selection for the tau-leaping simulation method. *J. Chem. Phys.* **2006**, *124*, 044109.

(34) Press, W. H.; Teukolsky, S. A.; Vetterling, W. T.; Flannery, B. P. *Numerical Recipes in C*, 2nd ed.; Cambridge University Press: New York, 1992.

(35) Kumar, S. K.; Szamel, G.; Douglas, J. F. Nature of the breakdown in the Stokes-Einstein relationship in a hard sphere fluid. *J. Chem. Phys.* **2006**, *124*, 214501.

(36) Asmussen, S.; Glynn, P. W. *Stochastic Simulation: Algorithms and Analysis*; Springer: New York, 2007.

(37) van Gunsteren, W. F.; Berendsen, H.J. C. Algorithms for Brownian dynamics. *Mol. Phys.* **1982**, *45*, 637−647.